

**Document Version**

Final published version

**Citation (APA)**

He, C. (2025). *Thermomechanical Analysis of Wheel-Rail Contact: Modeling, Validation, and Application*. [Dissertation (TU Delft), Delft University of Technology]. <https://doi.org/10.4233/uuid:cc09daec-b917-4e1c-8e2d-fb16f1363abe>

**Important note**

To cite this publication, please use the final published version (if applicable). Please check the document version above.

**Copyright**

In case the licence states "Dutch Copyright Act (Article 25fa)", this publication was made available Green Open Access via the TU Delft Institutional Repository pursuant to Dutch Copyright Act (Article 25fa, the Taverne amendment). This provision does not affect copyright ownership.

Unless copyright is transferred by contract or statute, it remains with the copyright holder.

**Sharing and reuse**

Other than for strictly personal use, it is not permitted to download, forward or distribute the text or part of it, without the consent of the author(s) and/or copyright holder(s), unless the work is under an open content license such as Creative Commons.

**Takedown policy**

Please contact us and provide details if you believe this document breaches copyrights. We will remove access to the work immediately and investigate your claim.

**THERMOMECHANICAL ANALYSIS OF WHEEL-RAIL  
CONTACT: MODELING, VALIDATION, AND  
APPLICATION**



# **THERMOMECHANICAL ANALYSIS OF WHEEL-RAIL CONTACT: MODELING, VALIDATION, AND APPLICATION**

## **Dissertation**

for the purpose of obtaining the degree of doctor  
at Delft University of Technology  
by the authority of the Rector Magnificus Prof. dr. ir. T.H.J.J. van der Hagen,  
Chair of the Board for Doctorates  
to be defended publicly on Wednesday 14 May 2025 at 10:00 o'clock

by

**Chunyan HE**

This thesis has been approved by the

promotor: Prof. dr. Z. Li  
copromotor: Dr. Z. Yang

Composition of the doctoral committee:

Prof.dr.ir. A.W. Heemink,	Chairperson
Prof. dr. Z. Li,	Delft University of Technology, promotor
Dr. Z. Yang,	Delft University of Technology, copromotor

*Independent members:*

Prof. dr. ir. R.P.B.J. Dollevoet	Delft University of Technology
Prof. dr. ir. L.J. Sluys,	Delft University of Technology
Prof. dr. W. Yan,	Monash university, Australia
Prof. dr. R. Lewis,	The University of Sheffield, UK
Dr. ir. A. Zoeteman,	Prorail



**ProRail**

*Keywords:* Finite element model, contact temperature, thermal effect, friction, wheel-rail contact

*Printed by:* Gildeprint

*Front & Back:* Designed by Chunyan He

Copyright © 2024 by C. He

ISBN 978-94-6518-059-5

An electronic version of this dissertation is available at  
<http://repository.tudelft.nl/>.

*To my family*



# CONTENTS

<b>Summary</b>	<b>ix</b>
<b>Samenvatting</b>	<b>xiii</b>
<b>1 Introduction</b>	<b>1</b>
1.1 Background . . . . .	2
1.2 State of the art . . . . .	3
1.2.1 Thermal contact modeling . . . . .	3
1.2.2 Thermal contact measurement . . . . .	4
1.2.3 Wheel polygonal wear . . . . .	6
1.2.4 A summary of research gaps . . . . .	7
1.3 Objectives . . . . .	8
1.4 Outline of this dissertation . . . . .	8
<b>2 A finite element thermomechanical analysis of the development of wheel polygonal wear</b>	<b>19</b>
2.1 Introduction . . . . .	20
2.2 Modeling . . . . .	22
2.2.1 A finite element (FE) model . . . . .	22
2.2.2 Polygonal wheel profile . . . . .	24
2.2.3 Wear simulation . . . . .	25
2.3 Model verification . . . . .	26
2.3.1 Elastic contact with a round wheel . . . . .	26
2.3.2 Elastic contact with a polygonal wheel . . . . .	28
2.4 Results and discussions . . . . .	31
2.4.1 Simulation cases . . . . .	31
2.4.2 Contact stress and wear . . . . .	31
2.4.2.1 Results at one time step . . . . .	31
2.4.2.2 Results along the wheel profile . . . . .	33
2.4.3 Influence of the initial defect amplitude . . . . .	36
2.5 Conclusions . . . . .	36
<b>3 Infrared Temperature Measurement of Wheel-Rail Frictional Rolling Contact up to High Slip Ratios</b>	<b>45</b>
3.1 Introduction . . . . .	46
3.2 Experimental methodology . . . . .	48
3.2.1 V-Track test rig . . . . .	48
3.2.2 Temperature measurement system . . . . .	49
3.2.3 Test conditions and procedure . . . . .	50

3.3	Calibration of rail emissivity . . . . .	51
3.3.1	Experiment setup for rail emissivity calibration . . . . .	51
3.3.2	Calibration results . . . . .	52
3.4	Results and discussions . . . . .	53
3.4.1	Thermal results during braking . . . . .	54
3.4.2	A “wheel flat” observation . . . . .	57
3.5	Conclusions. . . . .	59
<b>4</b>	<b>Thermomechanical finite element wheel-rail contact modeling and exper-</b>	
	<b>imental validation</b> . . . . .	<b>65</b>
4.1	Introduction . . . . .	66
4.2	Method . . . . .	68
4.2.1	Numerical model . . . . .	68
4.2.2	Measurement . . . . .	72
4.2.3	Slip ratio calculation . . . . .	74
4.3	Results . . . . .	75
4.3.1	Measurement data processing . . . . .	75
4.3.2	Regression analysis . . . . .	77
4.3.3	Model validation . . . . .	78
	4.3.3.1 Simulation cases and results . . . . .	78
	4.3.3.2 Comparison with measurement . . . . .	80
4.4	Conclusions, discussion, and future work. . . . .	81
<b>5</b>	<b>Conclusions and future Work</b> . . . . .	<b>87</b>
5.1	Conclusions. . . . .	88
5.2	Future work. . . . .	89
	<b>Acknowledgements</b> . . . . .	<b>93</b>
	<b>Curriculum Vitae</b> . . . . .	<b>97</b>
	<b>List of Publications</b> . . . . .	<b>99</b>

# SUMMARY

The generation of frictional heat at the wheel-rail interface is a critical factor during train operations, especially during acceleration and braking. High slip ratios can lead to substantial thermal loading due to the rapid accumulation of thermal energy, resulting in significant temperature increases in the contact area. This thermal loading is known to accelerate wear, induce plastic deformation, and cause thermal fatigue in wheel and rail materials. Additionally, high contact temperatures around 720 °C may induce microstructural transformations in the material, leading to the formation of the white etching layer (WEL), which includes brittle martensite and makes the material more prone to cracking. These wheel-rail interface deteriorations increase maintenance costs and impact the operational safety of trains. Therefore, it is vital to investigate the wheel-rail friction-induced temperature and its effects on wheel/rail damage. The aim of this research is to better understand the thermomechanical behavior of the wheel-rail system. Three objectives are accomplished to reach this goal: 1) establish numerical models and experimental setups to accurately assess the thermomechanical behavior of the wheel-rail contact system; 2) reliably validate the thermomechanical contact model by accurately measuring the wheel-rail contact temperature, especially under the high slip ratio conditions; 3) improve the understanding of the generation and development of thermomechanical damage, e.g., polygonal wear and a “wheel flat”.

Objective 1 focuses on establishing thermomechanical numerical models and experimental setups. First, a 3D FE thermomechanical wheel-rail contact model was developed based on the parameters of an in-house test rig—V-Track in Chapter 2, facilitating the next-step model validation. Different material properties (elastic, elasto-plastic, and elasto-plastic-thermo, i.e. with thermal softening) and contact geometries (a round wheel and a wheel with polygonal wear) were applied to the FE model to investigate the influence of wheel/rail material on wheel-rail contact stress and wear depth. Kalker’s CONTACT program was used to verify the elastic contact solutions obtained with the proposed FE model with a round wheel. The simulation results indicate that the normal contact stress is higher than in pure mechanical solutions due to thermal softening and thermal expansion/contraction stresses, particularly in high-temperature areas after the crest of the polygonal profile. This suggests that wheel-rail impact contact stress and wear depth peaks can be significantly underestimated if thermal effects are not considered. Then, an innovative measurement system was developed in the V-Track to reproduce and capture high contact temperatures up to 1200 °C at the wheel-rail interface in Chapter 3. An infrared thermal camera was mounted on a moving wheel assembly, enabling a continuous measurement of contact temperature. Compared to the previous studies using thermal cameras, a more sensitive and precise camera was used in this study to capture the transient thermal phenomena that occur within short time frames, e.g., the cooling process. The measurement results indicate that the wheel-rail contact

temperature rose with the slip ratio until a “wheel flat” was formed. The contact temperature dropped when the “wheel flat” exited the contact area, and then increased again with the slip ratio. The contact temperature may reach up to 1000 °C with a slip ratio of 99%.

Objective 2 aims to reliably validate the thermomechanical contact model by accurately measuring the wheel-rail contact temperature, particularly under high slip ratio conditions. A thermomechanical finite element (FE) model for simulating wheel and rail interactions during braking was developed and it was experimentally validated up to about 360 °C in the TU-Delft V-Track test rig under braking with the same contact conditions in terms of contact pressure, slip ratio and coefficient of friction, as described in Chapter 4. After processing the measurement data, including the calculation of slip ratio and data synchronization, a regression analysis was conducted between the measured contact temperature and slip ratio. Comparisons were then made between the measured and simulated contact temperatures (with two different temperature-dependent mechanical and thermal material parameter sets) under three slip-ratio scenarios (5%, 10%, and 15%). The contact temperatures simulated with the developed thermomechanical FE model using the two different parameter sets demonstrated close similarity and aligned reasonably with the experimental results across the slip ratios of 5%, 10%, and 15%. The simulated temperatures exhibited a maximum relative error, ranging from 7.9% to 9.8%, being slightly lower than the experimental values. This suggests that the presented model is reliable for simulating wheel-rail contact with thermal effects and both the parameter sets can reflect the thermomechanical properties of the rail materials.

Objective 3 is to enhance the comprehension of the generation and development of thermomechanical damage, e.g., polygonal wear and a “wheel flat”. A 3D FE thermo-mechanical wheel-rail contact model was developed based on the parameters of the in-house test rig—V-Track in Chapter 2. Besides elasto-plastic-thermo material used in the FE model, elastic material and the polygonal profile were also applied in this FE model to investigate the need for improved FE contact modeling for accurate dynamic contact representation in polygonal wheel-rail impact and wear prediction studies. The results calculated with the elastic FE model involving a polygonal profile were compared with those obtained from Kalker’s CONTACT program. The deviation in the micro-slip solutions suggests that the FE contact modeling with a better representation of dynamic contact should be applied to the polygonal wheel-rail impact contact study and further prediction of polygonal wear development. Simulations using elasto-plastic-thermo wheel/rail material properties and initial polygonal wheel profiles are then conducted to investigate the influences of plasticity, the thermal effect, and initial defects on wheel-rail contact stress distributions and polygonal wear development as an application case. The results show that the contact temperature presents a periodic pattern along with the polygonal profile: the temperature is low at the locations just after the wheel profile trough, and it goes up gradually and reaches the highest amplitude before decreasing slightly near the next trough. The simulated wear depth peaks increase with the initial polygonal wear amplitude, suggesting that with the increase of wear ampli-

tudes, the development of polygonization is accelerated. In Chapter 3, a “wheel flat” was generated when the slip ratio reached around 40%, and the corresponding wheel-rail contact temperature was 624 °C. By tracing the temperature drop of the “wheel flat” area over time, a temperature-evolution curve was obtained, which can be well fitted with an exponential curve.

The conclusions of this dissertation are given in Chapter 5. This research has made three significant contributions to the understanding of the wheel-rail contact system. Firstly, it developed advanced numerical models and experimental setups to accurately assess the thermomechanical behavior, providing a solid foundation for simulating and analyzing the complex thermal and mechanical interactions at the wheel-rail interface. Secondly, this research experimentally validated the thermomechanical contact model, ensuring its predictions closely aligned with real-world conditions. Finally, the research significantly enhanced the understanding of the generation and progression of thermo-mechanical damage, such as polygonal wear and a “wheel flat”. This PhD research seeks to comprehend the thermomechanical behavior of the wheel-rail system, which is crucial for improving the safety, reliability, and cost-effectiveness of railway operations.



# SAMENVATTING

De opwekking van wrijvingswarmte aan de wiel-railinterface is een cruciale factor tijdens treinoperaties, met name tijdens versnelling en remmen. Hoge slipverhoudingen kunnen leiden tot aanzienlijke thermische belasting als gevolg van de snelle accumulatie van thermische energie, wat resulteert in significante temperatuurstijgingen in het contactgebied. Deze thermische belasting versnelt de slijtage, veroorzaakt plastische vervorming en leidt tot thermische vermoeïng in wiel- en railmaterialen. Bovendien kunnen hoge contacttemperaturen rond 720 °C microstructurele transformaties in het materiaal veroorzaken, wat leidt tot de vorming van de zogenaamde white etching layer (WEL), bestaande uit bros martensiet, waardoor het materiaal gevoeliger wordt voor scheurvorming. Deze degradaties aan de wiel-railinterface verhogen de onderhoudskosten en beïnvloeden de operationele veiligheid van treinen. Daarom is het van groot belang om de door wrijving veroorzaakte temperatuur aan de wiel-railinterface en de effecten ervan op schade aan wiel en rail te onderzoeken. Het doel van dit onderzoek is om het thermomechanische gedrag van het wiel-railsysteem beter te begrijpen. Drie doelstellingen zijn geformuleerd om dit doel te bereiken: 1) het opstellen van numerieke modellen en experimentele opstellingen om het thermomechanisch gedrag van het wiel-railcontact nauwkeurig te beoordelen; 2) het betrouwbaar valideren van het thermomechanische contactmodel door nauwkeurige metingen van de wiel-railcontacttemperatuur, met name onder omstandigheden met hoge slipverhoudingen; 3) het verbeteren van het inzicht in het ontstaan en de ontwikkeling van thermomechanische schade, zoals polygonale slijtage en een “wheel flat” (een lokale vlakke plek op het wieloppervlak).

Doelstelling 1 richt zich op het opstellen van thermomechanische numerieke modellen en experimentele opstellingen. Eerst werd een driedimensionaal thermomechanisch eindige-elementen (FE) wiel-railcontactmodel ontwikkeld op basis van de parameters van een interne testopstelling (V-Track), zoals beschreven in hoofdstuk 2, ter ondersteuning van de modelvalidatie. Verschillende materiaaleigenschappen (elastisch, elasto-plastisch en elastoplastisch-thermisch, d.w.z. met thermische verzachting) en contactgeometrieën (een rond wiel en een wiel met polygonale slijtage) werden toegepast in het FE-model om de invloed van het wiel-/railmateriaal op contactspanningen en slijptediepte te onderzoeken. Het CONTACT-programma van Kalker werd gebruikt om de elastische contactoplossingen van het voorgestelde FE-model met een rond wiel te verifiëren. De simulatieresultaten tonen aan dat de normale contactspanningen hoger zijn dan bij zuiver mechanische oplossingen, als gevolg van thermische verzachting en uitzettings-/krimpspanningen, met name in hogetemperatuurzones na de top van het polygonale profiel. Dit suggereert dat pieken in impactcontactspanningen en slijtage aanzienlijk kunnen worden onderschat als thermische effecten niet worden meegenomen. Vervolgens werd een innovatief meetsysteem ontwikkeld op de V-Track om hoge

contacttemperaturen tot 1200 °C aan de wiel-railinterface te reproduceren en vast te leggen (hoofdstuk 3). Een infrarood thermische camera werd gemonteerd op een bewegende wielassemblage, waardoor continue meting van de contacttemperatuur mogelijk werd. In vergelijking met eerdere studies werd een gevoeliger en nauwkeurigere camera gebruikt om transiënte thermische verschijnselen waar te nemen, zoals het afkoelproces. De meetresultaten geven aan dat de contacttemperatuur toenam met de slipverhouding totdat een “wheel flat” werd gevormd. De temperatuur daalde toen deze “wheel flat” het contactgebied verliet, en steeg vervolgens opnieuw met de slipverhouding. De contacttemperatuur kan oplopen tot 1000 °C bij een slipverhouding van 99%.

Doelstelling 2 is het betrouwbaar valideren van het thermomechanische contactmodel door nauwkeurige meting van de wiel-railcontacttemperatuur, met name onder hoge slipverhoudingsomstandigheden. Een thermomechanisch FE-model voor het simuleren van wiel-railinteracties tijdens remmen werd ontwikkeld en experimenteel gevalideerd tot circa 360 °C in de TU Delft V-Track testopstelling onder dezelfde contactomstandigheden qua druk, slipverhouding en wrijvingscoëfficiënt (zoals beschreven in hoofdstuk 4). Na verwerking van de meetgegevens, inclusief de berekening van de slipverhouding en datasynchronisatie, werd een regressieanalyse uitgevoerd tussen de gemeten contacttemperatuur en slipverhouding. Vervolgens werden vergelijkingen gemaakt tussen de gemeten en gesimuleerde contacttemperaturen (met twee verschillende temperatuurafhankelijke mechanische en thermische materiaalparametersets) onder drie slipverhoudingsscenario's (5%, 10% en 15%). De met het ontwikkelde thermomechanische FE-model gesimuleerde contacttemperaturen, met gebruik van beide parametersets, vertoonden een hoge mate van overeenkomst met de experimentele resultaten bij alle drie de slipverhoudingen. De gesimuleerde temperaturen vertoonden een maximale relatieve fout tussen 7,9% en 9,8%, en lagen iets onder de experimentele waarden. Dit wijst erop dat het voorgestelde model betrouwbaar is voor het simuleren van wiel-railcontact onder thermische invloeden en dat beide parametersets de thermomechanische eigenschappen van de railmaterialen goed kunnen weergeven.

Doelstelling 3 is het verbeteren van het begrip van het ontstaan en de ontwikkeling van thermomechanische schade, zoals polygonale slijtage en een “wheel flat”. Een 3D thermomechanisch FE-model van het wiel-railcontact werd ontwikkeld op basis van de parameters van de interne testopstelling V-Track (hoofdstuk 2). Naast het gebruik van elastoplastisch-thermisch materiaal in het FE-model, werden ook elastisch materiaal en een polygonaal profiel toegepast om de noodzaak te onderzoeken van verbeterde FE-contactmodellering voor nauwkeurige dynamische contactweergave in studies naar polygonale wiel-railimpact en slijtagevoorspelling. De resultaten van het elastische FE-model met een polygonaal profiel werden vergeleken met die van Kalker's CONTACT-programma. De afwijkingen in de micro-slipoplossingen suggereren dat verbeterde dynamische contactmodellering noodzakelijk is voor het nauwkeurig analyseren van polygonale impactcontacten en het voorspellen van de ontwikkeling van polygonale slijtage. Vervolgens werden simulaties uitgevoerd met elastoplastisch-thermische materiaalparameters en initiële polygonale wielprofielen om de invloed van plasticiteit, thermische effecten en initiële defecten op de spanningsverdeling en polygonale slijtageontwikke-

ling te onderzoeken. De resultaten tonen aan dat de contacttemperatuur een periodiek patroon vertoont in overeenstemming met het polygonale profiel: de temperatuur is laag direct na het dal in het wielprofiel, neemt vervolgens geleidelijk toe en bereikt een piek, waarna deze weer iets daalt richting het volgende dal. De gesimuleerde slijtagepieken nemen toe met de amplitude van de initiële polygonale slijtage, wat suggereert dat bij grotere amplitudes de ontwikkeling van polygonalisatie wordt versneld. In Hoofdstuk 3 werd een “wheel flat” gegenereerd toen de slipratio ongeveer 40% bereikte, en de overeenkomstige wiel-railcontacttemperatuur bedroeg 624 °C. Door het temperatuurverloop van het “wheel flat”-gebied in de tijd te volgen, werd een evolutiecurve van de temperatuur verkregen, die goed benaderd kon worden met een exponentiële functie.

De conclusies van dit proefschrift worden besproken in hoofdstuk 5. Dit onderzoek heeft drie belangrijke bijdragen geleverd aan het begrip van het wiel-railcontact. Ten eerste zijn geavanceerde numerieke modellen en experimentele opstellingen ontwikkeld om het thermomechanische gedrag nauwkeurig te kunnen beoordelen, wat een solide basis vormt voor de simulatie en analyse van complexe thermische en mechanische interacties aan de wiel-railinterface. Ten tweede is het thermomechanische contactmodel experimenteel gevalideerd, waarbij de voorspellingen goed overeenkwamen met realistische omstandigheden. Ten slotte is het inzicht in het ontstaan en de voortgang van thermomechanische schade, zoals polygonale slijtage en “wheel flat”, aanzienlijk verdiept. Dit promotieonderzoek draagt bij aan het verbeteren van de veiligheid, betrouwbaarheid en kostenefficiëntie van spoorwegoperaties.



# 1

## INTRODUCTION

## 1.1. BACKGROUND

**F**RICTION between the wheel and rail plays an important role in the train traction, braking, and curve negotiation. However, due to the rapid accumulation of thermal energy and consequent increase in temperature in the contact area, the frictional heat generated at the wheel-rail interface and the resulting thermal stresses are undesirable, particularly at high slip ratios, which occur when braking is severe or adhesion is low [1, 2]. Thermal loading is detrimental to the wheel and rail materials because it greatly expedites wear, causes plastic deformation, and causes fatigue [3–7]. Some typical thermomechanical damage examples are shown in Figure 1.1: rail burn (Figure 1.1(a)), wheel flat (Figure 1.1(b)), wheel polygonal wear under braking (Figure 1.1(c)), and thermal cracks in the wheel tread and rail top surface (Figures 1.1(d) and (e)). When subjected to high contact temperatures (e.g., 200 ~ 250 °C [8] and 350 °C [9]) with high slip ratios, wheel and rail material can be more easily worn due to thermal softening. Rail burns and wheel flats and polygonisation, accompanied by significant plastic deformation, are caused by wheel-rail sliding under high temperatures [10, 11]. Moreover, thermal loading may accelerate wheel and rail fatigue by altering material properties, e.g., decreasing the elastic and shakedown limits and making the steel susceptible to progressive plastic deformation and cracks [12]. Additionally, high contact temperatures (e.g., around 720 °C [13, 14] or 800 ~ 1000 °C [11]) may induce microstructural transformations. These changes include the transformation of pearlite and ferrite into austenite, followed by a partial conversion into martensite beneath wheel and rail surfaces, leading to the thermally-induced white etching layer (WEL) [15]. The brittle martensite in the WEL then makes the material more prone to cracking [15–18]. The thermal damage at the wheel-rail interface dramatically increases maintenance costs and impacts the safety of train operations. To better understand and prevent thermal damage, it is crucial to accurately assess the thermal effects on the wheel-rail interface.

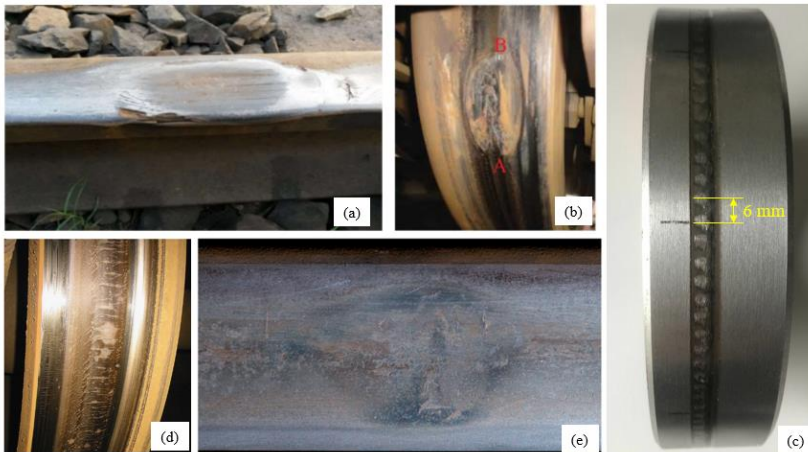


Figure 1.1: Typical wheel and rail damage caused by thermomechanical loading. (a) Rail burn [19]; (b) a wheel flat [20]; (c) polygonal wear; (d) thermal cracks on the wheel tread [21]; (e) thermal cracks in a squat [14].

## 1.2. STATE OF THE ART

### 1.2.1. THERMAL CONTACT MODELING

Considering that accurate wheel-rail contact temperature measurement is complex, labor-intensive, and expensive, especially in operational conditions [1], both analytical and numerical modeling methods have been developed to examine the thermal loading and temperature field at the wheel-rail interface. Most analytical approaches have been formulated to calculate the maximum flash temperature induced by a moving heat flux in a single body. Jaeger [22] investigated the problem of idealized plane heat sources of various shapes, such as two-dimensional (2D) uniformly distributed band sources and three-dimensional (3D) rectangular sources, moving at constant or non-constant velocities on the surface of a semi-infinite medium. The follow-up analytical analyzes then extended Jaeger's approach in two aspects: 1) by applying different moving heat sources [23, 24], and 2) by including thermal radiation and convection to the ambient [8, 25]. A 2D elliptical band source was modeled in [23] to represent the heat induced by contact. Instead of applying a predefined heat source as in [22, 23], Knothe et al. [26] calculated the 2D heat source at the wheel-rail interface based on Hertzian contact pressure, and analytically derived the temperature field engendered by wheel-rail sliding interactions through the application of Laplace transforms and Green's function. The study revealed that the wheel-rail contact temperatures do not exceed 450 ~ 500 °C if the slip ratio is less than 2% and the coefficient of friction is less than 0.6. With the consideration of heat interaction with ambient (i.e. radiation and convection), Lewis et al. [8] calculated the temperature field induced by twin-disc rolling contact from partial to full slip (slip ratio from 0.5% to 5%) and determined that the maximum contact temperature above ambient reached 113 °C under a normal contact stress of 1500 MPa and with a disc surface velocity of 0.98 m/s. To investigate the effects of contact body geometries on contact temperature, thinner and smaller twin discs operating under the same conditions as [22] were simulated in [25], which reported higher simulated contact temperatures (199.2 °C for the thinner discs and 235.3 °C for the smaller discs) than the results obtained in [8]. In addition, 3D analytical models were applied to the interaction of the wheel flange and gauge face of the rail head [27]. These analytical studies [8, 22, 23, 26] indicated that the instantaneous temperatures generated at the contact interface are related to the coefficient of friction, contact pressure, thermal properties, sliding velocity, and contact body geometry.

In contrast to analytical models, finite element (FE) models offer the capability to address transient thermal contact issues while considering complex geometries, material complexity including plasticity and temperature dependence [1, 9, 28–33], and dynamic wheel-rail interactions. Asih [9] developed a two-dimensional (2D) FE model that applied an analytical moving heat flux on the rail to investigate the thermal effect on the wear rate of the rail. It was concluded that the transition from mild to severe wear could happen when the temperature is above 350 °C. Wu et al. [30] built a 2D FE rail model and applied an instantaneous heat source to analyze the thermal effect on the rail. They concluded that the thermal effect influences the residual stress, deformation, and plastic strain of the rail. Vo et al. [31] developed a 3D FE model for a rail subjected to multiple thermal loads from passing locomotives, employing Goldak's heat source model [34]. The simulation with a slip ratio of 8.5% indicated that the rail-surface temperature may

reach 522 °C after one wheel pass and 723 °C after six. It was also concluded that the peak temperature calculated with the 2D model can be overestimated because the thermal energy emission in the transverse direction was overlooked. However, the heat source of the model was calculated based on Hertzian contact pressure. Such a simplification potentially leads to deviations of the thermal results from actual values. Naeimi et al. [28] proposed a 3D dynamic thermomechanical FE wheel-rail contact model in which the heat source was calculated based on the tangential load and micro-slip between the elements in contact. Considering the temperature-dependent nonlinear material properties, the temperature and stress field in the contact patch with a single wheel passage were obtained. The study concluded that the thermal softening of material induces higher von-Mises stresses and larger plastic deformation. The simulated peak contact temperatures with slip ratios of 10%, 18%, and 26% were 284 °C, 498 °C, and 756 °C, respectively. Lian et al. [1] then presented a 3D FE wheel-rail contact model to consider the superimposed thermal-mechanical loads induced by multiple wheel passages. The study indicated that the maximum temperature of the rail surface after 9 wheel passages may reach up to 776 °C with a slip ratio of 9.43%.

As to the model validation, attempts have been made in [35] to validate the analytical model presented in [8] for low slip ratio (below 5%) wheel-rail contact scenarios using infrared cameras. The results indicated that the measured contact temperature was between 100 and 150 °C with a slip ratio of 5%, which aligned well with the simulated results in [8]. However, although the FE models of thermal contact between wheel and braking block [36–38] or braking pad [39] have been experimentally validated using infrared cameras, no validation, to the best of the author's knowledge, has been reported for the FE wheel-rail thermal contact models with higher slip ratios (above 5%) that may induce significant thermal damage.

### 1.2.2. THERMAL CONTACT MEASUREMENT

Both contact and non-contact methods have been developed to measure temperatures at the contact interfaces, as examples shown in Figure 1.2. The contact methods commonly utilize thermocouples [5, 40–52] (e.g., Figure 1.2(a) ~ (c)), while the non-contact methods generally employ infrared thermal cameras [41, 53–56] (e.g., Figure 1.2(d)). Different test setups using thermocouples have been designed to measure contact temperatures. For instance, the thermocouples can be embedded into pre-drilled holes in a pin-on-disc setup [43], as shown in Figure 1.2(a), to identify temperature fields and heat fluxes at the contact surface [44]. It should be noted that the thermocouple was located 1mm below the contact surface in this setup and thus captured temperatures lower than those on the surface. Additionally, drilling holes into contact objects may alter their contact stiffness and stress distributions, leading to unrealistic contact conditions, as shown in Figure 1.2(b). Instead of being embedded, thermocouples can also be attached to the side faces of contact bodies close to the contact patch [45]. Such an implementation is, however, not suitable for real-life applications with complex contact geometries. In addition to the thermocouples placed near the contact patch, the thin-film thermocouples have been placed directly on the contact surfaces to measure the contact temperature, as shown in Figure 1.2(c). The thin-film thermocouples were designed based on a pin-on-flat wear test rig to measure the surface temperature distribution under a normal

load of 100N and a temperature below 150°C [46]. The thin-film thermocouples need to be firmly attached to the contact surfaces for accurate measurements [47, 57]. However, wheel-rail contact introduces high contact pressure and shear stress, potentially leading to wear, damage, or detachment of thin-film thermocouples and thus affecting measurement results. Besides, it should be noted that the discrete distribution of thermocouples provides temperature information only at specific points; therefore, the thermocouples cannot be handily used to capture continuous temperature distributions, especially in contact areas with large temperature gradients.

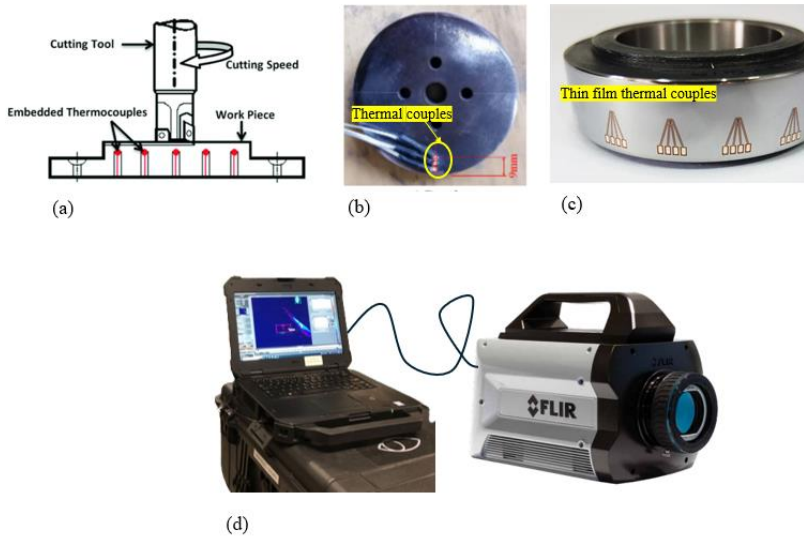


Figure 1.2: Contact temperature measurement methods. (a) Embedded thermocouples [44]; (b) attached thermocouples [45]; (c) thin-film thermocouples [48]; (d) infrared thermal camera [58].

As to the non-contact methods, infrared thermal cameras have been employed to monitor the temperature field close to the wheel-rail interface. In [59], an infrared thermal camera was mounted on a vehicle body behind a trailing wheel to measure wheel-rail contact positions as the train navigated switches and crossings. The technique in [59] was improved in [60] by mounting a thermal camera on the bogie to avoid correcting the viewing angle caused by the yaw angle difference between the vehicle body and the bogie. Digital image processing technology was then applied to process the camera-recorded thermal images to identify the positions of wheel-rail contact points. In [61], a thermal camera was mounted on the trams to monitor wheel and rail contact conditions by analyzing the thermal images. It is worth noting that the studies in [59–61] focused mainly on identifying wheel-rail contact points based on thermal images, with little attention paid to the absolute levels of contact temperature. In [8, 35], a thermal camera with a range from  $-20\text{ }^{\circ}\text{C}$  to  $350\text{ }^{\circ}\text{C}$  was used in a twin-disc test rig in the lab to

measure contact temperatures with slip ratios from 0.2% to 5%. Although the twin-disc experiments allowed precise control of contact conditions, such as the slip ratio, they had limitations in simulating the real-life wheel-rail dynamic contact [35]. In contrast, the V-Track test rig incorporates the modal characteristics of track and vehicle systems, demonstrates good dynamic similarity to actual vehicle-track systems [62] and can thus simulate real-life wheel-rail interactions. Besides, the maximum contact temperature measured in [35] is below 200 °C. Therefore, investigations of wheel-rail dynamic contact with higher contact temperatures (e.g., higher than 498 °C [28]) are still needed to provide insights into the development of thermal damage.

### 1.2.3. WHEEL POLYGONAL WEAR

Polygonal wear is typical damage that can be affected by thermal loading and occurs on the wheels of locomotives, metros, and high-speed trains [63–67]. High-amplitude vibrations induced by the impacts between rails and polygonal wheels accelerate train and track degradation and radiate high-level noises [68]. Severe polygonal wear threatens the safety of railway operations and adversely affects the ride comfort of passengers [24]. To mitigate the effects of polygonal wear, a better understanding of its initiation and development mechanisms is needed.

The initiation and progression of polygonal wear on railway wheels can be influenced by three principal mechanisms, as identified in the previous research. Firstly, initial defects play a crucial role, arising from factors such as the wheel re-profiling process [69, 70], uneven material properties [71], and static and dynamic imbalances [72]. Secondly, the natural vibrations within the train-track system may contribute to polygonal wear formation, driven by resonance frequencies from the vehicle components (e.g., wheelsets [73, 74], bogie frames [65], and linear induction motors [75]), track components (e.g., rail bending vibration modes [76]), and train-track interactions including stick-slip oscillations [77], P2 resonance [78], and frictional self-excited vibrations [79]. Lastly, the thermal effect between the wheel tread and braking blocks [37, 38] may further influence the development of polygonal wear.

Studies on the formation and growth of wheel polygonal wear have been conducted with numerical modeling. A general approach is to simulate wheel-rail contact and consequent wear by coupling a multibody dynamics (MBD) model with a wear prediction model considering initial defects [71]. The initial wheel defects and wheel/rail structural dynamics, as possible mechanisms of wheel polygonal wear generation and development, can be considered in the MBD models. The initial polygonal wear profile of the wheel could be simplified as one or several mixed harmonic waves. The wavenumber along the wheel circumference is regarded as the ‘order’ of the polygonal wear. The core connections between a MBD model and a wear model are wheel-rail contact solutions, i.e. the normal and tangential contact stresses and micro-slip distributions. Morys [80] built up a three-dimensional (3D) MBD model of an ICE-1 carriage. Hertzian theory and FASTSIM [81] were used to calculate the normal and tangential contact solutions, respectively. The study presented the simulation results of the evolution of the worn profile, which was assumed to be proportional to the wear energy, and concluded that the low-order polygonal wear could be developed into higher-order harmonics. Meyerwerk [82] built up an MBD model with a wheelset, in which the wheel axle and rims

were treated as flexible beams, and the bogie was simplified as a rigid frame. Kalker's linear theory [83] and Hertzian theory were employed to as the contact solutions. The study concluded that the phase shift of the left and right wheel profiles may influence the growth of polygonal wear, and the first and second bending modes of the wheelset are dominant contributors to polygonal wear growth. Andersson and Johanssons [78, 84] developed a model incorporating multi-rigid body wheelsets and a bogie frame, as well as FE rails. Hertzian theory and Shen-Hedrick-Elkins model [85] were employed as contact solutions. They concluded that the P2 resonance could cause the 5th, 6th, and 7th-order polygonal wear, and the track modes are the main causes of the 14th to 20th-order polygonal wear. Cai [76] developed a vehicle/track coupled dynamic model of a high speed train with an FE track model. Hertzian contact theory and FASTSIM were applied to obtain the contact solution. It was concluded that the 20th polygonal wear was related to the third-order rail vertical bending resonance occurring between the wheels of a bogie.

To deal with non-elliptical wheel-rail contact that occurs in the real-life operations [86], some MBD models applied non-Hertzian contact theories, e.g., ANALYN [87], modified Kik-Piotrowski [88] and FaStrip [89]. However, because wheel/rail material nonlinearities cannot be treated properly with the aforementioned contact methods, hardly can the MBD models accurately simulate polygonization-induced impact contact, where plasticity occurs, and be used to predict the further development of the wear. To cope with the material nonlinearities, complex wheel-rail contact geometry, and dynamic effects involved in the wheel-rail interactions, explicit FE contact models [90–93] have been broadly adopted to calculate wheel-rail dynamic contact, such as the polygonal wear-induced and flat-induced wheel dynamic responses [94, 95]. However, few of them, if any, have been combined with wear models to analyze the initiation and further development of polygonal wear.

#### 1.2.4. A SUMMARY OF RESEARCH GAPS

Despite substantial research on thermal contact modeling and experiments, several important aspects remain underexplored. Based on the aforementioned literature review and discussions, the following research gaps have been identified:

- 1) While attempts have been made to validate thermal contact models, there is a lack of validation for FE thermomechanical wheel-rail contact models, especially under high slip ratios (>5%), where thermal damage is more likely to occur.
- 2) Experimental investigation into dynamic wheel-rail contact under high contact temperatures (e.g., >498 °C) has not been addressed, due to the limitations of twin-disc setups in replicating real-world dynamics and high contact temperature conditions.
- 3) An integration of thermomechanical contact models with wear calculation is missing, restricting the understanding of the thermal damage initiation and evolution (e.g., wheel polygonal wear).

### 1.3. OBJECTIVES

This PhD research aims to understand the thermomechanical behavior of the wheel-rail system which is vital for enhancing the safety, reliability, and economic efficiency of railway operations. The following objectives are expected to be achieved:

- Objective 1:** Establish numerical models and experimental setups to accurately assess the thermomechanical behavior of the wheel-rail contact system.
- Objective 2:** Reliably validate the thermomechanical contact model by accurately measuring the wheel-rail contact temperature, especially under high slip ratio conditions.
- Objective 3:** Improve the understanding of the generation and development of thermal damage, e.g., polygonal wear and a “wheel flat”.

### 1.4. OUTLINE OF THIS DISSERTATION

To address the aforementioned three objectives, three main chapters are worked out, and their relationship with the research objectives is illustrated in Figure 1.3. In Chapter 2, a 3D thermomechanical FE wheel-rail contact model was built, which adopted the parameters of the V-Track test rig [29, 30] to facilitate the next-step model validation (in Chapter 4). The simulated elastic contact solutions were verified against the program CONTACT [96]. Other material properties (elasto-plastic and elasto-plastic with thermal softening) and different contact geometries (round wheel and wheel with polygonal wear) were applied to the FE model to investigate the influences of plasticity, the thermal effect, and initial defects on wheel-rail contact stress distributions and polygonal wear development, which addresses the objectives 1 and 3.

In Chapter 3, an innovative measurement system was developed in the V-Track to reproduce and capture high contact temperatures up to 1200 °C at the wheel-rail interface. A high-precision infrared thermal camera was mounted on a moving wheel assembly of the V-Track, enabling a continuous measurement of contact temperature. The camera used in this study can capture the transient thermal phenomena that occur within short time frames, e.g., the cooling process. A braking process was simulated in the V-Track with slip ratios ranging from about 2% to 99%. A “wheel flat”, as typical thermal damage, was generated during the braking process, and the resulting temperature field was measured over time. An emissivity calibration of the V-Track rail samples was conducted to ensure the accuracy of the temperature measured with the infrared thermal camera. This chapter demonstrates the reliability of the developed system in the high-temperature measurement induced by wheel-rail contact (objective 1), which may serve as a reference for calibrating and validating thermal contact and damage simulation models (objective 2) and enhances the understanding of the generation and development of “wheel flat” (objective 3).

Chapter 4 mainly addresses the validation of the thermomechanical FE wheel-rail contact model (objective 2). The mechanical parameters applied to the experiments presented in Chapter 3, including the wheel loads, coefficient of friction, and slip ratios (5%, 10%, and 15%), were taken as inputs for the thermomechanical FE model presented in Chapter 2. In the experiments, the camera targeting the wheel-rail contact

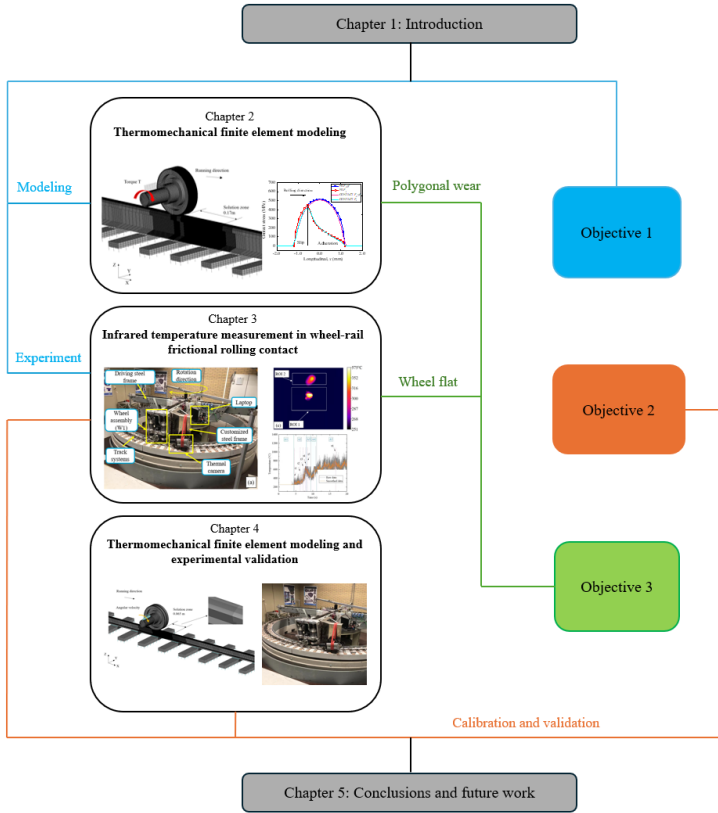


Figure 1.3: Relation between the thesis chapters and the research objectives.

area measured the rail running band temperature right after the wheel passages. The flash temperature as close as to the peak contact temperature was thus captured. The temperatures on the rail surface right behind the wheel-rail contact patch were then calculated under different slip ratio conditions using the thermomechanical FE model and compared to the measured camera-targeted flash temperature. A reasonable agreement between the measurements and simulations was achieved across varied slip ratios, indicating that the presented model is reliable for wheel-rail contact simulation with the consideration of thermal effects. Chapter 5 presents the main conclusions and recommendations for future work.



# BIBLIOGRAPHY

- [1] Q. Lian et al. “Thermo-mechanical coupled finite element analysis of rolling contact fatigue and wear properties of a rail steel under different slip ratios”. In: *Tribology International* 141 (2020), p. 105943. DOI: [10.1016/j.triboint.2019.105943](https://doi.org/10.1016/j.triboint.2019.105943).
- [2] D. Scott, D.I. Fletcher, and B.J. Cardwell. “Simulation study of thermally initiated rail defects”. In: *Proceedings of the Institution of Mechanical Engineers, Part F: Journal of Rail and Rapid Transit* 228 (2012), pp. 113–127. DOI: [10.1177/0954409712465697](https://doi.org/10.1177/0954409712465697).
- [3] J.P. Srivastava, P.K. Sarkar, and V. Ranjan. “Effects of thermal load on wheel–rail contacts: A review”. In: *Journal of Thermal Stresses* 39 (2016), pp. 1389–1418. DOI: [10.1080/01495739.2016.1216060](https://doi.org/10.1080/01495739.2016.1216060).
- [4] S. Caprioli et al. “Thermal cracking of railway wheels: Towards experimental validation”. In: *Tribology International* 94 (2016), pp. 409–420. DOI: [10.1016/j.triboint.2015.09.042](https://doi.org/10.1016/j.triboint.2015.09.042).
- [5] P.T. Zwierczyk and K. Váradi. “Thermal stress analysis of a railway wheel in sliding-rolling motion”. In: *Journal of Tribology* 136 (2014). DOI: [10.1115/1.4027544](https://doi.org/10.1115/1.4027544).
- [6] A. Ekberg and E. Kabo. “Fatigue of railway wheels and rails under rolling contact and thermal loading—an overview”. In: *Wear* 258 (2005), pp. 1288–1300. DOI: [10.1016/j.wear.2004.03.039](https://doi.org/10.1016/j.wear.2004.03.039).
- [7] A. Haidari and P.H. Tehrani. “Thermal load effects on fatigue life of a cracked railway wheel”. In: *Latin American Journal of Solids and Structures* 12 (2015), pp. 1144–1157. DOI: [10.1590/1679-78251658](https://doi.org/10.1590/1679-78251658).
- [8] R. Lewis and R. Dwyer-Joyce. “Wear mechanisms and transitions in railway wheel steels”. In: *Proceedings of the Institution of Mechanical Engineers, Part J: Journal of Engineering Tribology* 218 (2004), pp. 467–478. DOI: [10.1243/1350650042794815](https://doi.org/10.1243/1350650042794815).
- [9] A.M.S. Asih, K. Ding, and A. Kapoor. “Modelling rail wear transition and mechanism due to frictional heating”. In: *Wear* 284-285 (2012), pp. 82–90. DOI: [10.1016/j.wear.2012.02.017](https://doi.org/10.1016/j.wear.2012.02.017).
- [10] Y.Z. Chen et al. “The influence of wheel flats formed from different braking conditions on rolling contact fatigue of railway wheel”. In: *Engineering Failure Analysis* 93 (2018), pp. 183–199. DOI: [10.1016/j.engfailanal.2018.07.006](https://doi.org/10.1016/j.engfailanal.2018.07.006).
- [11] J. Ahlström and B. Karlsson. “Modelling of heat conduction and phase transformations during sliding of railway wheels”. In: *Wear* 253 (2002), pp. 291–300. DOI: [10.1016/S0043-1648\(02\)00119-9](https://doi.org/10.1016/S0043-1648(02)00119-9).

- [12] A. Böhmer, M. Ertz, and K. Knothe. “Shakedown limit of rail surfaces including material hardening and thermal stresses”. In: *Fatigue Fracture of Engineering Materials Structures* 26 (2003), pp. 985–998. DOI: [10.1046/j.1460-2695.2003.00690.x](https://doi.org/10.1046/j.1460-2695.2003.00690.x).
- [13] C. Bernsteiner et al. “Development of white etching layers on rails: simulations and experiments”. In: *Wear* 366–367 (2016), pp. 116–122. DOI: [10.1016/j.wear.2016.03.028](https://doi.org/10.1016/j.wear.2016.03.028).
- [14] S.L. Grassie et al. “Studs: a squat-type defect in rails”. In: *Proceedings of the Institution of Mechanical Engineers, Part F: Journal of Rail and Rapid Transit* 226 (2011), pp. 243–256. DOI: [10.1177/0954409711421462](https://doi.org/10.1177/0954409711421462).
- [15] R.I. Carroll and J.H. Beynon. “Rolling contact fatigue of white etching layer: Part 1”. In: *Wear* 262 (2007), pp. 1253–1266. DOI: [10.1016/j.wear.2007.01.003](https://doi.org/10.1016/j.wear.2007.01.003).
- [16] J. Jergéus et al. “Full-scale railway wheel flat experiments”. In: *Proceedings of the Institution of Mechanical Engineers, Part F: Journal of Rail* 213 (1999), pp. 1–13. DOI: [10.1243/0954409991530985](https://doi.org/10.1243/0954409991530985).
- [17] A.K. Saxena et al. “Micro fracture investigations of white etching layers”. In: *Materials Design* 180 (2019). DOI: [10.1016/j.matdes.2019.107892](https://doi.org/10.1016/j.matdes.2019.107892).
- [18] J. Seo et al. “Numerical stress analysis and rolling contact fatigue of White Etching Layer on rail steel”. In: *International Journal of Fatigue* 33 (2011), pp. 203–211. DOI: [10.1016/j.ijfatigue.2010.08.007](https://doi.org/10.1016/j.ijfatigue.2010.08.007).
- [19] J.P. Srivastava et al. “A numerical study on effects of friction-induced thermal load for rail under varied wheel slip conditions”. In: *Simulation* 95 (2018), pp. 351–362. DOI: [10.1177/0037549718782629](https://doi.org/10.1177/0037549718782629).
- [20] R. Zunsong. “An investigation on wheel/rail impact dynamics with a three-dimensional flat model”. In: *Vehicle System Dynamics* 57 (2018), pp. 369–388. DOI: [10.1080/00423114.2018.1469774](https://doi.org/10.1080/00423114.2018.1469774).
- [21] K. Handa and F. Morimoto. “Influence of wheel/rail tangential traction force on thermal cracking of railway wheels”. In: *Wear* 289 (2012), pp. 112–118. DOI: [10.1016/j.wear.2012.04.008](https://doi.org/10.1016/j.wear.2012.04.008).
- [22] J. Jaeger. “Moving sources of heat and temperature at sliding contacts”. In: *Proceedings of the Royal Society of New South Wales*. 1942, p. 222.
- [23] H. Blok. “The flash temperature concept”. In: *Wear* 6 (1963), pp. 483–494. DOI: [10.1016/0043-1648\(63\)90283-7](https://doi.org/10.1016/0043-1648(63)90283-7).
- [24] K. Knothe and S. Grassie. “Workshop on rail corrugations and out-of-round wheels”. In: *Journal of Sound and Vibration* 227 (1999), pp. 895–897. DOI: [10.1006/jsvi.1999.2053](https://doi.org/10.1006/jsvi.1999.2053).
- [25] A. Olver. “Testing transmission lubricants: the importance of thermal response”. In: *Proceedings of the Institution of Mechanical Engineers, Part G: Journal of Aerospace Engineering* 205 (1991), pp. 35–44. DOI: [10.1243/PIME\\_PROC\\_1991\\_205\\_235\\_0](https://doi.org/10.1243/PIME_PROC_1991_205_235_0).

- [26] K. Knothe and S. Liebelt. “Determination of temperatures for sliding contact with applications for wheel-rail systems”. In: *Wear* 189 (1995), pp. 91–99. DOI: [10.1016/0043-1648\(95\)06666-7](https://doi.org/10.1016/0043-1648(95)06666-7).
- [27] M. Spiriyagin et al. “Numerical calculation of temperature in the wheel-rail flange contact and implications for lubricant choice”. In: *Wear* 268 (2010), pp. 287–293. DOI: [10.1016/j.wear.2009.08.014](https://doi.org/10.1016/j.wear.2009.08.014).
- [28] M. Naeimi et al. “Thermomechanical analysis of the wheel-rail contact using a coupled modelling procedure”. In: *Tribology International* 117 (2018), pp. 250–260. DOI: [10.1016/j.triboint.2017.09.010](https://doi.org/10.1016/j.triboint.2017.09.010).
- [29] L. Ramanan, R.K. Kumar, and R. Sriraman. “Thermo-mechanical finite element analysis of a rail wheel”. In: *International Journal of Mechanical Sciences* 41 (1999), pp. 487–505. DOI: [10.1016/S0020-7403\(98\)00078-2](https://doi.org/10.1016/S0020-7403(98)00078-2).
- [30] L. Wu et al. “Thermo-elastic-plastic finite element analysis of wheel/rail sliding contact”. In: *Wear* 271 (2011), pp. 437–443. DOI: [10.1016/j.wear.2010.10.034](https://doi.org/10.1016/j.wear.2010.10.034).
- [31] K. Vo et al. “The influence of high temperature due to high adhesion condition on rail damage”. In: *Wear* 330 (2015), pp. 571–580. DOI: [10.1016/j.wear.2015.01.059](https://doi.org/10.1016/j.wear.2015.01.059).
- [32] S. Caprioli and A. Ekberg. “Numerical evaluation of the material response of a railway wheel under thermomechanical braking conditions”. In: *Wear* 314 (2014), pp. 181–188. DOI: [10.1016/j.wear.2013.11.022](https://doi.org/10.1016/j.wear.2013.11.022).
- [33] K.T. Deressa and D.A. Ambie. “Thermal load simulations in railway disc brake: a systematic review of modelling temperature, stress and fatigue”. In: *Archives of Computational Methods in Engineering* 29 (2021), pp. 2271–2283. DOI: [10.1007/s11831-021-09662-y](https://doi.org/10.1007/s11831-021-09662-y).
- [34] J. Goldak, A. Chakravarti, and M. Bibby. “A new finite element model for welding heat sources”. In: *Metallurgical Transactions B* 15 (1984), pp. 299–305. DOI: [10.1007/BF02667333](https://doi.org/10.1007/BF02667333).
- [35] E.A. Gallardo-Hernandez, R. Lewis, and R.S. Dwyer-Joyce. “Temperature in a twin-disc wheel/rail contact simulation”. In: *Tribology International* 39 (2006), pp. 1653–1663. DOI: [10.1016/j.triboint.2006.01.028](https://doi.org/10.1016/j.triboint.2006.01.028).
- [36] M. Petereson. “Two-dimensional finite element simulation of the thermal problem at railway block braking”. In: *Proceedings of the Institution of Mechanical Engineers, Part C: Journal of Mechanical Engineering Science* 216 (2002), pp. 259–273. DOI: [10.1243/0954406021524945](https://doi.org/10.1243/0954406021524945).
- [37] T. Vernersson. “Temperatures at railway tread braking. Part 1: modelling”. In: *Proceedings of the Institution of Mechanical Engineers, Part F: Journal of Rail* 221 (2007), pp. 167–182. DOI: [10.1243/0954409JRRRT57](https://doi.org/10.1243/0954409JRRRT57).
- [38] T. Vernersson and R. Lundén. “Temperatures at railway tread braking. Part 3: wheel and block temperatures and the influence of rail chill”. In: *Proceedings of the Institution of Mechanical Engineers, Part F: Journal of Rail* 221 (2007), pp. 443–454. DOI: [10.1243/09544097JRRRT91](https://doi.org/10.1243/09544097JRRRT91).

- [39] P. Baranowski et al. “Thermovision in the validation process of numerical simulation of braking”. In: *Metrology and Measurement Systems* 21 (2014), pp. 329–340. DOI: [10.2478/mms-2014-0028](https://doi.org/10.2478/mms-2014-0028).
- [40] T.C. Tszeng and V. Saraf. “A study of fin effects in the measurement of temperature using surface-mounted thermocouples”. In: *Journal of Heat Transfer* 125 (2003), pp. 926–935. DOI: [10.1115/1.1597622](https://doi.org/10.1115/1.1597622).
- [41] R. Komanduri and Z. Hou. “A review of the experimental techniques for the measurement of heat and temperatures generated in some manufacturing processes and tribology”. In: *Tribology International* 34 (2001), pp. 653–682. DOI: [10.1016/S0301-679X\(01\)00068-8](https://doi.org/10.1016/S0301-679X(01)00068-8).
- [42] O. Nosko et al. “Performance of acicular grindable thermocouples for temperature measurements at sliding contacts”. In: *Measurement* 181 (2021). DOI: [10.1016/j.measurement.2021.109641](https://doi.org/10.1016/j.measurement.2021.109641).
- [43] D. Meresse et al. “Determination of heat repartition parameters on high speed pin-on-disc tribometer by inverse heat conduction method”. In: *Key Engineering Materials*. Vol. 504–506. 2012, pp. 1061–1066. DOI: [10.4028/www.scientific.net/KEM.504-506.1061](https://doi.org/10.4028/www.scientific.net/KEM.504-506.1061).
- [44] P. Conradie et al. “Overview of work piece temperature measurement techniques for machining of Ti6Al4V”. In: *South African Journal of Industrial Engineering* 23 (2012), pp. 116–130.
- [45] Y. Wei, Y. Wu, and Z. Chen. “An experimental measurement and numerical calculation method on friction temperature rise of sliding contact pairs - taking rail/wheel contact as an example”. In: *Journal of Measurements in Engineering* 11 (2023), pp. 1–11. DOI: [10.21595/jme.2023.22974](https://doi.org/10.21595/jme.2023.22974).
- [46] X. Tian et al. “The development and use of thin film thermocouples for contact temperature measurement”. In: *Tribology Transactions* 35 (1992), pp. 491–499. DOI: [10.1080/10402009208982147](https://doi.org/10.1080/10402009208982147).
- [47] B. Tian et al. “Effect of magnetron sputtering parameters on adhesion properties of tungsten-rhenium thin film thermocouples”. In: *Ceramics International* 44 (2018), S15–S18. DOI: [10.1016/j.ceramint.2018.08.334](https://doi.org/10.1016/j.ceramint.2018.08.334).
- [48] Fraunhofer Institute for Surface Engineering and Thin Films. *Thin-film sensor technology*. Retrieved July 2024. 2024. URL: <https://www.ist.fraunhofer.de/en/expertise/sensor-technology/thin-film-sensor-technology.html>.
- [49] F.E. Kennedy, D. Frusescu, and J. Li. “Thin film thermocouple arrays for sliding surface temperature measurement”. In: *Wear* 207 (1997), pp. 46–54. DOI: [10.1016/S0043-1648\(96\)07473-X](https://doi.org/10.1016/S0043-1648(96)07473-X).
- [50] L.C. Martin and R. Holanda. “Applications of thin-film thermocouples for surface temperature measurement”. In: *NASA/SPIE Conference on Spin-Off Technologies from NASA for Commercial Sensors and Scientific Applications*. SPIE, 1994, pp. 65–76.

- [51] Y. Cui et al. “Adaptive thin film temperature sensor for bearing’s rolling elements temperature measurement”. In: *Sensors (Basel)* 22 (2022). DOI: [10.3390/s22082838](https://doi.org/10.3390/s22082838).
- [52] J. Yang et al. “Preparation of W-Ta thin-film thermocouple on diamond anvil cell for in-situ temperature measurement under high pressure”. In: *Review of Scientific Instruments* 82 (2011), p. 045108. DOI: [10.1063/1.3579515](https://doi.org/10.1063/1.3579515).
- [53] H. Deilamsalehy et al. “An automatic method for detecting sliding railway wheels and hot bearings using thermal imagery”. In: *Proceedings of the Institution of Mechanical Engineers, Part F: Journal of Rail and Rapid Transit* 231 (2016), pp. 690–700. DOI: [10.1177/09544097166638703](https://doi.org/10.1177/09544097166638703).
- [54] W. Sawczuk. “The evaluation of a rail disc brake braking process by using a thermal camera”. In: *Measurement Automation Monitoring* 61 (2015).
- [55] W. Sawczuk. “Identification of the hot spots phenomenon in brakes by using a thermal imaging camera”. In: *Proceedings of the 2016 International Conference on Quantitative InfraRed Thermography*. 2016.
- [56] J. Enthoven and H.A. Spikes. “Infrared and visual study of the mechanisms of scuffing”. In: *Tribology Transactions* 39 (1996), pp. 441–447. DOI: [10.1080/10402009608983550](https://doi.org/10.1080/10402009608983550).
- [57] K.G. Kreider, S. Semancik, and C. Olson. *Advanced thin film thermocouples*. Unpublished report or internal documentation. 1984.
- [58] Teledyne FLIR. *X6900sc MWIR - Overview*. Retrieved January 2024, from <https://www.flir.eu/support/products/x6900sc-mwir/Overview>. 2024.
- [59] J. Pearce, M. Burstow, and M. Podesta. “Understanding wheel/rail interaction with thermographic imaging”. In: *22nd International Symposium on Dynamics of Vehicles on Roads and Tracks*. 2021.
- [60] D. Yamamoto. “Improvement of method for locating position of wheel/rail contact by means of thermal imaging”. In: *Quarterly Report of RTRI* 60 (2019), pp. 65–71. DOI: [10.2219/rtriqr.60.1\\_65](https://doi.org/10.2219/rtriqr.60.1_65).
- [61] B. Firlik, T. Staśkiewicz, and M. Słowiński. “Thermal imaging of the wheel-rail interface”. In: *Proceedings of the Institution of Mechanical Engineers, Part F: Journal of Rail and Rapid Transit* (2023). DOI: [10.1177/09544097231155573](https://doi.org/10.1177/09544097231155573).
- [62] P. Zhang et al. “Comprehensive validation of three-dimensional finite element modelling of wheel-rail high-frequency interaction via the V-Track test rig”. In: *Vehicle System Dynamics* (2024), pp. 1–25. DOI: [10.1080/00423114.2024.2304626](https://doi.org/10.1080/00423114.2024.2304626).
- [63] G. Tao et al. “Experimental investigation into the mechanism of the polygonal wear of electric locomotive wheels”. In: *Vehicle System Dynamics* 56 (2018), pp. 883–899. DOI: [10.1080/00423114.2017.1399210](https://doi.org/10.1080/00423114.2017.1399210).
- [64] G. Tao et al. “An investigation into the mechanism of the out-of-round wheels of metro train and its mitigation measures”. In: *Vehicle System Dynamics* 57 (2018), pp. 1–16. DOI: [10.1080/00423114.2018.1445269](https://doi.org/10.1080/00423114.2018.1445269).

- [65] Y. Wu et al. “Experimental analysis of the mechanism of high-order polygonal wear of wheels of a high-speed train”. In: *Journal of Zhejiang University-Science A* 18 (2017), pp. 579–592. DOI: [10.1631/jzus.A1600741](https://doi.org/10.1631/jzus.A1600741).
- [66] G. Tao et al. “Measurement and assessment of out-of-round electric locomotive wheels”. In: *Proceedings of the Institution of Mechanical Engineers, Part F: Journal of Rail Rapid Transit* 232 (2018), pp. 275–287.
- [67] B. Fu, S. Bruni, and S. Luo. “Study on wheel polygonization of a metro vehicle based on polygonal wear simulation”. In: *Wear* 438–439 (2019). DOI: [10.1016/j.wear.2019.203071](https://doi.org/10.1016/j.wear.2019.203071).
- [68] D.W. Barke and W.K. Chiu. “A review of the effects of out-of-round wheels on track and vehicle components”. In: *Proceedings of the Institution of Mechanical Engineers, Part F: Journal of Rail and Rapid Transit* 219 (2005), pp. 151–175. DOI: [10.1243/095440905x8853](https://doi.org/10.1243/095440905x8853).
- [69] W. Rode, D. Müller, and J. Villman. “Results of DB AG investigations ‘out-of-round wheels’”. In: *Proceedings corrugation symposium—extended abstracts*. IFV Bahn-technik, 1997.
- [70] D. Cui et al. “Effect of the turning characteristics of underfloor wheel lathes on the evolution of wheel polygonisation”. In: *Proceedings of the Institution of Mechanical Engineers, Part F: Journal of Rail and Rapid Transit* 233 (2018), pp. 479–488. DOI: [10.1177/0954409718795760](https://doi.org/10.1177/0954409718795760).
- [71] J.C.O. Nielsen and A. Johansson. “Out-of-round railway wheels—a literature survey”. In: *Proceedings of the Institution of Mechanical Engineers, Part F: Journal of Rail and Rapid Transit* 214 (2005), pp. 79–91. DOI: [10.1243/0954409001531351](https://doi.org/10.1243/0954409001531351).
- [72] P. Meinke and S. Meinke. “Vibration, Polygonalization of wheel treads caused by static and dynamic imbalances”. In: *Journal of Sound and Vibration* 227 (1999), pp. 979–986. DOI: [10.1006/jsvi.1999.2590](https://doi.org/10.1006/jsvi.1999.2590).
- [73] X. Jin et al. “An investigation into the mechanism of the polygonal wear of metro train wheels and its effect on the dynamic behaviour of a wheel/rail system”. In: *Vehicle System Dynamics* 50 (2012), pp. 1817–1834. DOI: [10.1080/00423114.2012.695022](https://doi.org/10.1080/00423114.2012.695022).
- [74] G. Tao et al. “An investigation into the mechanism of high-order polygonal wear of metro train wheels and its mitigation measures”. In: *Vehicle System Dynamics* 59 (2020), pp. 1557–1572. DOI: [10.1080/00423114.2020.1770810](https://doi.org/10.1080/00423114.2020.1770810).
- [75] W. Ma, R. Song, and S. Luo. “Study on the mechanism of the formation of polygon-shaped wheels on subway vehicles”. In: *Proceedings of the Institution of Mechanical Engineers, Part F: Journal of Rail and Rapid Transit* 230 (2014), pp. 129–137. DOI: [10.1177/0954409714529269](https://doi.org/10.1177/0954409714529269).
- [76] W. Cai et al. “Experimental and numerical analysis of the polygonal wear of high-speed trains”. In: *Wear* 440 (2019), p. 203079. DOI: [10.1016/j.wear.2019.203079](https://doi.org/10.1016/j.wear.2019.203079).

- [77] J. Kalousek and K. Johnson. “An investigation of short pitch wheel and rail corrugations on the Vancouver mass transit system”. In: *Proceedings of the Institution of Mechanical Engineers, Part F: Journal of Rail and Rapid Transit* 206 (1992), pp. 127–135. DOI: [10.1243/PIME\\_PROG\\_1992\\_206\\_226\\_02](https://doi.org/10.1243/PIME_PROG_1992_206_226_02).
- [78] A. Johansson and C. Andersson. “Out-of-round railway wheels—a study of wheel polygonalization through simulation of three-dimensional wheel–rail interaction and wear”. In: *Vehicle System Dynamics* 43 (2006), pp. 539–559. DOI: [10.1080/00423110500184649](https://doi.org/10.1080/00423110500184649).
- [79] B. Wu et al. “Effect of the unstable vibration of the disc brake system of high-speed trains on wheel polygonalization”. In: *Proceedings of the Institution of Mechanical Engineers, Part F: Journal of Rail and Rapid Transit* 234 (2020), pp. 80–95. DOI: [10.1177/0954409719833787](https://doi.org/10.1177/0954409719833787).
- [80] B. Morys. “Enlargement of out-of-round wheel profiles on high speed trains”. In: *Journal of Sound and Vibration* 227 (1999), pp. 965–978. DOI: [10.1006/jsvi.1999.2055](https://doi.org/10.1006/jsvi.1999.2055).
- [81] J.J. Kalker. “A fast algorithm for the simplified theory of rolling contact”. In: *Vehicle System Dynamics* 11 (2007), pp. 1–13. DOI: [10.1080/00423118208968684](https://doi.org/10.1080/00423118208968684).
- [82] M. Meywerk. “Polygonalization of railway wheels”. In: *Archive of Applied Mechanics* 69 (1999), pp. 105–120. DOI: [10.1007/s004190050208](https://doi.org/10.1007/s004190050208).
- [83] J.J. Kalker. “Survey of wheel–rail rolling contact theory”. In: *Vehicle System Dynamics* 8 (2007), pp. 317–358. DOI: [10.1080/00423117908968610](https://doi.org/10.1080/00423117908968610).
- [84] C. Andersson and A. Johansson. “Prediction of rail corrugation generated by three-dimensional wheel–rail interaction”. In: *Wear* 257 (2004), pp. 423–434. DOI: [10.1016/j.wear.2004.01.006](https://doi.org/10.1016/j.wear.2004.01.006).
- [85] Z. Shen, J. Hedrick, and J. Elkins. “A comparison of alternative creep force models for rail vehicle dynamic analysis”. In: *Vehicle System Dynamics* 12 (2007), pp. 79–83. DOI: [10.1080/00423118308968725](https://doi.org/10.1080/00423118308968725).
- [86] N. Burgelman et al. “Influence of wheel–rail contact modelling on vehicle dynamic simulation”. In: *Vehicle System Dynamics* 53 (2015), pp. 1190–1203. DOI: [10.1080/00423114.2015.1039550](https://doi.org/10.1080/00423114.2015.1039550).
- [87] M. Sh. Sichani, R. Enblom, and M. Berg. “A novel method to model wheel–rail normal contact in vehicle dynamics simulation”. In: *Vehicle System Dynamics* 52 (2014), pp. 1752–1764. DOI: [10.1080/00423114.2014.961932](https://doi.org/10.1080/00423114.2014.961932).
- [88] Y. Sun, W. Zhai, and Y. Guo. “A robust non-Hertzian contact method for wheel–rail normal contact analysis”. In: *Vehicle System Dynamics* 56 (2018), pp. 1899–1921. DOI: [10.1080/00423114.2018.1439587](https://doi.org/10.1080/00423114.2018.1439587).
- [89] M. Sh. Sichani, R. Enblom, and M. Berg. “An alternative to FASTSIM for tangential solution of the wheel–rail contact”. In: *Vehicle System Dynamics* (2016), pp. 748–764. DOI: [10.1080/00423114.2016.1156135](https://doi.org/10.1080/00423114.2016.1156135).
- [90] X. Zhao and Z. Li. “The solution of frictional wheel–rail rolling contact with a 3D transient finite element model: Validation and error analysis”. In: *Wear* 271 (2011), pp. 444–452. DOI: [10.1016/j.wear.2010.10.007](https://doi.org/10.1016/j.wear.2010.10.007).

- [91] Z. Yang, X. Deng, and Z. Li. “Numerical modeling of dynamic frictional rolling contact with an explicit finite element method”. In: *Tribology International* 129 (2019), pp. 214–231. DOI: [10.1016/j.triboint.2018.08.028](https://doi.org/10.1016/j.triboint.2018.08.028).
- [92] X. Deng, Z. Qian, and R. Dollevoet. “Lagrangian explicit finite element modeling for spin-rolling contact”. In: *Journal of Tribology* 137 (2015), p. 041401. DOI: [10.1115/1.4030709](https://doi.org/10.1115/1.4030709).
- [93] Z. Wei et al. “3D FE modelling and validation of frictional contact with partial slip in compression–shift–rolling evolution”. In: *International Journal of Rail Transportation* 4 (2015), pp. 20–36. DOI: [10.1080/23248378.2015.1094753](https://doi.org/10.1080/23248378.2015.1094753).
- [94] K. Liu and L. Jing. “A finite element analysis-based study on the dynamic wheel–rail contact behaviour caused by wheel polygonization”. In: *Proceedings of the Institution of Mechanical Engineers, Part F: Journal of Rail and Rapid Transit* 234 (2020), pp. 1285–1298. DOI: [10.1177/0954409719891549](https://doi.org/10.1177/0954409719891549).
- [95] L. Han, L. Jing, and K. Liu. “A dynamic simulation of the wheel–rail impact caused by a wheel flat using a 3-D rolling contact model”. In: *Journal of Modern Transportation* 25 (2017), pp. 124–131. DOI: [10.1007/s40534-017-0131-0](https://doi.org/10.1007/s40534-017-0131-0).
- [96] J.J. Kalker. *Three-dimensional elastic bodies in rolling contact*. Springer Science Business Media, 2013.

# 2

## A FINITE ELEMENT THERMOMECHANICAL ANALYSIS OF THE DEVELOPMENT OF WHEEL POLYGONAL WEAR

*Polygonal wear is a type of damage commonly observed on the railway wheel tread. It induces wheel-rail impacts and consequent train/track components failure. This study presents a finite element (FE) thermomechanical wheel-rail contact model, which is able to cope with the three possible generation and development mechanisms of polygonal wear: initial defects, thermal effects, and structural dynamics. The polygonal wear-induced impact contact and further development of wear are simulated. The simulated elastic contact solutions are verified against the program CONTACT. Different material properties (elastic, elasto-plastic and elasto-plastic-thermo, i.e., with thermal softening) and initial polygonal profiles are then applied to the FE model to investigate the influence of wheel/rail material and wear amplitude on wheel-rail contact stress and wear development. The simulations indicate that the wheel-rail impact-induced temperature may reach up to 362 °C at the contact interface, and the high temperature at the contact area influences wheel-rail contact stress and wear depth.*

---

This chapter has been published as: He, C., Yang, Z., Zhang, P., Li, S., Naeimi, M., Dollevoet, R., Li, Z. (2024). A finite element thermomechanical analysis of the development of wheel polygonal wear. *Tribology International*, 195, 109577.

## 2.1. INTRODUCTION

**P**OLYGONAL wear is typical damage that occurs on the wheels of locomotives, metros, and high-speed trains [1–3]. High-amplitude vibrations induced by the impacts between rails and polygonal wheels accelerate train and track degradation and radiate high-level noises [4]. Severe polygonal wear threatens the safety of railway operations and adversely affects ride comfort of passengers [5]. To mitigate the effects of polygonal wear, a better understanding of its initiation and development mechanisms is needed.

The initiation and progression of polygonal wear on railway wheels can be influenced by three principal mechanisms, as identified in the previous research. Firstly, initial defects play a crucial role, arising from factors such as the wheel re-profiling process [6, 7], uneven material properties [8], and static and dynamic imbalances [9]. Secondly, the natural vibrations within the train-track system may contribute to polygonal wear formation, driven by resonance frequencies from the vehicle components (e.g., wheelsets [10, 11], bogie frames [3], and linear induction motors [12]), track components (e.g., rail bending vibration modes [13]), and train-track interactions including stick-slip oscillations [14], P2 resonance [15], and frictional self-excited vibrations [16]. Lastly, the thermal effect between the wheel tread and braking blocks [17, 18] may further influence the development of polygonal wear.

Studies on the formation and growth of wheel polygonal wear have been conducted with numerical modeling. A general approach is to simulate wheel-rail contact and consequent wear by coupling a multibody dynamics (MBD) model with a wear prediction model considering initial defects [19]. The initial wheel defects and wheel/rail structural dynamics, as possible mechanisms of wheel polygonal wear generation and development, can be considered in the MBD models. The initial polygonal wear profile of wheel could be simplified as one or several mixed harmonic waves. The number of waves along the wheel circumference is regarded as the ‘order’ of the polygonal wear. The core connections between a MBD model and a wear model are wheel-rail contact solutions, i.e., the normal and tangential contact stresses and micro-slip distributions.

Morys [20] built up a three-dimensional (3D) MBD model of an ICE-1 carriage. Hertzian theory and FASTSIM [21] were used to calculate the normal and tangential contact solutions, respectively. The study presented the simulation results of the evolution of the worn profile, which was assumed to be proportional to the wear energy, and concluded that the low-order polygonal wear could be developed into higher-order harmonics. Meywerk [22] built up an MBD model with a wheelset, in which the wheel axle and rims were treated as flexible beams, and the bogie was simplified as a rigid frame. Kalker’s linear theory [23] and Hertzian theory were employed to deal with the contact solutions. The study concluded that the phase shift of the left and right wheel profiles may influence the growth of polygonal wear, and the first and second bending modes of the wheelset axle are dominant contributors to polygonal wear growth. Andersson and Johansson [15, 24] developed a model incorporating multi-rigid body wheelsets and a bogie frame, as well as finite element rails. Hertzian theory and Shen-Hedrick-Elkins model [25] were employed to calculate contact solutions. They concluded that the P2 resonance could cause the 5th, 6th, and 7th-order polygonal wear, and the track modes are the main causes of the 14th to 20th-order polygonal wear. To deal with non-elliptical wheel-rail contact that occurs in the real-life operations [26], some MBD models applied

non-Hertzian contact theories, e.g., ANALYN [27], modified Kik–Piotrowski [28] and FaS-trip [29]. However, because wheel/rail material nonlinearities cannot be treated properly with the aforementioned contact methods, hardly can the MBD models accurately simulate polygonization-induced impact contact, where plasticity occurs, and be used to predict the further development of wear. To cope with the material nonlinearities, complex wheel-rail contact geometry, and dynamic effects involved in the wheel-rail interactions, explicit finite element (FE) contact modeling [30] has been broadly adopted to calculate wheel-rail dynamic contact, such as the polygonal wear-induced and flat-induced wheel dynamic responses [31, 32]. However, few of them, if any, have been combined with wear models to analyze the initiation and further development of polygonal wear.

In addition, it has been found that the heat induced by wheel-rail frictional contact may significantly influence the material properties and consequently the evolution of wear [33]. Hence, friction-induced heat has been considered in some FE contact models. Asih [34] developed a two-dimensional (2D) FE model which applied an analytical moving heat flux on the rail to investigate the thermal effect on the wear rate of the rail. It was concluded that the transition from mild to severe wear could happen when the temperature is above 350 °C. Wu et al. [35] built a 2D FE rail model and applied an instantaneous heat source to analyze the thermal effect on the rail. They concluded that the thermal effect influences the residual stress, deformation, and plastic strain of the rail. Vo et al. [36] compared the wheel-rail contact temperatures calculated with a 2D model and a 3D model, and found that the peak temperature on the rail calculated with the 2D model was overestimated because the thermal energy emission in the transverse direction was overlooked. Besides the limitation of the Hertzian elastic assumption used in the moving heat sources, all the studies above prescribed the thermal effect in the wheel-rail contact load. In other words, the thermal effect that should be influenced by frictional contact was not updated in the simulations. To obtain more accurate contact solutions with the consideration of thermal effect, Naeimi et al. [37] proposed a 3D dynamic FE wheel-rail contact model that couples the mechanical and thermal load to investigate the stress-strain responses and flash temperature on the rail surface. Considering the temperature-dependent nonlinear material properties, the temperature and stress field in the contact patch with a single wheel passage were obtained. The study concluded that the thermal softening of material induces higher von-Mises stresses and larger plastic deformation. The thermomechanical FE modeling approach proposed in [37] was then applied by Lian et al. [38] to study the fatigue life and wear behavior of a rail with multiple wheel loads. The thermomechanical FE model has been applied to study the stress and the flash temperature of the corrugated rail [39]. To the best of the authors' knowledge, an analysis of thermal effect on wheel polygonal wear has not been conducted.

In this study, a 3D FE thermomechanical wheel-rail contact model is presented to simulate polygonal wheel-rail interactions. The model is able to cope with the three possible generation and development mechanisms of polygonal wear: initial defects, thermal effect, and structural dynamics. In combination with Archard's wear model [40], the further development of wear is predicated. The FE model is built up based on the parameters of an in-house test rig—V-Track [41, 42], to facilitate the next-step model validation. Kalker's CONTACT program [43] is used to verify the elastic contact solutions obtained

with the proposed FE model. Simulations using different wheel/rail material properties and initial wheel profiles are then conducted to investigate the influences of plasticity, the thermal effect, and initial defects on wheel-rail contact stress distributions and wear development.

## 2.2. MODELING

### 2.2.1. A FINITE ELEMENT (FE) MODEL

Figure 2.1 shows the 1/7 downscaled V-Track test rig and the FE thermomechanical wheel-rail contact model. The parameters used in the FE model are listed in Table 2.1. In the V-Track, the wheel assembly mounted on a steel frame can be powered by two motors and run along the ring track. One motor drives the steel frame together with the wheel assembly to run with a controllable translational velocity, and the other can provide a negative or positive torque to the rolling wheel to simulate a braking or traction loading condition. The V-Track has been proven to be able to reproduce real-life wheel-rail frictional rolling contact and to investigate the related problems [44, 45]. In addition, the V-Track demonstrates notable dynamic similarity to real vehicle-track systems [46, 47], which is important for the reproduction of wheel polygonal wear. Figure 2.1(a) (and a close-up in Figure 2.2) shows an example of wheel polygonal wear that was successfully produced in the V-Track test rig with the operational condition that the wheel speed was 13 km/h, and the wheel-rail normal, lateral and longitudinal contact forces were 4000 N (corresponding to the contact pressure of 1100 MPa), 80 N, and 1800 N, respectively.

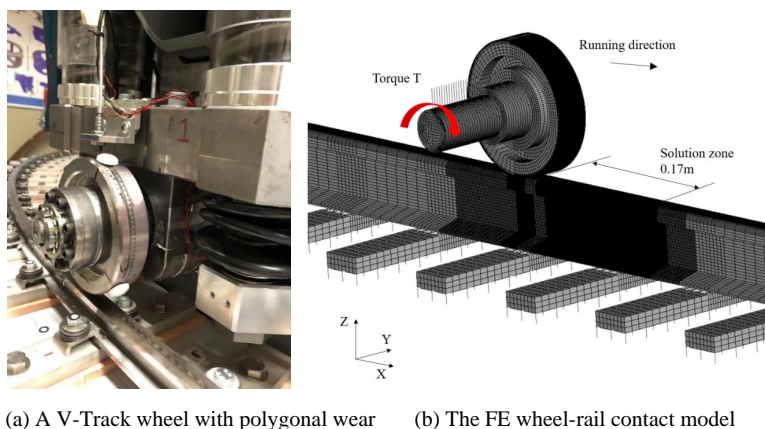


Figure 2.1: The V-Track test rig and corresponding 3D FE thermomechanical wheel-rail contact model.

In the FE model, the cylindrical wheel, rail, and sleepers are modeled with 8-node solid elements, as shown in Figure 2.1(b). The fastenings and the ballast (physically modeled with clamps and rubber pads in the V-Track) are modeled with spring-damper elements. The car body and bogie, which are physically modeled in the V-Track with the steel frame, are simplified as lumped mass elements connected to the wheel axle with spring-damper elements which represent the primary suspension. The total length of

Table 2.1: Input parameters of the FE model

Symbol (units)	Parameters	Value
$\rho_0$ (kg/m <sup>3</sup> )	The density of wheel, rail, and sleeper material	7800
$m$ (kg)	Total weight of the mass element	40
$L$ (m)	The initial length of the primary suspension	0.0574
$K_p$ (kN/m)	Stiffness of the primary suspension	11.5
$C_p$ (N·s/m)	Damping of the primary suspension	5
$K_f$ (kN/m)	Stiffness of the fastener	2220
$C_f$ (N·s/m)	Damping of the fastener	21
$K_b$ (kN/m)	Stiffness of the ballast	370
$C_b$ (N·s/m)	Damping of the ballast	32
$f$	Coefficient of friction	0.45
$R$ (mm)	Initial radius of the wheel	65
$R'$ (mm)	Principal radii of rail	120
$T_0$ (°C)	Ambient temperature	25

the rail model is 3.07 m (with 24 sleeper spans), including a solution zone with a length of 0.17 m. To increase computation efficiency, a partially refined mesh strategy is applied. The solution zones on the wheel and rail have a fine mesh with a size of 0.14 mm (along the  $x$ -axis)  $\times$  0.20 mm (along the  $y$ -axis)  $\times$  0.20 mm (along the  $z$ -axis). The directions of the axis can be found in Figure 2.1(b). The minor axis of the contact patch includes 20 elements along the running direction, which is sufficient for obtaining accurate contact solutions, as reported in [48].

An implicit-explicit sequential analysis is conducted to simulate wheel-rail frictional rolling contact. A static equilibrium of wheel loading on the rail is first performed in the commercial software ANSYS, in which the longitudinal and lateral degrees of freedom of the wheel axle are constrained. An explicit analysis is then conducted to simulate wheel rolling along the rail. The longitudinal constraint of the wheel axle is released in the explicit simulation. This study simulates wheel rolling with high longitudinal creepage, although high lateral creepage may contribute to the formation of polygonal wear [10, 11, 14] and can be simulated with the explicit FE analysis [49]. That is because this study aims to investigate the polygonal wear observed in the V-Track (shown in Figure 2.1(a)), in the operational conditions of which the lateral creepage was controlled to a very small level, and the measured wheel-rail lateral contact force was only 1/22 of the longitudinal force. In the implicit-explicit sequential analysis, the nodal displacements obtained by the static equilibrium are taken as initial conditions for the explicit analysis. A positive torque is applied to the axle to simulate a driving wheel case. Three different types of materials, listed in Table 2.2, are applied to the wheel and rail models to investigate the influences of material plasticity and thermal effect on wheel-rail contact stress and wear development. The elasto-plastic material is simulated by a bilinear representation. The thermal softening is simulated by using temperature-dependent mechanical and thermal material parameters listed in Tables 2.3 and 2.4, respectively [37].

The thermal conductivity is scaled by a factor of 1/7, according to the scaling strat-

egy [50], to be consistent with the scale of V-Track. The calculations of the contact stress and friction-induced temperature rise (i.e., thermal effect) are coupled in the FE thermomechanical wheel-rail contact model [37].

Table 2.2: The material models used in the simulations [30]

Material Type	Parameters	Value (unit)
Elastic	Young's modulus, $E$ Poisson's ratio, $\nu$	210 (GPa) 0.3
Elasto-plastic	Young's modulus, $E$ Poisson's ratio, $\nu$ Yield stress, $\sigma_y$ Tangent modulus, $G$	210 (GPa) 0.3 483 (MPa) 21 (GPa)
Elasto-plastic-thermo with thermal softening	See the mechanical and thermal parameters in Tables 2.3 and 2.4	

Table 2.3: Temperature-dependent mechanical material parameters [37]

Temperature, $T$ (°C)	Young's modulus, $E$ (GPa)	Poisson's ratio, $\nu$	Yield stress, $\sigma_y$ (MPa)	Coefficient of thermal expansion, $\alpha$ ( $\times 10^{-6}$ °C $^{-1}$ )	Hardening modulus, $E_p$ (GPa)
24	213	0.295	483.0	9.89	22.7
230	201	0.307	485.1	10.82	26.9
358	193	0.314	418.8	11.15	21.3
452	172	0.320	332.4	11.27	15.6
567	102	0.326	151.1	11.31	6.2
704	50	0.334	45.0	11.28	1.0
900	43	0.345	13.4	11.25	0.1

### 2.2.2. POLYGONAL WHEEL PROFILE

The polygonal worn profile applied to the wheel model is assumed as a harmonic wave given in equation (2.1):

$$R_p(\theta) = R + A \cdot \sin(N \cdot \theta) \quad (0^\circ \leq \theta \leq 360^\circ) \tag{2.1}$$

where  $R_p(\theta)$  is the varying radius of a polygonal wheel;  $R$  is the original radius of a round

Table 2.4: Temperature-dependent thermal material parameters [37]

Temperature, $T$ ( $^{\circ}\text{C}$ )	Specific heat capacity, $c$ ( $\text{J}/\text{kg}^{\circ}\text{C}$ )	Thermal conductivity, $\lambda$ ( $\text{W}/\text{m}^{\circ}\text{C}$ )
0	419.5	8.53
350	629.5	5.84
703	744.5	4.32
704	652.9	4.31
710	653.2	4.29
800	657.7	3.57
950	665.2	3.86
1200	677.3	4.35

wheel;  $A$  is the amplitude of the polygonal wear; and  $N$  is the order number of the polygonal wear.  $N = 68$  is used in this study, corresponding to a wavelength of 6 mm, which is consistent with the observed wear wavelength of the V-Track wheel shown in Figure 2.2.  $\theta$  is the corresponding angle in the polar coordinate. In this study,  $\theta$  also indicates the angular displacement of the wheel rolling over the original position  $O$ , which increases from 0 to 90 degrees in the simulations, as shown schematically in Figure 2.3.

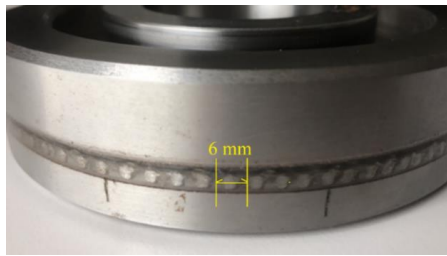


Figure 2.2: Observed polygonal wear on a V-Track wheel with the cylindrical tread.

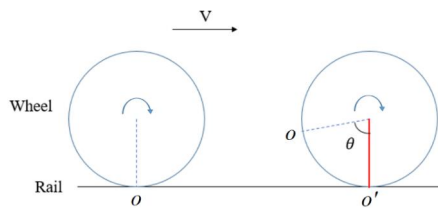


Figure 2.3: The angular displacement that the wheel rolls over the rail in the simulation.

### 2.2.3. WEAR SIMULATION

Archard's wear model has been proven to be reliable for wheel-rail contact-induced wear predictions [51, 52]. It is employed in this study to predict wear development induced by

polygonal wheel-rail impact, as given in equation (2.2):

$$\Delta r = k \frac{NS}{H} \quad (2.2)$$

where  $\Delta r$  is material loss depth,  $k$  is wear coefficient,  $N$  is normal contact stress between contact surfaces,  $S$  is relative sliding distance between two contact surfaces, and  $H$  is Vickers' hardness of the material. The wear coefficient  $k$  can be identified based on the coefficient map presented in [51], along with the contact load and relative sliding velocity calculated with the FE wheel-rail contact model. According to the wheel-rail contact simulation results (to be presented in Section 2.4), the wear coefficient  $k$  is taken as  $10^{-3}$ , which is based on the measurement of the wear depth of the wheel in Figure 2.2. The Vicker's hardness  $H$  is 261 MPa, which was measured via a hardness test on a V-Track wheel at ambient temperature. The thermal effect and influence of plastic deformation on the hardness are ignored in the simulation. It should be noted that, within the studied temperature range, yield stress is temperature-dependent, and material hardness is closely linked to yield stress, as shown in Table 2.3. When the temperature exceeds 230 °C, the material softens, leading to increased wear. If the accumulation of plastic deformation from multiple wheel passes is considered, the material hardness will increase. Although the present study does not account for hardness variations, future wear calculations will incorporate the temperature-dependent changes in material hardness to improve the accuracy of the wear prediction. The wear depth of the wheel can thus be calculated using equation (2.2) at each time step based on the FE simulation results, i.e., micro-slip and the surface contact stress.

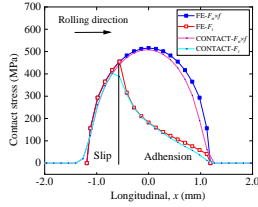
## 2.3. MODEL VERIFICATION

ACCURATE calculations of contact are crucial for wear predictions. To verify the accuracy of the FE contact solutions obtained in this study, they are compared to the solutions calculated with the widely-accepted CONTACT program. Because CONTACT deals with steady-state elastic contact without the consideration of the thermal effect, the contact solutions obtained with the two elastic FE models (here named model E and model E-POL, for the ones with the round and polygonal wheel profiles, respectively) are compared to the CONTACT solutions in Sections 2.3.1 and 2.3.2. For model E-POL, the amplitude of the polygonal profile  $A$  is 0.029 mm, which equals to 1/7 (the scale of the V-Track) of the manufacturing tolerance of high-speed trains (where wheel polygons are commonly observed)—0.2 mm [6].

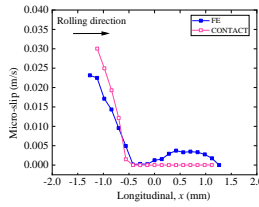
### 2.3.1. ELASTIC CONTACT WITH A ROUND WHEEL

A 87.75 N·m constant positive torque is first applied to model E, resulting in a traction coefficient of 0.27. A partial-slip contact case could then be simulated (considering the traction coefficient is smaller than the coefficient of friction 0.45 listed in Table 2.1), which is a critical characteristic of the frictional rolling contact [53]. Figures 2.4(a), (b), and (c) show the comparisons between the FE contact solutions (model E at instant 9.84 ms) and CONTACT results in terms of the traction bound (i.e., the normal stress  $F_n$  times the coefficient of friction  $f$ ), surface shear stress  $F_t$ , and micro-slip distributions. The slip and adhesion area within the contact patch can be distinguished by compar-

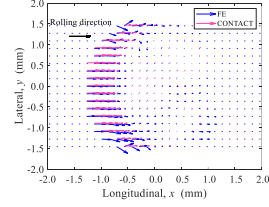
ing the surface shear stress to the traction bound: the contact is in adhesion when the surface shear stress is below the traction bound, and the contact is in slip when they are equal.



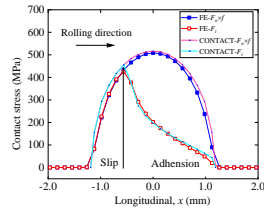
(a) Stress distribution with a constant torque and  $\zeta=0.0001$



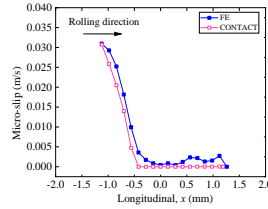
(b) Micro-slip at  $y=0$  mm with a constant torque and  $\zeta=0.0001$



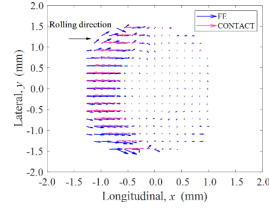
(c) Micro-slip with a constant torque and  $\zeta=0.0001$



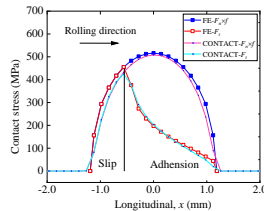
(d) Stress distribution with a functional torque and  $\zeta=0.0001$



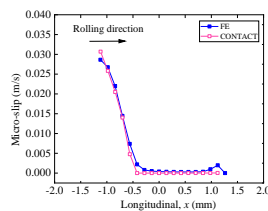
(e) Micro-slip at  $y=0$  mm with a functional torque and  $\zeta=0.0001$



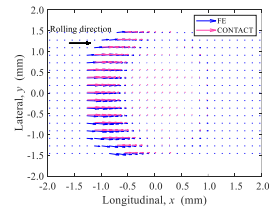
(f) Micro-slip with a functional torque and  $\zeta=0.0001$



(g) Stress distribution with a functional torque and  $\zeta=0.1$



(h) Micro-slip at  $y=0$  mm with a functional torque and  $\zeta=0.1$



(i) Micro-slip with a functional torque and  $\zeta=0.1$

Figure 2.4: Comparisons between the contact solutions of the FE models and CONTACT program (The damping coefficient is denoted as  $\zeta$ ).

It could be seen that the contact stresses, i.e., the traction bound and surface shear stress, calculated with the FE model and CONTACT agree reasonably with each other. Differences are observed in the micro-slip calculations in the center line along the longitudinal axis ( $y = 0$  mm) and in the vector graph within the contact patch, as shown in Figures 2.4(b) and (c), respectively. The differences may result from the dynamic effects inherently involved in the FE modeling [48] but ignored in CONTACT. A better agreement can be achieved when the dynamic effects are mitigated in the FE modeling, e.g., by applying a gradually increased functional driving torque to facilitate the dynamic relaxation [54, 55]. This study represents the torque applied to the FE model with a cosine

function, as given in equation (2.3):

$$T(t) = \begin{cases} \frac{M}{2(1-\cos(\frac{\pi t}{t_0}))}, & t < t_0 \\ M, & t \geq t_0 \end{cases} \quad (2.3)$$

where  $T(t)$  is the time-dependent torque,  $t$  is the running time of the wheel,  $M$  is the maximum value of the torque, and  $t_0$  is the duration required to reach  $M$ . The torque keeps constant after  $M$  is reached. Here,  $M = 87.75\text{N}\cdot\text{m}$  and  $t_0 = 2\text{ms}$ . Figures 2.4(d) and (e) show that when the functional torque is applied, the contact stresses and micro-slips at  $y = 0\text{mm}$  calculated with the FE model and CONTACT have a better agreement. However, Figures 2.4(c) and (f) show that in the FE contact solution, the micro-slips have more significant lateral components close to the top and bottom edges of the contact patch. To further mitigate the dynamic effects of the FE solutions, the Rayleigh damping coefficient used in the FE model is increased from 0.0001 to 0.1. Figures 2.4(g), (h), and (i) compare the contact solutions obtained with the FE model E using the functional torque and a larger damping coefficient of 0.1 to those obtained with CONTACT. Excellent agreements are achieved, indicating that reliable contact solutions can be provided by the proposed FE model.

### 2.3.2. ELASTIC CONTACT WITH A POLYGONAL WHEEL

The radius of curvature of the wheel in the rolling direction, as a critical input for CONTACT, is adjusted to represent a polygonal wheel, which can be calculated with equations (2.4) and (2.5) [56]:

$$k(\theta) = \frac{\left( (x')^2 + (z')^2 \right)^{3/2}}{|x''z' - x'z''|} \quad (2.4)$$

$$\begin{cases} x = R_p(\theta) \cos(\theta) \\ z = R_p(\theta) \sin(\theta) \end{cases} \quad (2.5)$$

where  $k(\theta)$  is the radius of curvature of the wheel in the rolling direction, and  $\theta$  is the angular displacement of the wheel defined in Figure 2.3.  $x$  and  $z$  represent the longitudinal and vertical coordinates of the node in the center line of the wheel tread ( $y = 0\text{mm}$ ) along the polygonal profile.  $x'$  and  $z'$  are the first-order derivatives.  $x''$  and  $z''$  are the second-order derivatives. The contact solutions calculated with the elastic polygonal wheel model, i.e., model E-POL, at 15 time steps (denoted as t1 to t15 in Figure 2.5) are then analyzed in Figures 2.6 and 2.7. Figure 2.5 shows the wheel radial deviation from the original radius of a round wheel (i.e., the worn profile defined in equation (2.1)) as a function of angular displacement  $\theta$ , which covers two wavelengths of the prescribed polygonal wear. 15 time steps with an interval of 0.12 ms are selected for the analysis to cover the wheel passage within one wavelength (between  $36^\circ$  and  $41.5^\circ$ ). At t5 and t6, two-point wheel-rail contact occurs, and the corresponding contact positions along the wheel profile are indicated by the orange and pink vertical lines. Because prescribing the four principal radii for contact geometry in CONTACT cannot deal with two-point contact, only the FE contact solutions at t5 and t6 are displayed in Figures 2.6 and 2.7. The

contact positions of the single-point contact cases (t1 ~ t4, and t7 ~ t15) are indicated by blue vertical lines in Figure 2.5.

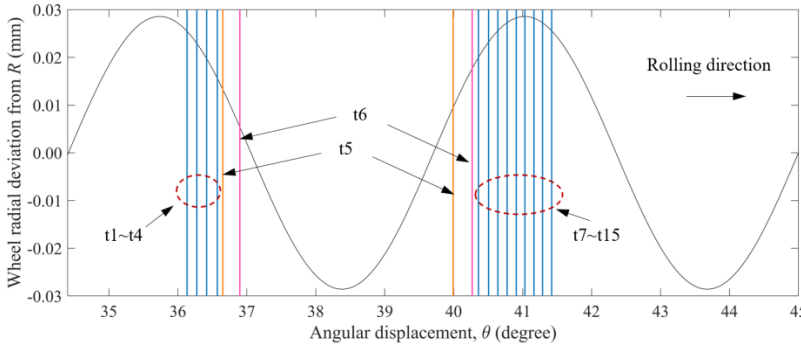


Figure 2.5: The contact positions along the polygonal profile at 15 time steps.

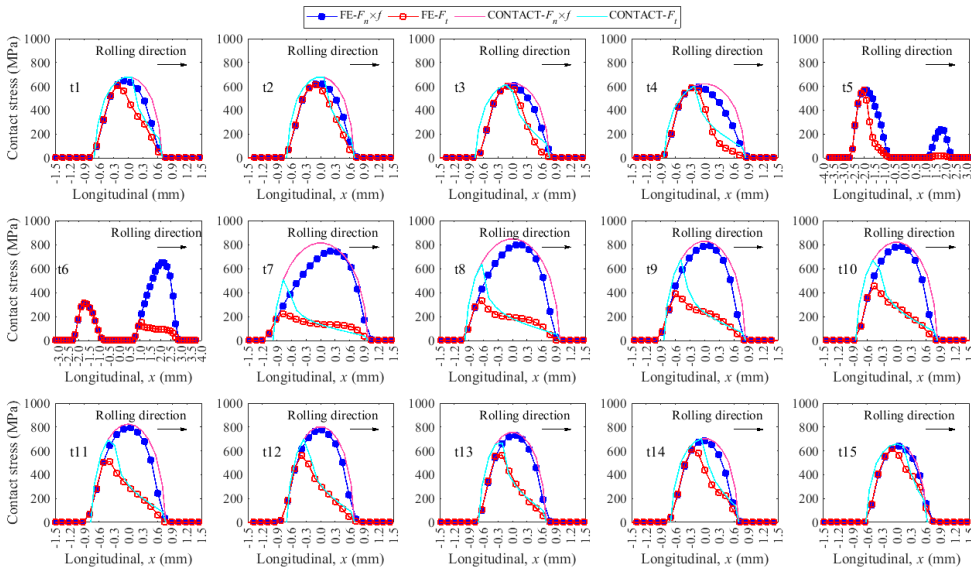


Figure 2.6: Comparison between the contact stresses of the FE model E-POL and CONTACT.

It can be seen from Figure 2.6, that the contact stress varies significantly from t1 to t15 with the change of the wheel contact radius. The proportion of the adhesion area increases slightly from t1 to t4. The surface stresses are not continuous at instants t5 and t6 due to the two-point contact. At instant t5, partial slip occurs in the 'left' contact patch, while the adhesion area occupies the whole 'right' contact patch. At instant t6, the 'left' contact patch is in slip, and partial slip occurs in the 'right' contact patch with a small proportion of slip area. A wheel-rail impact occurs after two-point contact, indicated

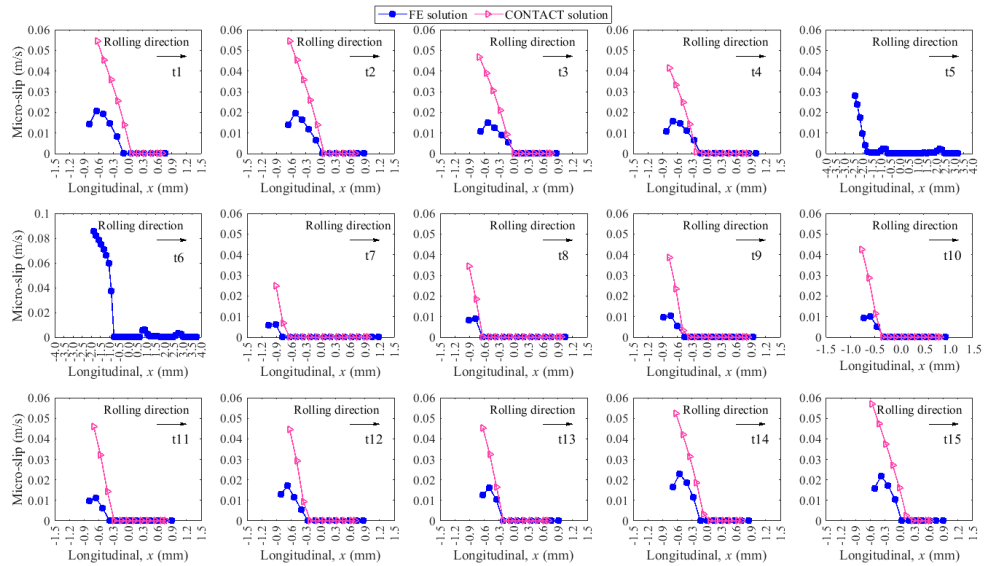


Figure 2.7: Comparison between the micro-slip along the axis ( $y=0$  mm) of the FE model E-POL and CONTACT.

by a significant increase in contact area as well as a high proportion of adhesion area at instants  $t7 \sim t8$ . A similar phenomenon has been observed when simulating a wheel-rail impact at an insulated rail joint [53]. The proportion of the adhesion area then decreases from  $t9$  to  $t15$  due to the rebound effect.

In Figure 2.6, the traction bounds, especially the maximum normal contact stress, calculated with the FE model are generally in line with the results calculated with CONTACT, despite the presence of the polygonal profile. However, it is worth noticing that at  $t7$  and  $t8$  the peak normal contact stress moves forward to the leading side of the contact patch in the FE solutions due to impact, where the dynamic effects play an important role. The dynamic effects may also influence the maximum shear stress located at the border of the slip and adhesion regions: the FE solutions are lower from  $t7$  to  $t15$ .

The corresponding micro-slip distributions along the longitudinal axis of the contact patch ( $y = 0$  mm) calculated with the FE model and CONTACT are compared in Figure 2.7. The peak values of the micro-slip calculated with CONTACT are higher than the FE solutions, similar to the case shown in Figure 2.4(b). The difference in the calculated micro-slips is also believed to be attributed to the dynamic effect since it can be effectively mitigated by applying a functional torque, as shown in Figures 2.4(e) and (h). Here, in Figure 2.7, although the functional torque has been applied in the FE simulation, the dynamic effect can still be remarkable because of the wheel polygonal profile and consequently the variation in contact geometry. The deviation in the micro-slip solutions suggests that the FE contact modeling with a better representation of dynamic contact should be applied to the polygonal wheel-rail impact contact study and further prediction of polygonal wear development.

## 2.4. RESULTS AND DISCUSSIONS

### 2.4.1. SIMULATION CASES

Simulations using different wheel/rail material properties and wheel profiles are then conducted to investigate the influences of plasticity, thermal effect, and wheel polygonization on wheel-rail contact stress distributions and consequent wear development with a single wheel passage. Cyclic wheel loading, the accumulation of contact temperature, and their influences on polygonal wear growth can be analyzed using the explicit FE approach [57] in future research. Three different wheel/rail material properties (listed in Table 2.2) are applied to the FE models, as summarized in Table 2.5. Corresponding to the three material models, the FE wheel-rail contact models are named after E-POL, EP-POL, and EPT-POL, respectively. Note that model E-POL used here is the one used also in Section 2.3 but with a different setup of torque: a larger torque of 162.50 N·m is applied to model E-POL, as well as the other two models, in this section to achieve full slip wheel-rail contact. This is necessary for the examination of thermal effect, which plays a significant role when the wheel-rail slip ratio is high [37, 38]. Three different amplitudes of polygonal profiles are then applied to model EP-POL and model EPT-POL, and the results are compared in Section 2.4.3 to examine the influence of initial defects on wear development.

Table 2.5: Simulation models with polygonal profile and different material properties.

Material type	Simulation models (abbreviation)	Initial wear amplitude $A$ (mm)
Elastic	E-POL	0.2
Elasto-plastic	EP-POL	0.1, 0.2, 0.3
Elasto-plastic-thermo with thermal softening	EPT-POL	0.1, 0.2, 0.3

### 2.4.2. CONTACT STRESS AND WEAR

#### 2.4.2.1 RESULTS AT ONE TIME STEP

Section 2.3 has demonstrated that the presented FE contact model is able to provide reliable elastic contact solutions for polygonal wear analysis. In this section, we first compare the normal contact stress and wear depth calculated with the three FE models listed in Table 2.5 at two different time steps (denoted as  $t_1$  and  $t_2$  in Figure 2.10 and Figure 2.11) because different wear phenomena are observed. The results are shown in Figure 2.8 and Figure 2.9, respectively. Because full slip wheel-rail contact is simulated, where the surface shear stress equals the traction bound and a constant coefficient of friction is used in this study, the distributions of the normal contact stress and shear stress follow the same pattern.

Figure 2.8(a) shows that the normal contact stress obtained with the elastic model (i.e., model E-POL) is higher than those of the elasto-plastic models (i.e., model EP-POL and model EPT-POL), and the stress distributions are symmetrical in the elastic contact solutions, whereas the peak values shift forward in the elasto-plastic solutions. These

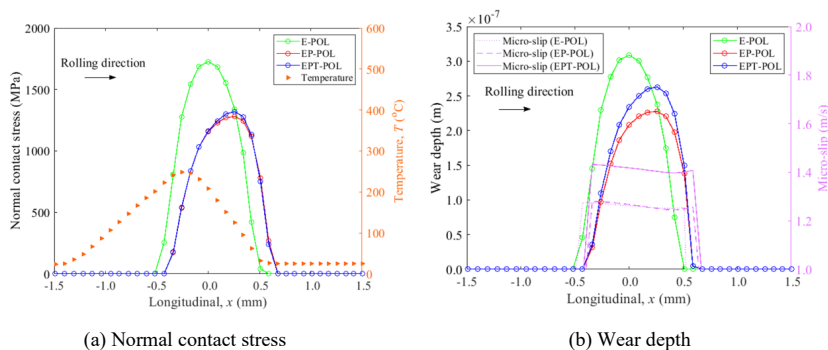


Figure 2.8: Simulated normal contact stresses and wear depths in a single contact patch (at instant t1) using different material models.

correspond well to the results reported in [30, 53]. The flash temperature simulated with model EPT-POL along the longitudinal center line of the running band ( $y = 0$  mm) is also displayed in Figure 2.8(a), as denoted by the triangular markers. The temperature increases from the leading area to the trailing area, which is consistent with the result simulated in [58, 59], because the cool material from the wheel and rail enters the contact patch from the leading area and is heated up gradually due to the friction within the contact patch. In line with the results reported in [37], the peak normal contact stress simulated with model EPT-POL is higher than the pure mechanical solution obtained with model EP-POL due to the thermal softening and thermal expansion/contraction stress. At the central area of the contact patch (the longitudinal position  $x$  ranges from 0 to 0.5 mm, as denoted in Figure 2.8), where the material yields due to high contact pressure and the flash temperature is around 150 °C, the normal contact stress obtained with model EPT-POL is higher, partly because the hardening modulus and the coefficient of thermal expansion increase with temperature in the range between 24 °C and 230 °C, as indicated in Table 2.3.

A similar trend can be seen in the wear depth results shown in Figure 2.8(b). According to Archard’s wear model given in equation (2.2), wear depth is proportional to the normal contact stress when the wear coefficient is determined. In addition, the sliding distance, or the micro-slip in this case indicated by the pink curves (dotted, dashed and solid) in Figure 2.8(b), contributes to the calculation of wear depth. We can see that the micro-slips of model E-POL and model EP-POL are close to each other, whereas the peak wear depth obtained with model E-POL is larger due to the higher normal contact stress. When the thermal softening is considered, the micro-slip is significantly increased (solid curve representing model EPT-POL). In combination with the increased normal contact stress shown in Figure 2.8(a), the wear depth calculated with model EPT-POL is significantly larger than that obtained with the model EP-POL. This indicated that the maximum wheel-rail normal contact stress and wear are overestimated without considering material plasticity (E-POL vs EP-POL/EPT-POL), whereas they can be underestimated without considering thermal effects (EP-POL vs EPT-POL).

The results calculated at a later time step (i.e., instant t2) as shown in Figure 2.9,

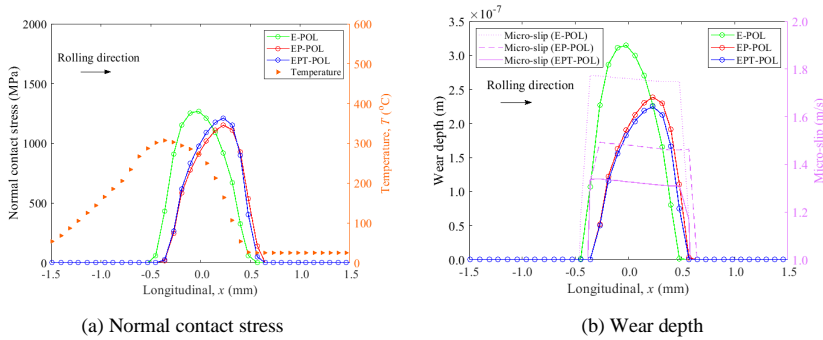


Figure 2.9: Simulated normal contact stresses and wear depths in a contact patch (at instant  $t_2$ ) using different material models.

present a more significant difference in the calculated normal contact stress obtained with model EP-POL and model EPT-POL. That is because the flash temperature calculated with model EPT-POL at this step is higher, about 200 °C at the center of the contact area. As to the results shown in Figure 2.9(b), despite the smaller normal contact stress, the wear depth obtained with model EP-POL is greater than that of model EPT-POL, due to the remarkably larger micro-slip (dashed curve) than that of model EPT-POL (solid curve). This suggests that, again, the maximum wheel-rail normal contact stress is underestimated without considering thermal effects (EP-POL vs. EPT-POL), whereas the wear depth can be either underestimated (Figure 2.8(b)) or overestimated (Figure 2.9(b)), depending also on the value of micro-slip.

#### 2.4.2.2 RESULTS ALONG THE WHEEL PROFILE

The analysis of results at one time step (Section 2.4.2.1) indicates the contact stress and wear depth may differ with time and slip ratio, the results along a section of wheel profile are thus analyzed in this section. In Figure 2.10, the maximum normal contact stress calculated with the three models at a series of time steps (with an interval of 0.06 ms) are plotted as curves with markers against the polygonal wheel profile plotted as a solid curve. The markers indicate the peak values of the wheel-rail normal contact stress calculated at the time steps of concern. In order to visualize the results of different material models at the same time step, particularly the results obtained with model EP-POL and model EPT-POL, a series of curves characterized by an alternating pattern of solid and hollow dots has been plotted. For instance, the blue hollow dot and the red hollow dot below it represent the results of the same time step at  $t_1$  and  $t_2$ . The lateral axis indicates the angular displacement that the wheel rolls over the rail, i.e.,  $\theta$  shown in Figure 2.3, which covers three wavelengths of the polygonal profile. The maximum normal stress curves with markers are not continuous at the troughs of the wheel profile, because the troughs of the wheel profile have no contact with the rail, and two-point contact occurs at locations close to the trough, as presented in Section 2.3.2.

Along the wheel rolling direction, the area after the trough and before the next profile crest is identified as the 'uphill' area, whereas the 'downhill' area is located after the crest and before the next trough. In general, the normal contact stress increases along the

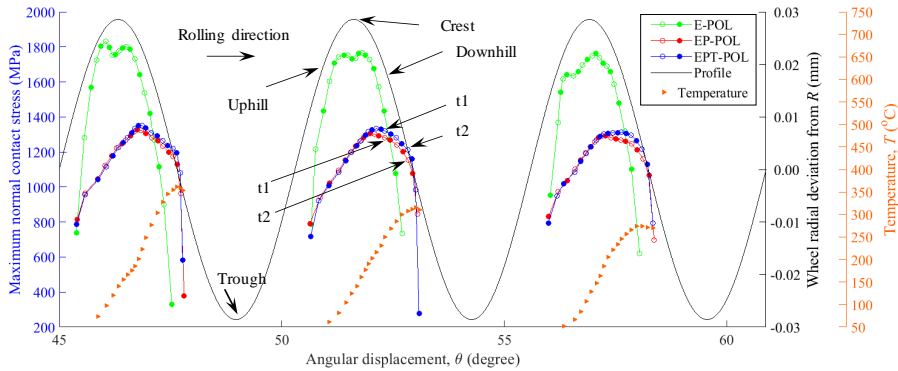


Figure 2.10: The maximum normal contact stress and temperature in each contact patch along the wheel profile.

‘uphill’ profile and decreases along the ‘downhill’ profile with the variation of the wheel-rail contact geometry. This finding can be supported by [39], where a similar trend of the wheel-rail contact stress along the corrugated rail was presented. The difference between the elastic and elasto-plastic solutions are as follows: at most of the locations, the normal contact stresses calculated with the elastic model (E-POL) are higher than those calculated with the elasto-plastic models (EP-POL and EPT-POL), which is consistent with the one-time-step results presented in Section 2.4.2.1; the normal contact stress peaks of all the time steps obtained with the elasto-plastic models (EP-POL and EPT-POL) are not at the crest of the polygonal profile, but a bit forward at the ‘downhill’ area compared to the results calculated with model E-POL. That is because the maximum magnitude of the contact stress is located in the leading part of the wheel-rail contact patch when plastic deformation occurs [30, 53].

To examine the effect of temperature, we may see again that the normal contact stress simulated with model EPT-POL is higher than the pure mechanical solution obtained with model EP-POL, also in line with the one-time-step results. Note that the difference occurs mainly at the ‘downhill’ area of the polygonal profile. This is because the temperature induced by wheel-rail contact at the ‘downhill’ area is higher. The simulated flash temperatures along the polygonal profile are also displayed in Figure 2.10, as denoted by the orange triangular markers. The triangular marker shows the peak flash temperature within the contact patch at the corresponding time step. It can be seen that the temperature presents a periodic pattern along with the polygonal profile: the temperature is low at the locations just after the wheel profile trough, because of the two-point contact; and it goes up gradually and reaches the highest amplitude before decreasing slightly near the next trough. At the ‘uphill’ areas, the friction power which generates contact heat is lower because of the lower friction force (contact stress). It thus causes lower flash temperature. The heat is then accumulated with the increase of friction force, which causes the increase in temperature. When the contact position is at the ‘downhill’ area approaching the trough, the contact stress, and thus friction power

(i.e., shear contact stress times micro-slip, which is not shown), decrease significantly (blue curve in Figure 2.10), causing a reduction in the rate of temperature increase and the drop of contact temperature near the trough. While the friction power levels at certain positions at both the 'downhill' and 'uphill' areas are comparable, the temperature at the 'downhill' region is higher. This phenomenon can be attributed to the fact that contact temperature is influenced by both friction power and thermal conduction from adjacent positions [60, 61]. The increased temperature of the wheel and rail at the 'downhill' area from the preceding time step rapidly propagates to the current materials in the contact patch, predominantly contributing to the higher contact temperature. The simulated peak contact temperature at the three waves of the analyzed polygonal profile are 362 °C, 315 °C, and 275 °C, respectively. These simulation results agree reasonably with the experimental results obtained from an ongoing measurement conducted in the V-Track using an infrared camera. A comprehensive analysis of the measured results and the testing methodology will be presented in a follow-up paper.

The wear depths along the wheel polygonal profile simulated with the three models are compared in Figure 2.11. The maximum wear depth calculated at the same time steps as those in Figure 2.10 are plotted with a series of curves featuring an alternating pattern of solid and hollow dots markers against the polygonal profile of the wheel and the flash temperature. By comparing Figure 2.10 to Figure 2.11, an obvious difference can be noticed: the wear depth results have two peaks in each wavelength of the wheel polygonal profile, no matter what material is used. The formation of the two peaks could be related to the longitudinal compression mode of the V-Track rail with modal frequency of 2300~2700 Hz [62]. The wheel profile at the locations of the two peaks of wear depth may experience heavier material loss, and be developed into new troughs, as presented in [63]. The wear depth peaks calculated with the elastic model (E-POL) are significantly larger than those calculated with the elasto-plastic models (EP-POL and EPT-POL) due mainly to the higher contact stress. In addition, the positions of the two peaks and the dip calculated with the elasto-plastic models shift forward to the 'downhill' area in comparison with the results of the elastic model. The dips between the two peaks of wear depth are located at the profile crest in the elastic simulation case, but a bit to the 'downhill' area in the elasto-plastic cases. This suggests that in the elastic contact case, the crests of the polygonal profile are less worn than the areas close by, and could thus be developed into higher-amplitude crests in the further cycles; and in the elasto-plastic case, the low-worn positions occur close to but after the crests of the polygonal profile.

By comparing the results of the two elasto-plastic models (EP-POL and EPT-POL), the thermal effect increases the 2nd peaks of wear depth, which are also located at the 'downhill' areas of the wheel polygonal profile where the simulated contact temperature is higher. The wear solutions presented in Figures 2.8(b) and 2.9(b) correspond to the results at  $t_1$  and  $t_2$  in the second wave. It can thus be concluded that the thermal effect increases the wear depths of the 2nd peak at the 'downhill' area along the wheel profile, but the wear depth can be overestimated after the 2nd peak at the 'downhill' area without considering the thermal effect. The wear depth increased by the thermal effect of the 1st peak is not significant because lower contact temperature does not significantly influence the material properties. The thermal effect should be considered when a high

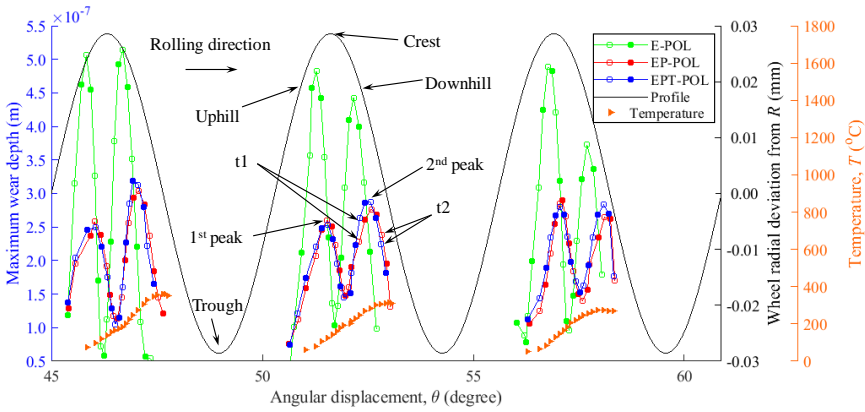


Figure 2.11: The maximum wear depth and temperature in each contact patch along the wheel profile.

contact temperature can be reached.

### 2.4.3. INFLUENCE OF THE INITIAL DEFECT AMPLITUDE

This section investigates the influence of initial defect amplitude on the development of polygonal wear. Three amplitudes of initial wheel polygonal profiles are applied to the elasto-plastic models (EP-POL and EPT-POL):  $A = 0.014\text{ mm}$ ,  $0.029\text{ mm}$ , and  $0.043\text{ mm}$  (1/7 scaled down from  $0.1\text{ mm}$ ,  $0.2\text{ mm}$ , and  $0.3\text{ mm}$ ), denoted by Profile-1, Profile-2 and Profile-3 in Figure 2.12, respectively. Figure 2.12 also displays the simulated wear depths along the prescribed initial profiles. In the legend, EP-POL-1 represents the wear depth simulated with model EP-POL with Profile-1, etc. We may see from Figure 2.12 that the simulated wear depth peaks increase with the initial wear amplitude, suggesting that the development of polygonisation is an accelerating progress: the larger the polygonal wear, the faster the development is [63]. In addition, the 1st peak and 2nd peak of the wear depth move closer to the crest of the profile with the increase of initial wear amplitude, which indicates that locations at these peaks suffer from large-amplitude wear and result in the development of new polygonal profile. Furthermore, for all the simulation cases, the wear depth simulated with model EP-POL is smaller than that of model EPT-POL at the 2nd peak along the wheel profile where the wheel-rail contact-induced temperature is high.

## 2.5. CONCLUSIONS

To investigate the development of wheel polygonal wear, this study simulates impact contact between the polygonal wheel and rail using an FE thermomechanical analysis. The elastic contact solutions with a round and a polygonal wheel profile are verified against the CONTACT program. The contact stress, temperature, and development of wheel polygonal wear are then investigated. Simulations with different materials (elas-

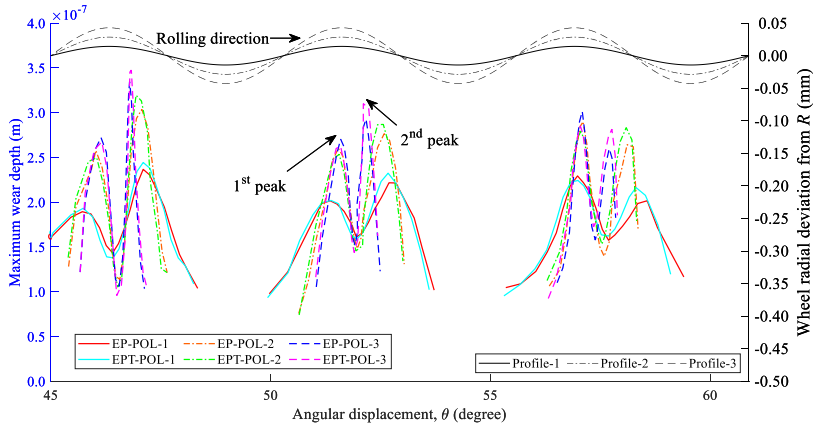


Figure 2.12: Influence of the initial amplitudes on wear depth along the wheel profile.

tic, elasto-plastic and elasto-plastic-thermo, i.e., with thermal softening) and initial amplitudes are conducted to examine the influences of plasticity, thermal effect, and initial defects on the wheel-rail contact stress distributions and consequent wear development. The following conclusions can be drawn from this study:

- The normal contact stress simulated with thermomechanical model is higher than the pure mechanical solution involving plasticity due to the thermal softening and thermal expansion/contraction stress, especially at locations after the crest of polygonal profile, where the contact temperature is high. The wheel-rail impact contact stress can thus be underestimated without considering thermal effects.
- Within a contact patch, the contact temperature increases from the leading area to the trailing area, because cool materials enter the contact patch from the leading area and are then heated up during frictional rolling.
- The contact temperature presents a periodic pattern along with the polygonal profile: the temperature is low at the locations just after the wheel profile trough and it goes up gradually and reaches the highest amplitude before decreasing slightly near the next trough. The simulated peak contact temperature at the three waves along the polygonal profile are 362 °C, 315 °C, and 275 °C, respectively.
- The material model influences wear depth calculation. The peaks of wear depth can be significantly overestimated when elastic model is used. The consideration of thermal effect increases the peaks of wear depth, especially when the contact temperature is high.
- The simulated wear depth peaks increase with the initial polygonal wear amplitude, suggesting that with the increase of wear amplitudes, the development of polygonization is accelerated.



# BIBLIOGRAPHY

- [1] G. Tao et al. “Experimental investigation into the mechanism of the polygonal wear of electric locomotive wheels”. In: *Vehicle System Dynamics* 56 (2018), pp. 883–899. DOI: [10.1080/00423114.2017.1399210](https://doi.org/10.1080/00423114.2017.1399210).
- [2] G. Tao et al. “An investigation into the mechanism of the out-of-round wheels of metro train and its mitigation measures”. In: *Vehicle System Dynamics* 57 (2018), pp. 1–16. DOI: [10.1080/00423114.2018.1445269](https://doi.org/10.1080/00423114.2018.1445269).
- [3] Y. Wu et al. “Experimental analysis of the mechanism of high-order polygonal wear of wheels of a high-speed train”. In: *Journal of Zhejiang University-Science A* 18 (2017), pp. 579–592. DOI: [10.1631/jzus.A1600741](https://doi.org/10.1631/jzus.A1600741).
- [4] D.W. Barke and W.K. Chiu. “A review of the effects of out-of-round wheels on track and vehicle components”. In: *Proceedings of the Institution of Mechanical Engineers, Part F: Journal of Rail and Rapid Transit* 219 (2005), pp. 151–175. DOI: [10.1243/095440905x8853](https://doi.org/10.1243/095440905x8853).
- [5] K. Knothe and S. Grassie. “Workshop on rail corrugations and out-of-round wheels”. In: *Journal of Sound and Vibration* 227 (1999), pp. 895–897. DOI: [10.1006/jsvi.1999.2053](https://doi.org/10.1006/jsvi.1999.2053).
- [6] W. Rode, D. Müller, and J. Villman. “Results of DB AG investigations ‘out-of-round wheels’”. In: *Proceedings corrugation symposium–extended abstracts, IFV Bahntechnik* (1997).
- [7] D. Cui et al. “Effect of the turning characteristics of underfloor wheel lathes on the evolution of wheel polygonisation”. In: *Proceedings of the Institution of Mechanical Engineers, Part F: Journal of Rail and Rapid Transit* 233 (2018), pp. 479–488. DOI: [10.1177/0954409718795760](https://doi.org/10.1177/0954409718795760).
- [8] J.C.O. Nielsen and A. Johansson. “Out-of-round railway wheels—a literature survey”. In: *Proceedings of the Institution of Mechanical Engineers, Part F: Journal of Rail and Rapid Transit* 214 (2005), pp. 79–91. DOI: [10.1243/0954409001531351](https://doi.org/10.1243/0954409001531351).
- [9] P. Meinke and S. Meinke. “Vibration, Polygonalization of wheel treads caused by static and dynamic imbalances”. In: *Journal of Sound and Vibration* 227 (1999), pp. 979–986. DOI: [10.1006/jsvi.1999.2590](https://doi.org/10.1006/jsvi.1999.2590).
- [10] X. Jin et al. “An investigation into the mechanism of the polygonal wear of metro train wheels and its effect on the dynamic behaviour of a wheel/rail system”. In: *Vehicle System Dynamics* 50 (2012), pp. 1817–1834. DOI: [10.1080/00423114.2012.695022](https://doi.org/10.1080/00423114.2012.695022).
- [11] G. Tao et al. “An investigation into the mechanism of high-order polygonal wear of metro train wheels and its mitigation measures”. In: *Vehicle System Dynamics* 59 (2020), pp. 1557–1572. DOI: [10.1080/00423114.2020.1770810](https://doi.org/10.1080/00423114.2020.1770810).

- [12] W. Ma, R. Song, and S. Luo. “Study on the mechanism of the formation of polygon-shaped wheels on subway vehicles”. In: *Proceedings of the Institution of Mechanical Engineers, Part F: Journal of Rail and Rapid Transit* 230 (2014), pp. 129–137. DOI: [10.1177/0954409714529269](https://doi.org/10.1177/0954409714529269).
- [13] W. Cai et al. “Experimental and numerical analysis of the polygonal wear of high-speed trains”. In: *Wear* 440 (2019). DOI: [10.1016/j.wear.2019.203079](https://doi.org/10.1016/j.wear.2019.203079).
- [14] J. Kalousek and K. Johnson. “An investigation of short pitch wheel and rail corrugations on the Vancouver mass transit system”. In: *Proceedings of the Institution of Mechanical Engineers, Part F: Journal of Rail and Rapid Transit* 206 (1992), pp. 127–135. DOI: [10.1243/PIME\\_PROC\\_1992\\_206\\_226\\_02](https://doi.org/10.1243/PIME_PROC_1992_206_226_02).
- [15] A. Johansson and C. Andersson. “Out-of-round railway wheels—a study of wheel polygonalization through simulation of three-dimensional wheel–rail interaction and wear”. In: *Vehicle System Dynamics* 43 (2006), pp. 539–559. DOI: [10.1080/00423110500184649](https://doi.org/10.1080/00423110500184649).
- [16] B.W. Wu et al. “Effect of the unstable vibration of the disc brake system of high-speed trains on wheel polygonalization”. In: *Proceedings of the Institution of Mechanical Engineers, Part F: Journal of Rail and Rapid Transit* 234 (2019), pp. 80–95. DOI: [10.1177/0954409719833787](https://doi.org/10.1177/0954409719833787).
- [17] T. Vernersson and R. Lundén. “Temperatures at railway tread braking. Part 3: wheel and block temperatures and the influence of rail chill”. In: *Proceedings of the Institution of Mechanical Engineers, Part F: Journal of Rail Rapid Transit* 221 (2007), pp. 443–454. DOI: [10.1243/09544097JRRT91](https://doi.org/10.1243/09544097JRRT91).
- [18] T. Vernersson. “Temperatures at railway tread braking. Part 1: modelling”. In: *Proceedings of the Institution of Mechanical Engineers, Part F: Journal of Rail Rapid Transit* 221 (2007), pp. 167–182. DOI: [10.1243/09544097JRRT57](https://doi.org/10.1243/09544097JRRT57).
- [19] G. Tao et al. “Polygonisation of railway wheels: a critical review”. In: *Railway Engineering Science* 28 (2020), pp. 317–345. DOI: [10.1007/s40534-020-00222-x](https://doi.org/10.1007/s40534-020-00222-x).
- [20] B. Morys. “Enlargement of out-of-round wheel profiles on high speed trains”. In: *Journal of Sound and Vibration* 227 (1999), pp. 965–978. DOI: [10.1006/jsvi.1999.2055](https://doi.org/10.1006/jsvi.1999.2055).
- [21] J.J. Kalker. “A fast algorithm for the simplified theory of rolling contact”. In: *Vehicle System Dynamics* 11 (2007), pp. 1–13. DOI: [10.1080/00423118208968684](https://doi.org/10.1080/00423118208968684).
- [22] M. Meywerk. “Polygonalization of railway wheels”. In: *Archive of Applied Mechanics* 69 (1999), pp. 105–120. DOI: [10.1007/s004190050208](https://doi.org/10.1007/s004190050208).
- [23] J.J. Kalker. “Survey of wheel–rail rolling contact theory”. In: *Vehicle System Dynamics* 8 (2007), pp. 317–358. DOI: [10.1080/00423117908968610](https://doi.org/10.1080/00423117908968610).
- [24] C. Andersson and A. Johansson. “Prediction of rail corrugation generated by three-dimensional wheel–rail interaction”. In: *Wear* 257 (2004), pp. 423–434. DOI: [10.1016/j.wear.2004.01.006](https://doi.org/10.1016/j.wear.2004.01.006).
- [25] Z. Shen, J. Hedrick, and J. Elkins. “A comparison of alternative creep force models for rail vehicle dynamic analysis”. In: *Vehicle System Dynamics* 12 (2007), pp. 79–83. DOI: [10.1080/00423118308968725](https://doi.org/10.1080/00423118308968725).

- [26] N. Burgelman et al. "Influence of wheel–rail contact modelling on vehicle dynamic simulation". In: *Vehicle System Dynamics* 53 (2015), pp. 1190–1203. DOI: [10.1080/00423114.2015.1039550](https://doi.org/10.1080/00423114.2015.1039550).
- [27] M. Sh. Sichani, R. Enblom, and M. Berg. "A novel method to model wheel–rail normal contact in vehicle dynamics simulation". In: *Vehicle System Dynamics* 52 (2014), pp. 1752–1764. DOI: [10.1080/00423114.2014.961932](https://doi.org/10.1080/00423114.2014.961932).
- [28] Y. Sun, W. Zhai, and Y. Guo. "A robust non-Hertzian contact method for wheel–rail normal contact analysis". In: *Vehicle System Dynamics* 56 (2018), pp. 1899–1921. DOI: [10.1080/00423114.2018.1439587](https://doi.org/10.1080/00423114.2018.1439587).
- [29] M. Sh. Sichani, R. Enblom, and M. Berg. "An alternative to FASTSIM for tangential solution of the wheel–rail contact". In: *Vehicle System Dynamics* 2016 (2016), pp. 748–764. DOI: [10.1080/00423114.2016.1156135](https://doi.org/10.1080/00423114.2016.1156135).
- [30] X. Zhao and Z. Li. "A three-dimensional finite element solution of frictional wheel–rail rolling contact in elasto-plasticity". In: *Proceedings of the Institution of Mechanical Engineers, Part J: Journal of Engineering Tribology* 229 (2015), pp. 86–100. DOI: [10.1177/1350650114543717](https://doi.org/10.1177/1350650114543717).
- [31] K. Liu and L. Jing. "A finite element analysis-based study on the dynamic wheel–rail contact behaviour caused by wheel polygonization". In: *Proceedings of the Institution of Mechanical Engineers, Part F: Journal of Rail Rapid Transit* 234 (2020), pp. 1285–1298. DOI: [10.1177/0954409719891549](https://doi.org/10.1177/0954409719891549).
- [32] L. Han, L. Jing, and K. Liu. "A dynamic simulation of the wheel–rail impact caused by a wheel flat using a 3-D rolling contact model". In: *Journal of Modern Transportation* 25 (2017), pp. 124–131. DOI: [10.1007/s40534-017-0131-0](https://doi.org/10.1007/s40534-017-0131-0).
- [33] R. Lewis and U. Olofsson. "Mapping rail wear regimes and transitions". In: *Wear* 257 (2004), pp. 721–729. DOI: [10.1016/j.wear.2004.03.019](https://doi.org/10.1016/j.wear.2004.03.019).
- [34] A.M.S. Asih, K. Ding, and A. Kapoor. "Modelling rail wear transition and mechanism due to frictional heating". In: *Wear* 284–285 (2012), pp. 82–90. DOI: [10.1016/j.wear.2012.02.017](https://doi.org/10.1016/j.wear.2012.02.017).
- [35] L. Wu et al. "Thermo-elastic–plastic finite element analysis of wheel/rail sliding contact". In: *Wear* 271 (2011), pp. 437–443. DOI: [10.1016/j.wear.2010.10.034](https://doi.org/10.1016/j.wear.2010.10.034).
- [36] K. Vo et al. "The influence of high temperature due to high adhesion condition on rail damage". In: *Wear* 330 (2015), pp. 571–580. DOI: [10.1016/j.wear.2015.01.059](https://doi.org/10.1016/j.wear.2015.01.059).
- [37] M. Naeimi et al. "Thermomechanical analysis of the wheel-rail contact using a coupled modelling procedure". In: *Tribology International* 117 (2018), pp. 250–260. DOI: [10.1016/j.triboint.2017.09.010](https://doi.org/10.1016/j.triboint.2017.09.010).
- [38] Q. Lian et al. "Thermo-mechanical coupled finite element analysis of rolling contact fatigue and wear properties of a rail steel under different slip ratios". In: *Tribology International* 141 (2020). DOI: [10.1016/j.triboint.2019.105943](https://doi.org/10.1016/j.triboint.2019.105943).
- [39] Y.C. Chen and S.Y. Lee. "Elastic-plastic wheel-rail thermal contact on corrugated rails during wheel braking". In: *Journal of Tribology* 131 (2009). DOI: [10.1115/1.2991163](https://doi.org/10.1115/1.2991163).

- [40] J. Archard and W. Hirst. “The wear of metals under unlubricated conditions”. In: *Proceedings of the Royal Society of London. Series A. Mathematical Physical Sciences* 236 (1956), pp. 397–410. DOI: [10.1098/rspa.1956.0144](https://doi.org/10.1098/rspa.1956.0144).
- [41] M. Naeimi et al. “Development of a new downscale setup for wheel-rail contact experiments under impact loading conditions”. In: *Experimental Techniques* 42 (2018), pp. 1–17. DOI: [10.1007/s40799-017-0216-z](https://doi.org/10.1007/s40799-017-0216-z).
- [42] P. Zhang, J. Moraal, and Z. Li. “Design, calibration and validation of a wheel-rail contact force measurement system in V-Track”. In: *Measurement* 175 (2021). DOI: [10.1016/j.measurement.2021.109105](https://doi.org/10.1016/j.measurement.2021.109105).
- [43] J.J. Kalker. *Three-dimensional elastic bodies in rolling contact*. Vol. 2. Springer Science Business Media, 2013.
- [44] Z. Yang et al. “An experimental study on the effects of friction modifiers on wheel–rail dynamic interactions with various angles of attack”. In: *Railway Engineering Science* 30 (2022), pp. 360–382. DOI: [10.1007/s40534-022-00285-y](https://doi.org/10.1007/s40534-022-00285-y).
- [45] P. Zhang and Z. Li. “Experimental study on the development mechanism of short pitch corrugation using a downscale V-Track test rig”. In: *Tribology International* 180 (2023). DOI: [10.1016/j.triboint.2023.108293](https://doi.org/10.1016/j.triboint.2023.108293).
- [46] C. Shen, R. Dollevoet, and Z. Li. “Fast and robust identification of railway track stiffness from simple field measurement”. In: *Mechanical Systems and Signal Processing* 152 (2021). DOI: [10.1016/j.ymsp.2020.107431](https://doi.org/10.1016/j.ymsp.2020.107431).
- [47] M. Molodova. “Detection of early squats by axle box acceleration”. PhD thesis. Delft University of Technology, The Netherlands, 2013.
- [48] X. Zhao and Z. Li. “The solution of frictional wheel–rail rolling contact with a 3D transient finite element model: Validation and error analysis”. In: *Wear* 271 (2011), pp. 444–452. DOI: [10.1016/j.wear.2010.10.007](https://doi.org/10.1016/j.wear.2010.10.007).
- [49] Z. Yang and Z. Li. “Numerical modeling of wheel-rail squeal-exciting contact”. In: *International Journal of Mechanical Sciences* 153–154 (2019), pp. 490–499. DOI: [10.1016/j.ijmecsci.2019.02.012](https://doi.org/10.1016/j.ijmecsci.2019.02.012).
- [50] A. Jaschinski et al. “The application of roller rigs to railway vehicle dynamics”. In: *Vehicle System Dynamics* 31 (1999), pp. 345–392. DOI: [10.1076/vesd.31.5.345.8360](https://doi.org/10.1076/vesd.31.5.345.8360).
- [51] T. Jendel. “Prediction of wheel profile wear—comparisons with field measurements”. In: *Wear* 253 (2002), pp. 89–99. DOI: [10.1016/S0043-1648\(02\)00087-X](https://doi.org/10.1016/S0043-1648(02)00087-X).
- [52] J. Brouzoulis et al. “Prediction of wear and plastic flow in rails—Test rig results, model calibration and numerical prediction”. In: *Wear* 271 (2011), pp. 92–99. DOI: [10.1016/j.wear.2010.10.021](https://doi.org/10.1016/j.wear.2010.10.021).
- [53] Z. Yang et al. “Numerical study of wheel-rail impact contact solutions at an insulated rail joint”. In: *International Journal of Mechanical Sciences* 138 (2018), pp. 310–322. DOI: [10.1016/j.ijmecsci.2018.02.025](https://doi.org/10.1016/j.ijmecsci.2018.02.025).
- [54] Z. Yang, X. Deng, and Z. Li. “Numerical modeling of dynamic frictional rolling contact with an explicit finite element method”. In: *Tribology International* 129 (2019), pp. 214–231. DOI: [10.1016/j.triboint.2018.08.028](https://doi.org/10.1016/j.triboint.2018.08.028).

- [55] Z. Wei et al. “3D FE modelling and validation of frictional contact with partial slip in compression–shift–rolling evolution”. In: *International Journal of Rail Transportation* 4 (2015), pp. 20–36. DOI: [10.1080/23248378.2015.1094753](https://doi.org/10.1080/23248378.2015.1094753).
- [56] M.P. Do Carmo. *Differential geometry of curves and surfaces: revised and updated second edition*. Courier Dover Publications, 2016.
- [57] S. Li et al. “An integrated 3D dynamic FE vehicle-track model in elasto-plasticity to investigate short pitch corrugation under cyclic wheel loads”. In: *Structures* 53 (2023), pp. 1000–1011. DOI: [10.1016/j.istruc.2023.05.001](https://doi.org/10.1016/j.istruc.2023.05.001).
- [58] K. Knothe and S. Liebelt. “Determination of temperatures for sliding contact with applications for wheel-rail systems”. In: *Wear* 189 (1995), pp. 91–99. DOI: [10.1016/0043-1648\(95\)06666-7](https://doi.org/10.1016/0043-1648(95)06666-7).
- [59] L.J. Oestriinger and C. Proppe. “On the transient thermomechanical contact simulation for two sliding bodies with rough surfaces and dry friction”. In: *Tribology International* 170 (2022). DOI: [10.1016/j.triboint.2021.107425](https://doi.org/10.1016/j.triboint.2021.107425).
- [60] O.H. John. *LS-DYNA theory manual*. Livermore Software Technology Corporation, California, 2006.
- [61] O.M. Necati. *Heat conduction*. John Wiley Sons, Inc, 1993.
- [62] P. Zhang et al. “Comprehensive validation of three-dimensional finite element modelling of wheel-rail high-frequency interaction via the V-Track test rig”. In: *Vehicle System Dynamics* (2024). DOI: [10.1080/00423114.2024.2304626](https://doi.org/10.1080/00423114.2024.2304626).
- [63] B. Fu, S. Bruni, and S. Luo. “Study on wheel polygonization of a metro vehicle based on polygonal wear simulation”. In: *Wear* 438–439 (2019). DOI: [10.1016/j.wear.2019.203071](https://doi.org/10.1016/j.wear.2019.203071).



# 3

## INFRARED TEMPERATURE MEASUREMENT OF WHEEL-RAIL FRICTIONAL ROLLING CONTACT UP TO HIGH SLIP RATIOS

*Thermal loading resulting from wheel-rail frictional heat accelerates wear, plastic deformation, and fatigue, especially under high contact temperatures. Accurate measurements of wheel-rail contact temperature are thus crucial for understanding and preventing thermal damage. Existing studies have commonly assessed wheel-rail contact temperatures experimentally in a relatively low range (below 200 °C), while higher temperatures that cause severe thermal damage have been rarely measured. To fill this gap, this work develops a measurement system in the V-Track test rig, which can reproduce and capture wheel-rail frictional rolling contact temperatures up to 1200 °C. In this measurement system, a high-precision infrared thermal camera was mounted on a moving wheel assembly to continuously measure the wheel-rail contact temperature in the running scenario. A wheel braking process was simulated by applying a controllable negative wheel torque, which generated slip ratios from 2% to 99%. To ensure the accuracy of the temperature measurement, an emissivity calibration of the V-Track rail samples was conducted. The calibrated rail emissivity values are 0.83 at 600 °C and 0.43 at 950 °C. The V-Track test results revealed that the wheel-rail contact temperature generally rose with slip ratios and reached up to 1000 °C with a slip ratio of 99%. When the slip ratio reached 40%, a “wheel flat” was formed with the wheel-rail contact temperature around 624 °C, followed by a rapid drop as the “wheel flat” exited the contact area. This research demonstrates the reliability of the developed system in the high-temperature measurement induced by wheel-rail contact and may serve as a reference for calibrating and validating thermal contact and damage numerical models.*

---

This chapter has been submitted for international journal publication.

### 3.1. INTRODUCTION

**F**RICTION between the wheel and rail plays an important role in train traction, braking, and curve negotiation. However, the frictional heat generated at the wheel-rail interface and the resultant thermal stresses are undesirable, particularly at high slip ratios [1]. Thermal loading is detrimental to the wheel and rail materials because it greatly expedites wear, causes plastic deformation, and causes fatigue [2]. Some typical thermal damage examples are shown in Figure 3.1: rail burn (Figure 3.1(a)), a wheel flat (Figure 3.1(b)), and thermal cracks at the wheel tread and rail top surface (Figures 3.1(c) and (d)). When subjected to high contact temperatures (e.g., 200 °C ~ 250 °C [3] and exceeding 350 °C [4]) with high slip ratios, rail material can get easily worn due to thermal softening [3, 4]. Rail burn and wheel flats, accompanied by significant plastic deformation, are caused by wheel-rail sliding under extremely high temperatures [5]. Moreover, thermal loading may accelerate wheel and rail fatigue by altering material properties, e.g., decreasing the elastic and shakedown limits and making the steel susceptible to progressive plastic deformation and cracks [6]. Additionally, contact temperatures around 720 °C and higher [7, 8] may induce microstructural transformations in the material, leading to the thermally-induced white etching layer (WEL) [9]. The inclusion of brittle martensite in the WEL then makes the material more prone to cracking. The thermal damage at the wheel-rail interface greatly increases maintenance costs and impacts the safety of train operations. To better understand and prevent thermal damage, it is crucial to accurately assess the thermal effects at the wheel-rail interface. For this purpose, a reliable measurement of wheel-rail contact temperature is a prerequisite.

Both contact and non-contact methods have been developed to measure temperatures at the contact interfaces. The contact methods commonly utilize thermocouples, while the non-contact methods generally employ infrared thermal cameras [13]. Different test setups using thermocouples have been designed to measure contact temperatures. For instance, the thermocouples can be embedded into pre-drilled holes in a pin-on-disc setup to identify temperature fields and heat fluxes at the contact surface [14]. It should be noted that the thermocouple was located 1 mm below the contact surface in this setup and thus captured temperatures lower than those on the surface. Additionally, drilling holes into contact objects may alter their contact stiffness and stress distributions, leading to unrealistic contact conditions. Instead of being embedded, thermocouples can also be attached to the side faces of contact bodies close to the contact patch [15]. Such an implementation is, however, not suitable for real-life applications with complex contact geometries. In addition to the thermocouples placed near the contact patch, the thin-film thermocouples have been placed directly on the contact surfaces to measure the contact temperature. The thin-film thermocouples were designed based on a pin-on-flat wear test rig to measure the surface temperature distribution under a normal load of 100 N and a temperature below 150 °C [16]. The thin-film thermocouples need to be firmly attached to the contact surfaces for accurate measurements [17, 18]. However, wheel-rail contact introduces high contact pressure and shear stress, potentially leading to wear, damage, or detachment of thin-film thermocouples, and thus affecting measurement results. Besides, it should be noted that the discrete distribution of thermocouples provides temperature information only at specific points; therefore, the thermocouples cannot be handily used to capture continuous tempera-

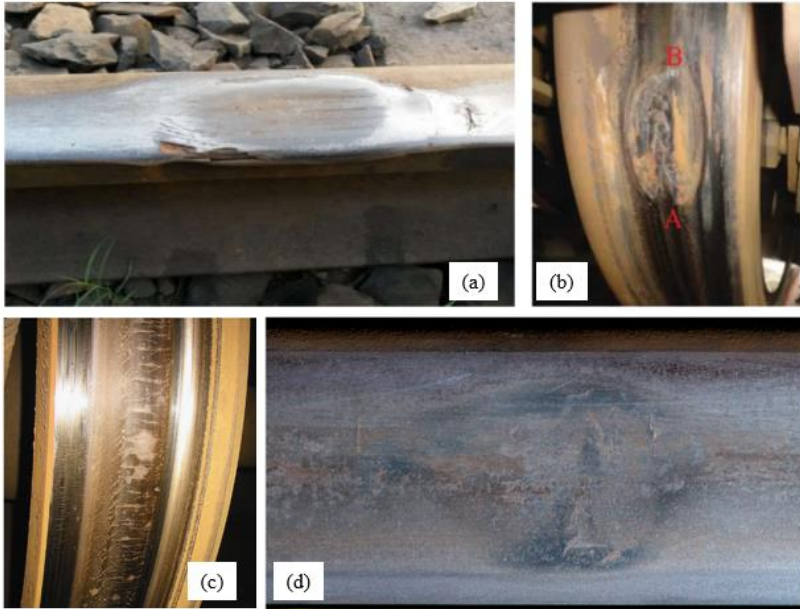


Figure 3.1: Typical wheel and rail damage caused by thermal loading. (a) Rail burn [10]; (b) wheel flat [11]; (c) thermal cracks on the wheel tread [12]; (d) thermal cracks in a squat [8].

ture distributions, especially in the contact areas with large temperature gradients.

As to the non-contact methods, infrared thermal cameras have been employed to monitor the temperature field close to the wheel-rail interface. In [19], an infrared thermal camera was mounted on a vehicle body behind a trailing wheel to measure wheel-rail contact positions as the train navigated switches and crossings. The technique in [19] was improved in [20] by mounting a thermal camera on the bogie, to avoid correcting the viewing angle caused by the yaw angle difference between the vehicle body and bogie. Digital image processing technology was then applied to process the camera-recorded thermal images to identify the positions of wheel-rail contact points. In [21], a thermal camera was mounted on the tram to monitor wheel and rail contact conditions by analyzing the thermal images. It is worth noting that the studies in [19–21] focused mainly on identifying wheel-rail contact points based on thermal images, with little attention paid to the absolute levels of contact temperature. In [3, 22], a thermal camera with a range from  $-20\text{ }^{\circ}\text{C}$  to  $350\text{ }^{\circ}\text{C}$  was used in a twin-disc test rig in the lab to measure contact temperatures with slip ratios from 0.2% to 5%. Although the twin-disc experiments allowed precise control of contact conditions, such as the slip ratio, they had limitations in simulating the real-life wheel-rail dynamic contact [22]. Besides, the maximum contact temperature measured in [22] is below  $200\text{ }^{\circ}\text{C}$ . Therefore, investigations of wheel-rail dynamic contact with higher contact temperatures (e.g., higher than  $498\text{ }^{\circ}\text{C}$  [23]) are still needed to provide insights into the development of thermal damage.

In this study, an innovative measurement system was developed in the TU-Delft V-

Track test rig [24, 25] to reproduce and capture high contact temperatures up to 1200 °C at the wheel-rail interface. An infrared thermal camera was mounted on a moving wheel assembly, enabling a continuous measurement of contact temperature. Compared to the previous studies using thermal cameras [3, 19–22], a more sensitive and precise camera was used in this study to capture the transient thermal phenomena that occur within short time frames, e.g., the cooling process. A braking process was simulated in the V-Track with slip ratios from about 2% to 99%. An emissivity calibration of the V-Track rail samples was conducted to ensure the accuracy of the temperature measured with the infrared thermal camera. The structure of this paper is organized as follows. Section 3.2 details the experimental methodology of the wheel-rail contact temperature in the V-Track test rig. Section 3.3 outlines the process of the rail emissivity calibration. Section 3.4 presents and analyzes the contact temperature measurement results in the V-Track. Finally, Section 3.5 summarizes the main conclusions of the study.

## 3.2. EXPERIMENTAL METHODOLOGY

In this section, we introduce the structure of the V-Track test rig, the developed temperature measurement system using an infrared thermal camera, and the test procedure.

### 3.2.1. V-TRACK TEST RIG

The downscale V-Track test rig has been developed to simulate and investigate real-life wheel-rail frictional rolling contact and related problems [26, 27]. As shown in Figure 3.2(a), the V-Track test rig consists of a ring track system and two wheel assemblies, W1 and W3, which are connected to a driving steel frame centered on the ring track. W3 is positioned on the opposite side of the driving steel frame relative to W1. Propelled by a motor through the driving steel frame, the wheel assemblies can run along the ring track at a speed of up to 40 km/h. Another motor provides a negative/positive torque to the wheels through torsional shafts to simulate train braking/traction.

A close-up view of the V-Track wheel assembly and track system is illustrated in Figure 3.2(b). The cylindrical wheels have a radius of 65 mm, about 1/7 scale to a passenger train wheel. The wheels are preloaded on the ring track by two suspension springs. The ring track has a radius of 2 m, consisting of five rail sections with four rail grades (i.e., B360, R370, R350 HT, and R260) connected by the joints J1 ~ J5, as shown in Figure 3.2(c). The rails have the same profile, with a head curvature radius of 60 mm. The rails are fixed to 100 evenly-distributed sleepers through fastenings, and the sleepers are supported by the “ballast” and the subgrade, which are represented by the rubber pads and plywood layers, respectively. To ensure identical wheel/rail material and thermo-mechanical behaviors to the field, the rails and wheels used in the V-Track were cut from actual rail heads and wheel rims. The coefficient of friction between the wheel and the rail was about 0.45. More parameters of the V-Track test rig can be found in [28].

The wheel-rail contact forces in three directions can be recorded in the V-Track using dynamometers [25], with a sampling rate of 16.67 kHz. Two separate encoders with a data acquisition rate of 16.67 kHz were installed in the test rig to obtain the angular velocities of the driving steel frame and the wheel axle. The measured slip ratio can be calculated by equation (3.1):

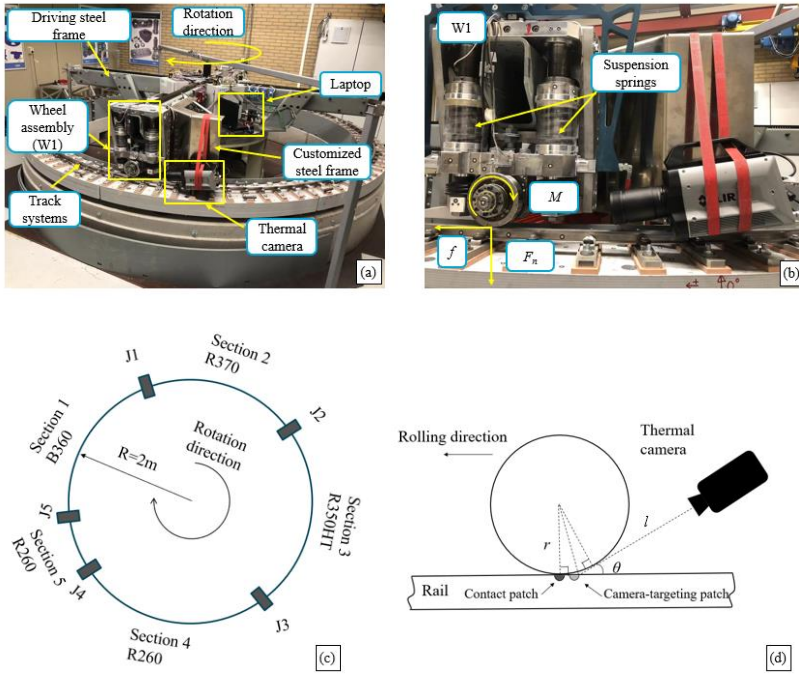


Figure 3.2: The experiment setup for contact temperature measurement in the V-Track test rig. (a) an overview of the V-Track equipped with an infrared thermal camera; (b) a close-up view of the V-Track wheel assembly, track system, and the installation of the infrared thermal camera; (c) a schematic of the ring track system; (d) a schematic of the setup for contact temperature measurement.

$$S = \frac{V_p - \omega r}{V_p} = \frac{\omega_0 - \omega}{\omega_0} \times 100\% \quad (3.1)$$

where  $S$  denotes the slip ratio,  $\omega_0$  is the angular velocity of the wheel under a free rolling contact condition (i.e., when the wheel translation velocity equals the wheel circumferential velocity),  $V_p$  is the wheel translation velocity corresponding to  $\omega_0$ ,  $\omega$  is the wheel angular velocity measured under different slip conditions, and  $r$  is the wheel radius.

### 3.2.2. TEMPERATURE MEASUREMENT SYSTEM

A measurement system was implemented in the V-Track to capture wheel-rail contact temperature, which consisted of an infrared thermal camera, a laptop for remote control, and a customized steel (mounting) frame, as shown in Figure 3.2(a) and Figure 3.2(b). A high-precision FLIR X6900sc infrared thermal camera [29] was used in this study, with its specifications detailed in Table 3.1. The camera incorporates multiple temperature measurement ranges, namely  $10^\circ\text{C} \sim 90^\circ\text{C}$ ,  $80^\circ\text{C} \sim 120^\circ\text{C}$ ,  $250^\circ\text{C} \sim 670^\circ\text{C}$ , and  $600^\circ\text{C} \sim 1200^\circ\text{C}$ . With a spectral range of  $3.0\ \mu\text{m} \sim 5.0\ \mu\text{m}$ , this camera is most sensitive to the temperature range of  $300^\circ\text{C} \sim 700^\circ\text{C}$ , where the highest image quality and temperature

resolution can be provided [30]. This camera can capture images with a high resolution of  $640 \times 512$  pixels at a rate of 1000 frames per second (i.e., 1000 Hz), suitable for capturing transient contact temperature during wheel-rail dynamic interactions. For higher temperature measurement ranges (i.e.,  $250^\circ\text{C} \sim 1200^\circ\text{C}$ ), the camera was installed with a four-position motorized filter to isolate specific wavelengths of light and to modulate the quantity of incoming radiation to the camera sensor [31]. Limited to the storage capacity of the camera, it captured 20 s of data at a sampling frequency of 1000 Hz per test. Each data file thus contains 20,000 thermal images allowing for individual analysis of each frame.

Table 3.1: Specifications of the FLIR X6900sc camera [29]

Parameter	Value
Resolution	$640 \times 512$ pixels
Spectral range	$3.0 \sim 5.0 \mu\text{m}$
Temperature range	$10 \sim 90^\circ\text{C}$ , $80 \sim 120^\circ\text{C}$ , $250 \sim 670^\circ\text{C}$ , $600 \sim 1200^\circ\text{C}$
Accuracy	$\pm 2^\circ\text{C}$ or $\pm 2\%$ of reading
Lens	$3 \sim 5 \mu\text{m}$ : 25 mm
Focus	Manual
Filtering	Filter wheel, standard 1-inch filters
Frame rate (Full Window) programmable	0.0015 Hz to 1004 Hz
On-camera image storage	RAM (volatile): 16 GB, full frame

To continuously monitor the wheel-rail contact temperature, the infrared thermal camera was mounted onto a customized steel frame on the trailing side of W1, as shown in Figures 3.2(a) and (b). To position the camera as close as possible to the wheel-rail contact point and avoid a collision with the rail, a small projection angle  $\theta = 11^\circ$  was selected, as schematically shown in Figure 3.2(d). This angle represented the angle between the projection line of the camera and the horizontal axis. The distance between the center of the camera-targeting patch and the camera lens (denoted as  $l$  in Figure 3.2(d)) was 0.29 m. Being screwed onto the customized steel mounting frame, with the red belts providing extra protection, the camera maintained the same travel speed as the wheel assembly and focused specifically on the wheel-rail contact region. This measurement setup allowed for capturing the rail surface temperature field just 4.5 mm behind the trailing edge of the contact area. The laptop was placed on the driving steel frame and was remotely controlled for data acquisition.

### 3.2.3. TEST CONDITIONS AND PROCEDURE

This study measured the wheel-rail contact temperature during a wheel braking process with a broad range of slip ratios up to 99% to gain insights into the development of thermal damages in practice. The specific test conditions are as follows.

The vertical (normal) wheel load ( $F_n$ ) was about 4000 N, resulting in a maximum contact pressure of 1.01 GPa, similar to the field conditions. The angle of attack was mini-

mized to reduce the wheel-rail lateral contact force, simulating the wheels running on straight tracks. The wheel running speed was 16 km/h. A nominal braking torque ( $M$ ) up to 120 N·m was applied to the wheel to generate slip ratios ranging from 2% to 99%.

Temperature data were recorded with the camera for 20 s, during which the wheel assembly completed about seven cycles along the ring track. During the test, the temperature measurement range 250 ~ 670 °C was initially applied. At a certain moment (around 11.3 s), the observed temperature reached the upper limit, and the measurement range was then manually adjusted to 600 ~ 1200 °C to capture higher contact temperatures. After the test, severe thermal damage was observed on both the wheel and rail surfaces, as shown in Figure 3.3.

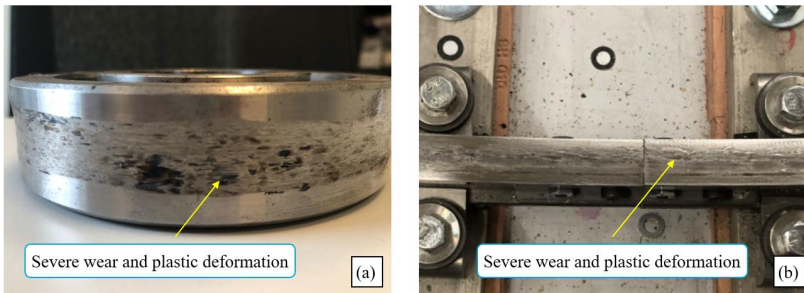


Figure 3.3: Severe thermal damages on the wheel and rail of the V-Track after the test. (a) Severe wear and plastic deformation on the wheel; (b) severe wear and plastic deformation on the rail.

### 3.3. CALIBRATION OF RAIL EMISSIVITY

Emissivity represents the efficiency factor of thermal radiation emission from the surface of an object [32]. The infrared thermal camera needs an input of the emissivity value of the target object beforehand in order to achieve reliable thermal measurements. The factory calibration of the infrared thermal camera used in this study was performed using a black target, whose spectral emissivity at room temperature (25 °C) is quantified as 1.0 [33]. In practice, the emissivity of most objects is below 1.0, determined by e.g., materials, surface roughness, and spectral wavelengths [34]. In this section, the emissivity of the rail samples of the V-Track was calibrated using the infrared thermal camera before the contact temperature measurements.

#### 3.3.1. EXPERIMENT SETUP FOR RAIL EMISSIVITY CALIBRATION

Figure 3.4 shows the experimental setup for the emissivity calibration of rail samples using a temperature-controlled furnace (Heraeus MR 170 E) and the infrared thermal camera. This furnace was capable of providing a controllable thermal environment up to 1200 °C. The emissivity of the rail samples can be determined by adjusting the emissivity value in the infrared thermal camera until it matched the baseline temperature provided by the furnace. Two pieces of rail samples made of R260 and R350HT were tested, identical to those used in the V-Track test rig, ensuring that the calibration aligned with the

subsequent temperature measurements. Half of the rail samples were coated with layers of thermographic paint [35] to avoid the influence of light reflection on the emissivity measurement [36]. Considering that the paint can be abraded during the wheel-rail frictional rolling contact test, the emissivity of uncoated rails were also calibrated, and compared to the coated cases to assess the impact of the coating on rail emissivity.

Emissivity calibrations were conducted under two distinct thermal conditions: 1) samples were heated to 600 °C, and 2) samples were heated to 950 °C. These conditions were designed according to the estimated contact temperature of the V-Track in high slip ratios from numerical modeling, which employed the same method as in [37]. The furnace was maintained at these two temperatures for 30 minutes to achieve a uniform sample temperature. The infrared thermal camera was positioned close to the furnace (0.6 m between the rail samples and the lens), as illustrated in Figure 3.4(c). Before the tests, the temperature range of the camera was pre-set to 250 °C ~ 670 °C and 600 °C ~ 1200 °C, respectively. To minimize the thermal dissipation of the rail samples to the surrounding air, the camera began recording when the rail samples were being moved out of the furnace.

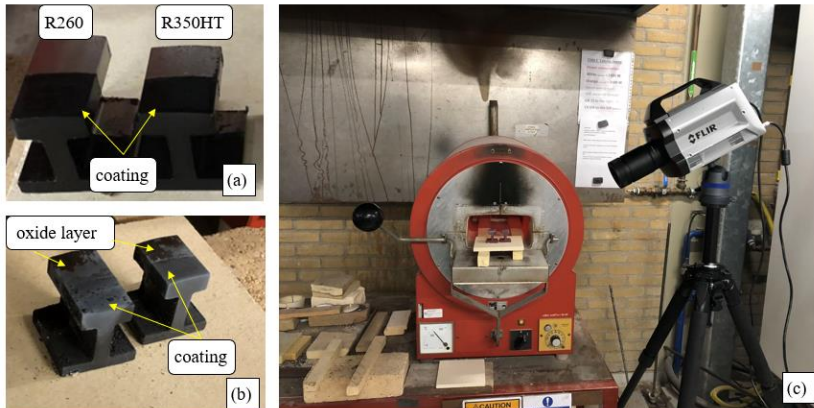


Figure 3.4: Emissivity calibration of the rail samples made of R260 and R350HT. (a) Rail samples before heating; (b) rail samples after heating up to 950 °C; (c) experimental setup for temperature measurement.

### 3.3.2. CALIBRATION RESULTS

Figure 3.5 shows the thermal images of the rail samples in the two heating conditions, i.e., at 600 °C and 950 °C. After being heated for 30 minutes in the furnace, the rail samples can be assumed to have reached thermal equilibrium, meaning that the temperature at each point of the samples was equal to the furnace setting. However, as shown in Figure 3.5, two distinct areas were observed on the rail heads, corresponding to the areas with and without coating. This difference was caused by the different emissivity values each had. The temperatures in Figure 3.5 were calculated based on the emissivity of rail samples without coating. Meanwhile, it was observed that at the junction of the rail foot and web the average temperature was higher compared to the rail head. This

can be attributed to that at the junction area the more complex interactions of convection, conduction, and radiation facilitate localized heat accumulation [38]. In addition, the two rail samples made of R260 and R350HT exhibited similar temperature distributions in both thermal conditions, indicating that the rail emissivity is insensitive to the steel grades.

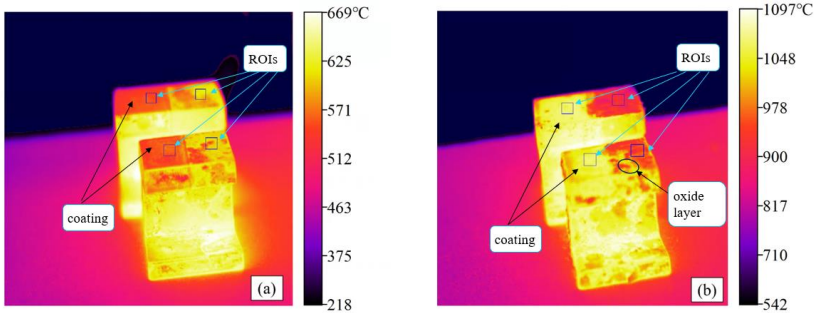


Figure 3.5: Thermal images of the rail samples under two heating conditions. (a) Rail samples were heated to 600 °C; (b) rail samples were heated to 950 °C.

The rail emissivity in these two cases was calibrated on the rail head, where wheel-rail interactions occur. Five regions of interest (ROIs) were defined on the heads of both coated and uncoated rails under each heating condition. To clearly display the ROIs, Figure 3.5 shows only one ROI, denoted by a small square, in each region. The local emissivity of rail samples was derived by adjusting the emissivity in the camera until the average temperature in ROI matched the furnace heating temperature. To minimize the random errors caused by uneven temperature distribution, the emissivity of samples was determined by averaging the values from the five ROIs.

Figure 3.6 shows the calibration results in these two thermal conditions. For the rail samples heating up to 600 °C, the calibrated emissivity values for the surfaces with and without coating were 0.72 (with a standard deviation of 2%) and 0.83 (with a standard deviation of 4%), respectively; at 950 °C, the corresponding values were 0.56 (with a standard deviation of 2.7%) and 0.43 (with a standard deviation of 3.1%). The emissivity of the coating rails was lower at 600 °C, but higher at 950 °C. This opposite trend could be due to the significant oxide layer in the uncoated rails when heating to 950 °C, as shown in Figure 3.4(b), which reduced the emissivity. The oxide layer, indicated by an oval in Figure 3.5(b), contributed to uneven temperature distributions on the uncoated rail surface, leading to greater uncertainty in the measured emissivity. To minimize this effect, ROIs were carefully selected to avoid areas with visible oxidation. The calibrated uncoated rail emissivity values of 0.83 and 0.43 were applied to wheel-rail contact temperature tests using the infrared thermal camera for the measurement ranges of 250 ~ 670 °C and 600 ~ 1200 °C, respectively.

### 3.4. RESULTS AND DISCUSSIONS

This section presents the measurement results of wheel-rail contact temperature in the V-Track under a wheel braking condition. A typical thermal damage, i.e., a “wheel flat”,

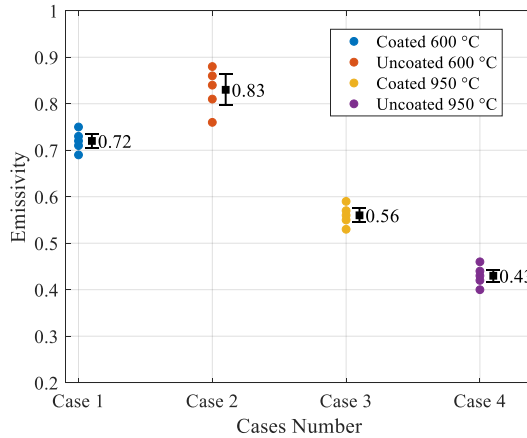


Figure 3.6: Rail emissivity calibration.

induced often by improper wheel braking in practice, was observed and analyzed in detail.

### 3.4.1. THERMAL RESULTS DURING BRAKING

Figure 3.7 shows the thermal results during a wheel-rail braking process. Figure 3.7(a) illustrates an example of the thermal image. The ROI 1 includes the wheel and rail surface areas close to the wheel-rail contact. The measured peak temperature within ROI 1 was extracted to obtain the time-history temperature curve, as shown in Figure 3.7(b). To clearly display the temperature variation, the raw temperature measurement data were smoothed with a window size of 50 points, as shown by the orange curve. Meantime, the corresponding wheel angular velocity and slip ratios calculated using equation (3.1) were synchronized and presented in Figures 3.7(c) and 3.7(d), respectively.

In Figures 3.7(b), (c), and (d), the time histories of the measurement data were divided into five segments (S1 to S5) based on different wheel-rail contact conditions. In the segment S1, from 0.000 s to 4.450 s, the temperature reading was a constant of 250 °C, which indicated the lower limit of the thermal camera setting (with a measurement range of 250 ~ 670 °C) and that the real contact temperature was below 250 °C. During this period, the wheel angular velocity was steady, slightly oscillating around 67 rad/s with a translational speed of 16 km/h, resulting in a slip ratio of approximately 2%.

In the segment S2, from 4.450 s to 8.114 s, the temperature gradually rose from 250 °C to 670 °C. 670 °C was the upper limit of the camera setting. During this process, the wheel angular velocity decreased from 67 rad/s to 41 rad/s, and the slip ratio increased significantly from approximately 2% to 40%.

In the segment S3, the contact temperature was observed to decline from about 670 °C to a low value of about 400 °C over the period from 8.114 s to 9.420 s. The main reason for this contact temperature drop can be that the cooler parts of the wheel and rail entered the contact area after a “wheel flat” was formed and then exited the contact

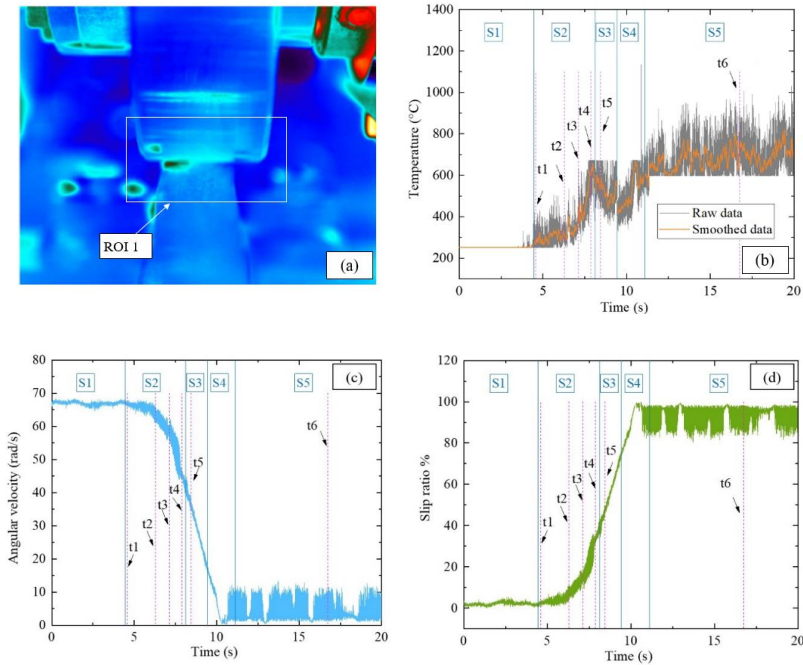


Figure 3.7: Thermal test results of wheel-rail contact in the V-Track. (a) A thermal image and ROI 1; (b) the measured temperature time history; (c) the measured wheel angular velocity; (d) the slip ratio.

area. A detailed analysis of the “wheel flat” occurrence will be presented in Section 3.4.2. During this period, it was observed that the wheel angular velocity kept decreasing from 41 rad/s to 18 rad/s, and the slip ratio increased further from approximately 40% to 75%.

In the segment S4, from 9.420 s to 11.339 s, the temperature rose again from about 400 °C to 670 °C. During this period, the angular velocity of the wheel dropped to almost zero and then oscillated below 10 rad/s, and the slip ratio approached 99% and then oscillated around 90% afterward. The significant oscillations can be attributed to wheel/rail unstable vibrations under the full-slip contact condition. To capture higher contact temperatures, at  $t = 11.339$  s, the camera temperature range was manually switched to 600 ~ 1200 °C during the measurement, and the rail emissivity changed from 0.83 to 0.43 accordingly.

In the segment S5, from 11.339 s to 20.000 s, the temperature fluctuated above 600 °C, and peaked at about 1000 °C, while the wheel angular velocity remained below 10 rad/s and the slip ratio fluctuated between 80% and 99%.

To better understand the three phases of the measured temperature, i.e., rise (S2), drop (S3), and extremely high temperature (S5), the thermal images captured by the camera at the instances  $t1 \sim t6$  (denoted in Figure 3.7) are presented in Figures 3.8 and 3.9. The thermal images in Figure 3.8 represent raw signals detected by the infrared thermal camera, called digital counts in the system. These counts can be converted into temper-

atures (displayed by the thermal images in Figure 3.9) automatically through calibration algorithms [39]. Compared to the temperature distribution images in Figure 3.9, the raw digital counts in Figure 3.8 provide a clearer view of the wheel-rail contact position. Due to the filter applied to the lens, the wheel and rail in Figure 3.8 cannot be seen as clearly as in Figure 3.7(a).

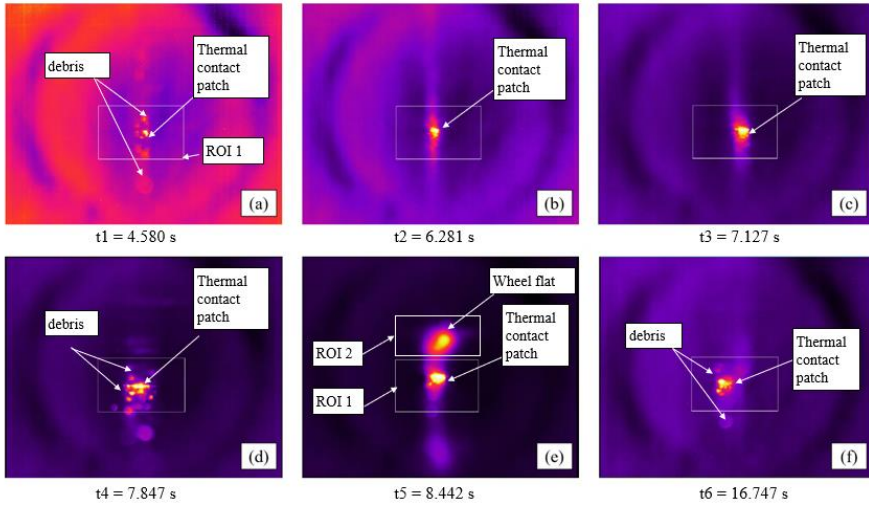


Figure 3.8: Raw thermal images captured as digital counts at the time instances  $t_1 \sim t_6$ , corresponding to (a) ~ (f).

Figure 3.8(a) shows the thermal image of wheel-rail contact at  $t_1 = 4.580$  s, with a corresponding slip ratio of approximately 3%. Figure 3.9(a) shows that the maximum temperature within the ROI 1 at  $t_1$  was  $269^\circ\text{C}$ , which was slightly higher than the lower limit of the camera measurement range setting ( $250^\circ\text{C}$ ). As the wheel moved along the rail, some steel debris due to surface wear can be seen flying towards the camera lens, as shown in Figure 3.8(a). This agrees with the finding reported in [3] that severe wear could occur when the temperature is higher than  $200^\circ\text{C}$ . Figure 3.9(a) depicts that the size of the thermal contact patch, i.e., the wheel-rail surface region with a temperature over  $250^\circ\text{C}$ , is quite small, and no debris can be seen because their temperatures were lower than  $250^\circ\text{C}$ .

In Figure 3.8(b), a thermal contact patch at  $t_2 = 6.281$  s is presented with a corresponding slip ratio of 7%. The thermal wheel-rail contact can be more clearly seen, in comparison to Figure 3.8(a). The maximum contact temperature within the ROI 1 at this instance was  $307^\circ\text{C}$ , as shown in Figure 3.9(b).

As the slip ratio increased to 15% at  $t_3 = 7.127$  s, the maximum temperature reached  $431^\circ\text{C}$ , as shown in Figure 3.9(c). The thermal contact patch size in Figure 3.9(c) further increased, meaning a larger surface region with a temperature above  $250^\circ\text{C}$ , due to the larger slip ratio and probably also the wear of the wheel and rail that changed the wheel-rail contact geometry and enlarged the contact patch.

As the slip ratio increased to 33% at  $t_4 = 7.874$  s in Figures 3.8(d) and 3.9(d), the max-

imum temperature of the ROI 1 reached  $670^{\circ}\text{C}$ , accompanied by some debris with the temperature as high as  $393^{\circ}\text{C}$ . At high temperatures, the material surface oxidized, and a brittle oxide layer was formed [40], which fractured more easily under mechanical stress, producing more debris.

At  $t_5 = 8.442\text{ s}$ , with slip ratio increased to 48%, both the thermal contact patch (within ROI 1) and the “wheel flat” (within ROI 2) are visible in the thermal image in Figure 3.8(e). The maximum temperature of ROI 1 was  $575^{\circ}\text{C}$ , lower than that at  $t_4$ . As explained above, this is mainly because after the “wheel flat” was formed and then exited the wheel-rail contact area, the cooler parts of the wheel and rail entered the contact area. Another reason could be that the occurrence of a “wheel flat” caused significant material removal and exposed the cooler material underneath. The maximum temperature in the “wheel flat” area was  $330^{\circ}\text{C}$  at  $t_5$ , and the cooling process of the “wheel flat” over time, including from  $t_4$  to  $t_5$ , will be discussed in Section 3.4.2.

At  $t_6 = 16.741\text{ s}$ , with the slip ratio increased to 86%, the maximum temperature of the thermal contact patch reached  $889^{\circ}\text{C}$ , as shown in Figure 3.9(f). Figure 3.8(f) shows that the contact patch was also accompanied by some debris, indicating significant surface damage, aligning with the observations in Figure 3.3. The size of the thermal contact patch in Figure 3.9(f) seems smaller than that in Figure 3.9(e), mainly because of the change of the camera measurement range setting, as indicated by the color bars of the graphs.

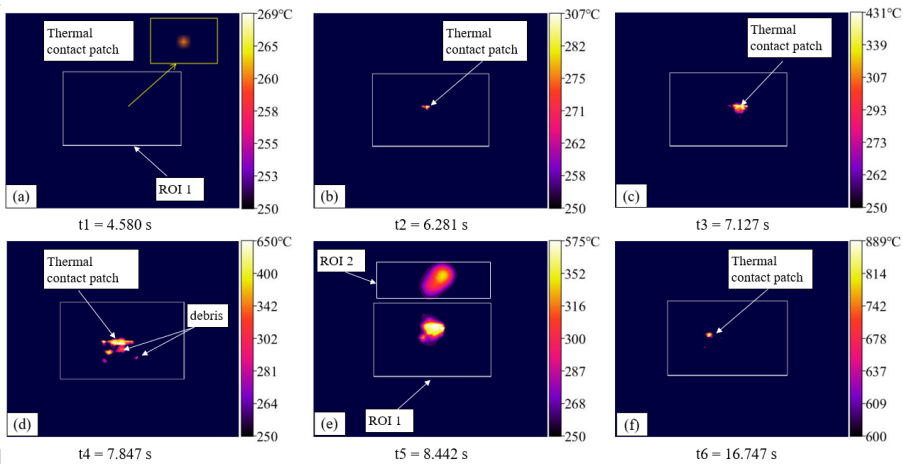


Figure 3.9: Thermal images indicating the wheel and rail surface temperatures at the time instances  $t_1$  to  $t_6$ , corresponding to (a) ~ (f).

### 3.4.2. A “WHEEL FLAT” OBSERVATION

The “wheel flat” was generated in the wheel-rail contact patch at about  $8.114\text{ s}$ . As the wheel rolled forward, the “wheel flat” moved upwards in the thermal images from the wheel’s trailing side and finally went out of the view of the camera at  $8.645\text{ s}$ . This process lasted for a total of  $0.531\text{ s}$ , during which 531 thermal images were captured by the

camera. The thermal images of four representative moments,  $m1 \sim m4$ , are displayed in Figure 3.10.

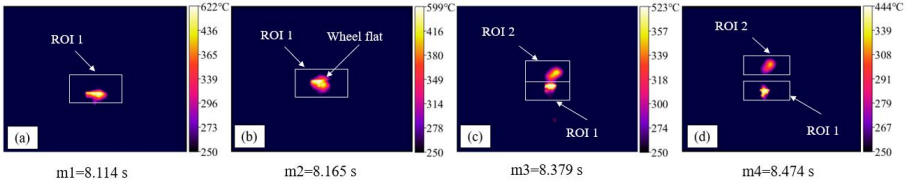


Figure 3.10: Thermal image of the “wheel flat” and the camera-targeting temperature ((a) ~ (d) represent the moments of the temperature variation of wheel flat ( $m1 \sim m4$ )).

In Figure 3.10(a), at  $m1 = 8.114$  s, the “wheel flat” was just generated and basically overlapped with the thermal contact patch in the thermal image. The highest temperature within ROI 1 was  $622^\circ\text{C}$ , and the corresponding wheel angular velocity and slip ratio were  $41$  rad/s and  $40\%$ , respectively. At  $m2 = 8.165$  s, as shown in Figure 3.10(b), the “wheel flat” began to separate from the wheel-rail contact patch as the wheel rolled forward, and the highest temperature fell to  $599^\circ\text{C}$ . Because the “wheel flat” was largely overlapping with the thermal contact patch at  $m1$  and  $m2$ , we approximated the peak temperatures within ROI 1 as the maximum temperatures of the “wheel flat” at these moments.

In Figure 3.10(c), the thermal contact patch and the “wheel flat” are distinct at  $m3 = 8.379$  s, appearing within two separate areas, ROI 1 and ROI 2, respectively. The maximum temperature within ROI 1 fell to  $523^\circ\text{C}$ , while that within ROI 2 was  $360^\circ\text{C}$ . At  $m4 = 8.474$  s, the maximum temperature within ROI 1 further declined to  $444^\circ\text{C}$ , while the temperature of the “wheel flat” was reduced to  $318^\circ\text{C}$ , as shown in Figure 3.10(d).

A cooling process of the “wheel flat” can be seen in Figure 3.10, indicated by the reduction of the maximum temperature of the “wheel flat” and the shrinkage of the “wheel flat” thermal area. To further examine this cooling process, the evolution of the “wheel flat” temperature over time was analyzed. As mentioned above, the peak temperatures within ROI 1 were approximated as the “wheel flat” temperature before the separation of the wheel-rail contact patch and the “wheel flat” (e.g., Figures 3.10(a) and (b)); and after the separation (e.g., Figures 3.10(c) and (d)), the peak temperature within ROI 2 was taken as the “wheel flat” temperature. The maximum “wheel flat” temperatures measured over the period from  $8.114$  s to  $8.645$  s were plotted together with an exponentially fitted curve in Figure 3.11.

The fitted temperature-decreasing curve plotted in Figure 3.11 can be described by equation (3.2):

$$T = 670.73e^{\left(\frac{-3.89(t-8.11)}{0.53}\right)} + 220.20 \quad (3.2)$$

where  $T$  is the temperature ( $^\circ\text{C}$ ) and  $t$  is the time (s). As mentioned before, the “wheel flat” was first captured by the thermal camera at  $8.114$  s with a temperature of  $622^\circ\text{C}$ . Considering that the camera-targeting patch was  $4.5$  mm behind the trailing edge of the wheel-rail contact area, as shown in Figure 3.2(d), the peak temperature of wheel-rail contact, occurring at the trailing edge of the contact area [37], was measured with a small

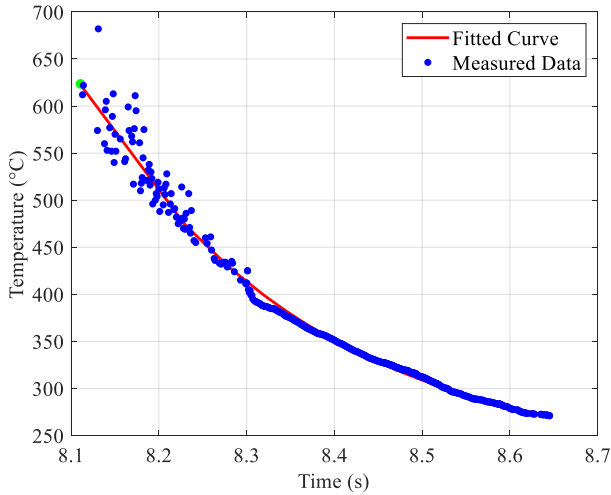


Figure 3.11: The measured and fitted maximum temperature of the “wheel flat” decreased with time from 8.114 s to 8.645 s.

time lag of 1.013 ms (4.5 mm divided by wheel running speed 16 km/h). Therefore, when the “wheel flat” was generated, the maximum wheel-rail contact temperature occurred at 8.113 s, and the value can be estimated with equation (3.2) as 624 °C, as represented by the green dot in Figure 3.11.

### 3.5. CONCLUSIONS

In this study, a measurement system was developed in the V-Track test rig equipped with an infrared thermal camera to measure a broad range of temperatures at the wheel-rail frictional rolling contact. The camera was mounted on the trailing side of a moving wheel by a customized steel frame, which enabled continuous monitoring of flash wheel-rail contact temperatures under running conditions. The rail emissivity was calibrated to obtain reliable thermal contact measurements. To gain insights into the development of thermal damages, the wheel-rail contact temperature was measured under a wheel braking condition with high slip ratios ranging from 2% to 99%. A “wheel flat” was generated during the braking process, and the resulting temperature field was examined over time. The main conclusions of this study are summarized as follows:

- The developed measurement system can reliably and continuously measure the wheel-rail contact temperatures up to 1200 °C, as well as the transient thermal phenomena such as the cooling process.
- The rail emissivity was calibrated using the infrared thermal camera, with values of 0.83 at 600 °C and 0.43 at 950 °C. It is also found that the emissivity is insensitive to rail grades.
- The wheel-rail contact temperature rose with the slip ratio until a “wheel flat” was

formed. The contact temperature dropped when the “wheel flat” exited the contact area and then increased again with the slip ratio. The contact temperature may reach up to 1000 °C with a slip ratio of 99%.

- A “wheel flat” was generated when the slip ratio reached around 40%, and the corresponding wheel-rail contact temperature was 624 °C. By tracing the temperature drop of the “wheel flat” area over time, a wheel-rail contact temperature-evolution curve was obtained, which can be well fitted with an exponential curve.

This study enhances the understanding of thermal damage mechanisms related to wheel-rail interactions, especially under high-temperature conditions. The presented measurement results may serve as references for calibrating and validating numerical thermal contact and damage models. Future research may involve a metallographic analysis to examine the microstructures of the wheel and rail tested in this study and to further reveal their damage mechanisms under the thermal loads.

# BIBLIOGRAPHY

- [1] Q. Lian et al. “Thermo-mechanical coupled finite element analysis of rolling contact fatigue and wear properties of a rail steel under different slip ratios”. In: *Tribology International* 141 (2020), p. 105943. DOI: [10.1016/j.triboint.2019.105943](https://doi.org/10.1016/j.triboint.2019.105943).
- [2] J. P. Srivastava, P. K. Sarkar, and V. Ranjan. “Effects of thermal load on wheel–rail contacts: A review”. In: *Journal of Thermal Stresses* 39 (2016), pp. 1389–1418. DOI: [10.1080/01495739.2016.1216060](https://doi.org/10.1080/01495739.2016.1216060).
- [3] R. Lewis and R. Dwyer-Joyce. “Wear mechanisms and transitions in railway wheel steels”. In: *Proceedings of the Institution of Mechanical Engineers, Part J: Journal of Engineering Tribology* 218 (2004), pp. 467–478. DOI: [10.1243/1350650042794815](https://doi.org/10.1243/1350650042794815).
- [4] A. M. S. Asih, K. Ding, and A. Kapoor. “Modelling rail wear transition and mechanism due to frictional heating”. In: *Wear* 284-285 (2012), pp. 82–90. DOI: [10.1016/j.wear.2012.02.017](https://doi.org/10.1016/j.wear.2012.02.017).
- [5] Y. Z. Chen et al. “The influence of wheel flats formed from different braking conditions on rolling contact fatigue of railway wheel”. In: *Engineering Failure Analysis* 93 (2018), pp. 183–199. DOI: [10.1016/j.engfailanal.2018.07.006](https://doi.org/10.1016/j.engfailanal.2018.07.006).
- [6] A. Böhmer, M. Ertz, and K. Knothe. “Shakedown limit of rail surfaces including material hardening and thermal stresses”. In: *Fatigue & Fracture of Engineering Materials & Structures* 26 (2003), pp. 985–998. DOI: [10.1046/j.1460-2695.2003.00690.x](https://doi.org/10.1046/j.1460-2695.2003.00690.x).
- [7] C. Bernsteiner et al. “Development of white etching layers on rails: simulations and experiments”. In: *Wear* 366-367 (2016), pp. 116–122. DOI: [10.1016/j.wear.2016.03.028](https://doi.org/10.1016/j.wear.2016.03.028).
- [8] S. L. Grassie et al. “Studs: a squat-type defect in rails”. In: *Proceedings of the Institution of Mechanical Engineers, Part F: Journal of Rail and Rapid Transit* 226 (2011), pp. 243–256. DOI: [10.1177/0954409711421462](https://doi.org/10.1177/0954409711421462).
- [9] R. I. Carroll and J. H. Beynon. “Rolling contact fatigue of white etching layer: Part 1”. In: *Wear* 262 (2007), pp. 1253–1266. DOI: [10.1016/j.wear.2007.01.003](https://doi.org/10.1016/j.wear.2007.01.003).
- [10] J. P. Srivastava et al. “A numerical study on effects of friction-induced thermal load for rail under varied wheel slip conditions”. In: *Simulation* 95 (2018), pp. 351–362. DOI: [10.1177/0037549718782629](https://doi.org/10.1177/0037549718782629).
- [11] R. Zunsong. “An investigation on wheel/rail impact dynamics with a three-dimensional flat model”. In: *Vehicle System Dynamics* 57 (2018), pp. 369–388. DOI: [10.1080/00423114.2018.1469774](https://doi.org/10.1080/00423114.2018.1469774).

- [12] K. Handa and F. Morimoto. "Influence of wheel/rail tangential traction force on thermal cracking of railway wheels". In: *Wear* 289 (2012), pp. 112–118. DOI: [10.1016/j.wear.2012.04.008](https://doi.org/10.1016/j.wear.2012.04.008).
- [13] R. Komanduri and Z. Hou. "A review of the experimental techniques for the measurement of heat and temperatures generated in some manufacturing processes and tribology". In: *Tribology International* 34 (2001), pp. 653–682. DOI: [10.1016/S0301-679X\(01\)00068-8](https://doi.org/10.1016/S0301-679X(01)00068-8).
- [14] D. Meresse et al. "Determination of heat repartition parameters on high speed pin-on-disc tribometer by inverse heat conduction method". In: *Key Engineering Materials* 504-506 (2012), pp. 1061–1066. DOI: [10.4028/www.scientific.net/KEM.504-506.1061](https://doi.org/10.4028/www.scientific.net/KEM.504-506.1061).
- [15] Y. Wei, Y. Wu, and Z. Chen. "An experimental measurement and numerical calculation method on friction temperature rise of sliding contact pairs - taking rail/wheel contact as an example". In: *Journal of Measurements in Engineering* 11 (2023), pp. 1–11. DOI: [10.21595/jme.2023.22974](https://doi.org/10.21595/jme.2023.22974).
- [16] X. Tian et al. "The development and use of thin film thermocouples for contact temperature measurement". In: *Tribology Transactions* 35 (1992), pp. 491–499. DOI: [10.1080/10402009208982147](https://doi.org/10.1080/10402009208982147).
- [17] B. Tian et al. "Effect of magnetron sputtering parameters on adhesion properties of tungsten-rhenium thin film thermocouples". In: *Ceramics International* 44 (2018), S15–S18. DOI: [10.1016/j.ceramint.2018.08.334](https://doi.org/10.1016/j.ceramint.2018.08.334).
- [18] K. G. Kreider, S. Semancik, and C. Olson. "Advanced thin film thermocouples". In: (1984).
- [19] J. Pearce, M. Burstow, and M. Podesta. "Understanding wheel/rail interaction with thermographic imaging". In: *22nd International Symposium on Dynamics of Vehicles on Roads and Tracks*. 2021.
- [20] D. Yamamoto. "Improvement of method for locating position of wheel/rail contact by means of thermal imaging". In: *Quarterly Report of RTRI* 60 (2019), pp. 65–71. DOI: [10.2219/rtriqr.60.1\\_65](https://doi.org/10.2219/rtriqr.60.1_65).
- [21] B. Firlik, T. Staśkiewicz, and M. Słowiński. "Thermal imaging of the wheel-rail interface". In: *Proceedings of the Institution of Mechanical Engineers, Part F: Journal of Rail and Rapid Transit* (2023). DOI: [10.1177/09544097231155573](https://doi.org/10.1177/09544097231155573).
- [22] E. A. Gallardo-Hernandez, R. Lewis, and R. S. Dwyer-Joyce. "Temperature in a twin-disc wheel/rail contact simulation". In: *Tribology International* 39 (2006), pp. 1653–1663. DOI: [10.1016/j.triboint.2006.01.028](https://doi.org/10.1016/j.triboint.2006.01.028).
- [23] M. Naeimi et al. "Thermomechanical analysis of the wheel-rail contact using a coupled modelling procedure". In: *Tribology International* 117 (2018), pp. 250–260. DOI: [10.1016/j.triboint.2017.09.010](https://doi.org/10.1016/j.triboint.2017.09.010).
- [24] M. Naeimi et al. "Development of a new downscale setup for wheel-rail contact experiments under impact loading conditions". In: *Experimental Techniques* 42 (2017), pp. 1–17. DOI: [10.1007/s40799-017-0216-z](https://doi.org/10.1007/s40799-017-0216-z).

- [25] P. Zhang, J. Moraal, and Z. Li. “Design, calibration and validation of a wheel-rail contact force measurement system in V-Track”. In: *Measurement* 175 (2021), p. 109105.
- [26] Z. Yang et al. “An experimental study on the effects of friction modifiers on wheel-rail dynamic interactions with various angles of attack”. In: *Railway Engineering Science* 30 (2022), pp. 360–382. DOI: [10.1007/s40534-022-00285-y](https://doi.org/10.1007/s40534-022-00285-y).
- [27] P. Zhang and Z. Li. “Experimental study on the development mechanism of short pitch corrugation using a downscale V-Track test rig”. In: *Tribology International* 180 (2023). DOI: [10.1016/j.triboint.2023.108293](https://doi.org/10.1016/j.triboint.2023.108293).
- [28] P. Zhang and Z. Li. “New experimental evidences of corrugation formation due to rail longitudinal vibration mode”. In: *International Journal of Rail Transportation* 2024 (2024). DOI: [10.1080/23248378.2024.2336503](https://doi.org/10.1080/23248378.2024.2336503).
- [29] Teledyne FLIR. *X6900sc MWIR - Overview*. Retrieved January 2024, from <https://www.flir.eu/support/products/x6900sc-mwir/#0verview>. 2024.
- [30] M. J. E. Planck. *The theory of heat radiation*. Vol. 144. 1900, p. 164.
- [31] O. Schreer et al. “Multispectral high-speed midwave infrared imaging system”. In: *Infrared Technology and Applications XXX, SPIE*. 2004, pp. 249–257.
- [32] Y. M. Guo et al. “Measurement of directional spectral emissivity at high temperatures”. In: *International Journal of Thermophysics* 40 (2018). DOI: [10.1007/s10765-018-2472-2](https://doi.org/10.1007/s10765-018-2472-2).
- [33] Y. Té et al. “High emissivity blackbody for radiometric calibration near ambient temperature”. In: *Metrologia* 40 (2003), p. 24.
- [34] J. Guthrie and B. Sparr. “Infrared study of factors affecting the emissivity of aluminum”. In: *Applied Spectroscopy* 45 (1991), pp. 588–596. DOI: [10.1366/0003702914337038](https://doi.org/10.1366/0003702914337038).
- [35] LabIR Paints. *HERP-HT: Thermographic paint for high temperature applications*. Retrieved July 2024, from <https://paints.labir.cz/en/paints/herp-ht/>.
- [36] S. Bagavathiappan et al. “Infrared thermography for condition monitoring – A review”. In: *Infrared Physics & Technology* 60 (2013), pp. 35–55. DOI: [10.1016/j.infrared.2013.03.006](https://doi.org/10.1016/j.infrared.2013.03.006).
- [37] C. He et al. “A finite element thermomechanical analysis of the development of wheel polygonal wear”. In: *Tribology International* 195 (2024). DOI: [10.1016/j.triboint.2024.109577](https://doi.org/10.1016/j.triboint.2024.109577).
- [38] J. P. Holman. *Heat Transfer: Tenth Edition*. McGraw-Hill Education, 2010.
- [39] O. Gonzalez-Chavez et al. “Radiometric calibration of digital counts of infrared thermal cameras”. In: *IEEE Transactions on Instrumentation and Measurement* 68 (2019), pp. 4387–4399. DOI: [10.1109/tim.2018.2887070](https://doi.org/10.1109/tim.2018.2887070).
- [40] P. J. Blau. “Elevated-temperature tribology of metallic materials”. In: *Tribology International* 43 (2010), pp. 1203–1208. DOI: [10.1016/j.triboint.2010.01.003](https://doi.org/10.1016/j.triboint.2010.01.003).



# 4

## THERMOMECHANICAL FINITE ELEMENT WHEEL-RAIL CONTACT MODELING AND EXPERIMENTAL VALIDATION

*Frictional heat is generated at the wheel-rail interface during train operations, particularly under high slip ratios during acceleration and braking. Thermal effects can accelerate wear, induce plastic deformation, and contribute to thermal fatigue. Reliable modeling of wheel-rail contact that considers friction-induced thermal effects is desirable for the accurate prediction of wheel-rail interface deterioration. Several analytical and numerical models have been proposed to simulate thermal or thermomechanical wheel-rail loads but have rarely been validated, especially in high slip ratio scenarios where flash temperatures exceed 200 °C. This study develops and experimentally validates a three-dimensional thermomechanical finite element (FE) wheel-rail contact model for high slip ratio conditions, with contact temperatures reaching 360 °C. The model incorporates key mechanical parameters, including wheel loads, coefficients of friction, and slip ratios. Simulated rail surface temperatures across various slip ratios (5%, 10%, and 15%) are compared with the flash temperatures measured with an onboard infrared thermal camera, showing good agreement with a maximum deviation of 9.9%. This confirms the reliability of the model for simulating wheel-rail contact under thermal effects.*

---

This chapter has been published as: He, C., Yang, Z., Zhang, P., Dollevoet, R., Li, Z. (2025). Thermomechanical finite element modeling of wheel-rail contact and experimental validation. *Tribology International*, 209, 110666.

## 4.1. INTRODUCTION

**F**RICTIONAL heat generation at the wheel-rail interface is a significant occurrence during train operations, especially during acceleration and braking. Substantial wheel-rail thermal loading occurs at high slip ratios because of the rapid accumulation of thermal energy and the consequent increase in temperature in the contact area. This thermal loading is known to accelerate wear and plastic deformation and cause thermal fatigue in wheel/rail materials [1, 2]. Wheel/rail materials can be easily worn when the wheel-rail contact temperature exceeds 350 °C [3]. Thermal fatigue occurs when thermal loading alters the shakedown behavior and mechanical properties of materials [4, 5]. The elastic and shakedown limits of a wheel and rail can be reduced under thermal loading, increasing the vulnerability of the steel to progressive plastic deformation. This may lead to crack initiation and potential structural failure, even under relatively low mechanical stresses. In addition, high temperatures may induce microstructural transformations in wheel/rail materials, such as the transformation of pearlite and ferrite into austenite, followed by partial conversion into martensite beneath wheel and rail surfaces (occurring above 720 °C with rapid cooling) [6, 7]. This deterioration of the wheel-rail interface increases maintenance costs and impacts the operational safety of trains. Therefore, it is important to investigate wheel-rail friction-induced temperature and its effects on wheel/rail damage.

Accurately measuring the contact temperature between the wheel and rail under operational conditions is a complex, labor-intensive, and expensive process [8], which has led to the development of analytical and numerical modeling methods to examine the thermal loading and temperature field at the wheel-rail interface. Several analytical approaches have been formulated to calculate the maximum flash temperature induced by a moving heat flux in a single body. Jaeger [9] investigated the problem of idealized plane heat sources of various shapes, such as two-dimensional (2D) uniformly distributed band sources and three-dimensional (3D) rectangular sources, moving at constant or nonconstant velocities on the surface of a semi-infinite medium. Subsequent analyses then extended Jaeger's approach in two aspects: 1) by applying different moving heat sources [10, 11] and 2) by including the thermal radiation and convection to the ambient environment [12, 13]. A 2D elliptical band source was modeled in [10] to represent the heat induced by contact. Instead of applying a predefined heat source as in [9, 10], Knothe et al. [11] calculated the 2D heat source at the wheel-rail interface on the basis of Hertzian contact pressure and analytically derived the temperature field engendered by wheel-rail sliding interactions through the application of Laplace transforms and Green's function. Their study revealed that the wheel-rail contact temperatures do not exceed 450 ~ 500 °C if the slip ratio is less than 2% and the coefficient of friction is less than 0.6. By considering the heat interaction with the ambient environment (i.e., radiation and convection), Lewis et al. [12] calculated the temperature field induced by twin-disc rolling contact from partial to full slip (slip ratio from 0.5% to 5%) and determined that the maximum contact temperature above ambient temperature reached 113 °C under a normal contact stress of 1500 MPa and a disc surface velocity of 0.98 m/s. To investigate the effects of contact body geometry on contact temperature, thinner and smaller twin discs operating under the same conditions as [12] were simulated in [13], which reported higher simulated contact temperatures (199.2 °C for the thinner discs

and 235.3 °C for the smaller discs) than the results obtained in [12]. These analytical studies [9–13] indicated that the instantaneous temperatures generated at the contact interface are related to the coefficient of friction, contact pressure, thermal properties, sliding velocity, and contact body geometry.

In contrast to analytical models, finite element (FE) models can address transient thermal contact issues while considering complex geometries and material complexity, including plasticity, temperature dependence [14], and dynamic wheel-rail interactions. Vo et al. [15] developed a 3D FE model for a rail subjected to multiple thermal loads from passing locomotives, employing Goldak's heat source model [16]. A simulation with a slip ratio of 8.5% indicated that the rail-surface temperature can reach 522 °C after one wheel pass and 723 °C after six passes. However, the heat source of the model was calculated on the basis of Hertzian contact pressure. Such a simplification can potentially lead to deviations in the thermal results from the actual values. Naeimi et al. [14] proposed a 3D dynamic thermomechanical FE wheel-rail contact model in which the heat source was calculated on the basis of the tangential load and micro-slip between the elements in contact. The simulated peak contact temperatures with slip ratios of 10%, 18%, and 26% were 284 °C, 498 °C, and 756 °C, respectively. Lian et al. [8] presented a 3D FE wheel-rail contact model to consider the superimposed thermomechanical loads induced by multiple wheel passages. Their study indicated that the maximum temperature of the rail surface after 9 wheel passages can reach 776 °C, with a slip ratio of 9.43%.

In terms of model validation, attempts were made in [17] to validate the analytical model presented in [12] for low slip ratio (below 5%) wheel-rail contact scenarios via infrared cameras. The results indicated that the measured contact temperature ranged between 100 and 150 °C with a slip ratio of 5%, which aligned well with the simulated results in [12]. However, although FE models of thermal contact between wheels and braking blocks [18–20] or braking pads [21] have been experimentally validated via infrared cameras, no validation, to the best of the author's knowledge, has been reported for FE wheel-rail thermal contact models with high slip ratios (above 5%) that may induce significant thermal damage.

In this study, a 3D thermomechanical FE wheel-rail contact model was constructed, and the model was validated with a carefully designed laboratory test. Wheel-rail contact across a range of slip ratios from 2% to 35% during braking was reproduced using the TU-Delft V-Track test rig, which is a downscaled wheel-rail interaction test rig, and the corresponding contact temperature was captured with an onboard high-precision infrared thermal camera. This measurement captured real-time flash temperatures induced by wheel-rail contact up to 670 °C. Section 4.2 presents the thermomechanical FE contact model, the methodology for measuring wheel-rail contact temperature, and the approach for calculating the slip ratio. Section 4.3 first presents the measurement data processing and then examines the correlation between the measured temperatures and slip ratios. A comparative analysis between the simulated and measured wheel-rail contact temperatures is subsequently presented. Section 4.4 presents the main conclusions. The primary aim of this study is to experimentally validate the proposed FE model by comparing the simulated wheel-rail contact temperatures with those obtained from experiments conducted on a V-Track test rig.

## 4.2. METHOD

### 4.2.1. NUMERICAL MODEL

A 3D thermomechanical FE wheel-rail contact model was constructed, incorporating its geometrical, mechanical, and material characteristics (R260 and R350HT rail grades) in the V-Track, as depicted in Figure 4.1. This model is capable of replicating the motion of a wheel traveling along a track at a predefined slip ratio during braking. The same braking process of the wheel was measured on the V-Track, as described in Section 4.2.2. The simulation procedure of the FE model includes four steps: 1) Modeling of wheel-rail contact in the V-Track test rig (preprocessing in ANSYS); 2) Static equilibrium of the wheel loading on the rail (implicit solution); 3) Dynamic rolling of the wheel along the rail (explicit solution); 4) Results output and analysis (postprocessing with MATLAB). The implicit-explicit sequential analysis (combining steps 2 and 3) can effectively mitigate initial dynamic excitation.

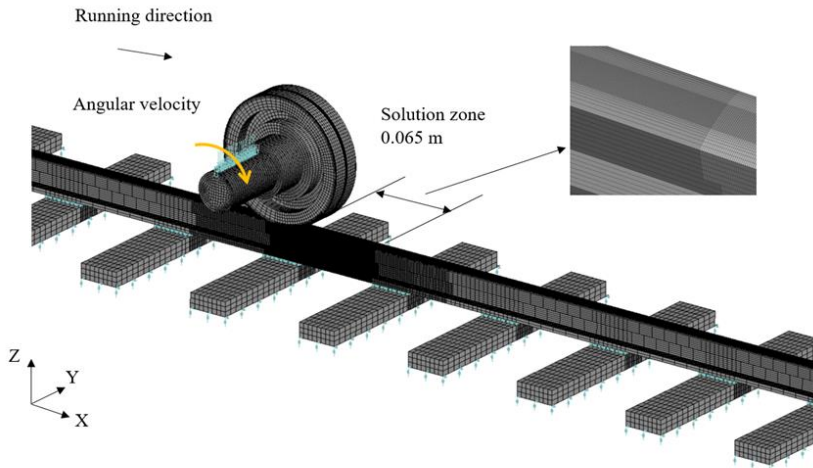


Figure 4.1: Thermomechanical FE model of wheel-rail contact on the test rig.

The preprocessing of FE modeling included geometry and material modeling, structural discretization, and the definitions of boundary conditions (including contact pairs), loads, and initial conditions. In terms of the geometry within the FE model, the track model spanned a total length of 1.75 metres, encompassing 14 sleeper spans, and included a 0.065-metre solution zone along the rail. The rail was fixed to the sleepers through fastenings in three directions. The sleepers were supported by the ballast and the subgrade, which were represented by the rubber pads and plywood layers in the test rig. A wheel with a radius of 65 mm (1/7 scale of the field wheels) and a half axle were modeled. Two distinct sets of temperature-dependent material parameters that have been widely used for wheel-rail thermomechanical behavior modeling [8, 14, 15, 22–25] were employed, with one set detailed in Tables 4.1 and 4.2 [8, 14, 15, 23, 25] and the other set listed in Table 4.3 [22, 24]. The thermal conductivities in Tables 4.2 and 4.3

were downscaled (1/7 scale) in this study on the basis of the similarity law [26]. The parameters in equation (4.2) of this study can be appropriately scaled, while temperature remains unscaled, according to [26]. Consequently, the measured temperature in the V-Track test rig can directly represent the corresponding values in the full-scale wheel-rail contact under field conditions. The simulation results obtained with different sets of material parameters are compared in Section 4.3. In the discretization process of the model, the primary suspension springs in the V-Track test rig were modeled via compressed spring-damper elements. These elements connected the wheel axle to lumped mass elements, which were simplified from the wheel axle box and the guiding block of the V-Track test rig, as described in Section 4.2.2. The wheel, rail, and sleepers were modeled with 8-node solid elements. The fastenings, ballast, and subgrade were modeled with spring-damper elements. To improve the calculation efficiency, a partially refined mesh strategy was applied. The finest mesh size of the top surface in the solution zone of the rail was 0.18 mm (x-axis)  $\times$  0.20 mm (y-axis)  $\times$  0.20 mm (z-axis). The FE model comprises 577,907 elements and 646,016 nodes. The minor axis of the contact patch covers 13 contact elements; thus, sufficiently accurate contact solutions can be obtained for engineering applications [27].

Table 4.1: Temperature-dependent mechanical material parameters [8, 14, 15, 23, 25]

Temperature, T (°C)	Young's modulus, E (GPa)	Poisson's ratio, $\nu$	Coefficient of thermal expansion, ( $\times 10^{-6}$ °C $^{-1}$ )	Hardening modulus, Ep (GPa)	Yield strength of R260 (MPa)	Yield strength of R350HT (MPa)	Yield strength of wheel (MPa)
24	213	0.295	9.89	22.7	583.0	779.0	500.0
230	201	0.307	10.82	26.9	585.1	781.1	502.1
358	193	0.314	11.15	21.3	518.8	714.8	435.8
452	172	0.320	11.27	15.6	432.4	628.4	349.4
567	102	0.326	11.31	6.2	251.1	447.1	168.1
704	50	0.334	11.28	1.0	136.2	332.2	53.2
900	43	0.345	11.25	0.1	113.4	309.4	30.4

Table 4.2: Temperature-dependent thermal material parameters [8, 14, 15, 23, 25]

Temperature, T (°C)	Specific heat capacity, c (J/kg°C)	Thermal conductivity, (W/m°C)
0	419.5	8.53
350	629.5	5.84
703	744.5	4.32
704	652.9	4.31
710	653.2	4.29
800	657.7	3.57
950	665.2	3.86
1200	677.3	4.35

An implicit-explicit sequential analysis was conducted to simulate wheel braking along the rail. The longitudinal (rolling direction) and lateral degrees of freedom of the wheel were first constrained to calculate the static equilibrium in the implicit analysis,

Table 4.3: Temperature-dependent thermomechanical material parameters [22, 24]

Temperature, T (°C)	Young's modulus, E (GPa)	Poisson's ratio, $\nu$	Coefficient of thermal expansion, ( $\times 10^{-6}$ °C <sup>-1</sup> )	Hardening modulus, Ep (GPa)	Specific heat capacity, c (J/kg°C)	Thermal conductivity, (W/m°C)	Yield strength of R260 (MPa)	Yield strength of R350HT (MPa)
25	209	0.30	11.0	20.9	490.1	6.81	583.0	779.0
100	207	0.30	11.6	20.7	499.9	6.99	583.0	779.0
650	105	0.36	14.8	10.5	571.5	8.26	477.0	673.0
1000	50	0.39	15.7	5.0	617.1	9.06	415.4	611.4
1450	2	0.40	16.1	0.2	671.8	10.91	151.3	347.3

where a gravity wheel load of 4000 N was applied. The longitudinal constraints of the wheel were then released in the explicit model for wheel rolling simulations, where a friction coefficient of 0.45 between the wheel and rail was applied. This applied friction coefficient was measured from the V-Track, based on the wheel-rail friction force and normal contact force recorded using dynamometers. When friction saturation occurred under high slip ratio conditions, the adhesion coefficient, i.e., the ratio of friction force to normal load, can be taken as the measured friction coefficient. The measured lateral friction force was close to zero with a careful control of the angle of attack in the V-Track. A fixed boundary condition was thus applied to the wheel axle in the lateral direction to minimize the simulated wheel-rail lateral force and its influence on the contact temperatures. The nodal displacements, obtained from the static equilibrium calculation, served as an initial condition for the explicit model. Another initial condition was the initial temperature of the wheel and rail, which was assumed to be 200 °C. The measurement was conducted with a continuous increase in slip ratio from 2% to 35%, and the simulation conditions were designed to be consistent with the experimental setup. In the test, by the time the slip ratio reached 5%, the wheel had already been braking for a period, leading to heat accumulation in both the wheel and rail. Therefore, in the simulation, the initial temperature was not set to ambient but accounted for this accumulated thermal effect to better reflect the actual conditions observed in the experiment. The translational velocity of the wheel was 16 km/h, and the angular velocity was controlled accordingly to simulate specific slip ratios during braking.

In this study, to address the complexities of the wheel-rail thermal contact phenomenon, both mechanical and thermal solvers were employed in the simulation. During wheel-rail frictional contact (calculated in the mechanical solver), kinetic energy is transformed into heat (calculated in the thermal solver), which consequently induces wheel-rail geometrical changes and affects the temperature-dependent material properties (employed as geometrical and material inputs for the mechanical solver). Concurrent operation and data exchange between the two solvers can be realized via a two-way coupling methodology implemented in LS-DYNA. The computation time steps of the two solvers were as follows:  $1.06 \times 10^{-8}$  for the mechanical solver and  $1.00 \times 10^{-6}$  for the thermal solver. Note that for both solvers, a small computation time step prolongs the computation time, whereas a large time step may induce numerical instabilities.

The governing equation of the mechanical solver involving the thermal effect is defined in equation (4.1) [28, 29].

$$M\ddot{u}(t) + C(T)\dot{u}(t) + K(T)u(t) = F_{\text{ext}}(t) + g(T) \quad (4.1)$$

where  $t$  is the time.  $\ddot{u}(t)$ ,  $\dot{u}(t)$ , and  $u(t)$  are the acceleration vector, velocity vector, and displacement vector, respectively.  $M$ ,  $C(T)$ ,  $K(T)$ ,  $F_{\text{ext}}(t)$ , and  $g(T)$  are the mass matrix, damping matrix, stiffness matrix, external mechanical load vector, and thermal load vector, respectively.  $T$  is the temperature, which is a function of the time and location of the FE nodes and varies throughout the simulation, as calculated in the thermal solver. Equation (4.1) indicates that the damping, stiffness, and thermal load of the model are temperature dependent. This ensures that the thermal effect can be included in the mechanical solver. An explicit time integration scheme [30] was adopted to solve the equation.

The governing equation of the thermal solver is presented in equation (4.2) [31, 32]:

$$\frac{\partial}{\partial x} \left( k_x \frac{\partial T}{\partial x} \right) + \frac{\partial}{\partial y} \left( k_y \frac{\partial T}{\partial y} \right) + \frac{\partial}{\partial z} \left( k_z \frac{\partial T}{\partial z} \right) + I(x, y, z, t) = \rho c \frac{\partial T}{\partial t} \quad (4.2)$$

where  $\rho$  is the density of the material, and  $c$  is the heat capacity.  $k_x$ ,  $k_y$ , and  $k_z$  represent the thermal conductivity in the  $x$ ,  $y$ , and  $z$  directions, and  $I(x, y, z, t)$  represents the internal heat generation rate per unit volume. An implicit method using a generalized trapezoidal time integration algorithm was employed to solve equation (4.2) with given initial and boundary conditions. Because wheel braking was simulated in this study and the wheel-rail interface had been heated due to the braking friction force, an initial temperature of 200 °C was used, i.e.,  $T_{(x,y,z)}^{t=0} = 200$  °C. The boundary condition of the thermal contact problem is given in equation (4.3) [31, 32] concerning the heat flux boundary equation (4.4).

$$k_x \frac{\partial T}{\partial x} n_x + k_y \frac{\partial T}{\partial y} n_y + k_z \frac{\partial T}{\partial z} n_z = Q \quad (4.3)$$

$$Q = \delta \mu v_s P(x, y) \quad (4.4)$$

where  $n_x$ ,  $n_y$ , and  $n_z$  are the normal vectors in the  $x$ ,  $y$ , and  $z$  directions.  $Q$  is the heat flux at the nodes due to friction, which relies on the calculations of wheel-rail contact in the mechanical solver.  $\delta$  is the heat partition to one contact body, and  $(1 - \delta)$  is thus the heat partition to the other contact body. In this model,  $\delta$  is assumed to be 0.5.  $\mu$  is the coefficient of friction, and  $v_s$  represents the relative sliding velocities of the nodes between the wheel and rail.  $P_{(x,y)}$  is the local surface contact pressure. The test was conducted indoors on a laboratory test rig with negligible airflow and a relatively low wheel speed, minimizing convective heat dissipation. Given that radiation and convection occur at a much slower rate compared to thermal conduction, these effects were neglected in the model, as heat primarily conducts into the rail and wheel within the 1.09 ms timeframe, making external heat dissipation mechanisms insignificant.

### 4.2.2. MEASUREMENT

In this section, the structure of the V-Track test rig is briefly introduced, and the temperature measurement methodology is described. The V-Track test rig is capable of reproducing real-life wheel-rail frictional rolling contact [33] and has been widely employed to investigate related problems [34]. As illustrated in Figure 4.2, the V-Track includes a ring track system and two wheel assemblies connected to a driving steel frame that rotates around a vertical axis centered on the ring track. The rails and cylinder wheels used in the V-Track were cut from real-life rail heads and wheel rims, respectively, to ensure identical thermal behavior. A more detailed description of the V-Track wheel assembly can be found in [26]. The angular velocities of the driving steel frame and the wheel axle were recorded by two separate encoders with a data acquisition rate of 16.67 kHz. Propelled by a motor through the driving steel frame, the wheel assemblies moved at a constant velocity of 16 km/h along the track in this study. The wheel angular velocity was initially controlled to approximately 68.4 rad/s. A braking torque was then applied to one V-Track wheel with another motor to generate the desired slip ratio from 2 to 35% and the wheel-rail longitudinal force. At the same time, the temperature field as close as possible to the contact patch was measured. Note that the applications of the braking torque effectively changed the wheel angular velocity but had a trivial influence on wheel assembly translation velocity, which was kept constant by the frame-driving motor. A 4000 N vertical (normal) wheel load, producing a maximum contact pressure of 1.01 GPa, which is similar to that in the field, was applied via the primary suspension of the wheel assembly (shown as two springs in Figure 4.2(b)). The angle of attack was designed to be as small as possible to minimize the wheel-rail lateral force. The wheel-rail contact forces were recorded via dynamometers [35] with a data acquisition rate of 16.67 kHz.

As shown in Figure 4.2(c), a ring track with a radius  $R$  of 2 m is mounted onto 100 uniformly distributed sleepers using fastenings. It consists of five rail sections made of different materials—B360, R370, R350 HT, and R260—that are connected through five rail joints, i.e., J1 ~ J5. The rails have identical profiles, featuring a head curvature radius of 60 mm.

Figure 4.3 shows a close-up view of the installation of the thermal camera used to measure the contact temperature in the V-Track. To capture the temperature field as close as possible to the contact patch, a high-speed infrared thermal imaging camera (FLIR X6900sc) was securely mounted on a customized steel frame on the trailing side of the wheel. Moving in synchronization with the wheel assembly, the camera focused on the running band just behind the wheel-rail contact area, enabling the measurement of contact temperature immediately after wheel passage. The thermal camera was connected to a remote-controlled laptop, as shown in Figure 4.2(a), for data acquisition. The temperature data were recorded with a sampling frequency of 1 kHz for more than 20 s, during which the wheel assembly ran seven cycles along the track. The measured temperatures, ranging from 250 to 670 °C, were predetermined on the basis of the FE simulation results. The calibrated emissivity value for the rail surface is 0.83 (with a standard deviation of 4%).

To target the camera as close as possible to the wheel-rail contact area, a small projection angle  $\theta$ , i.e., the angle between the projection line of the camera and a horizon-

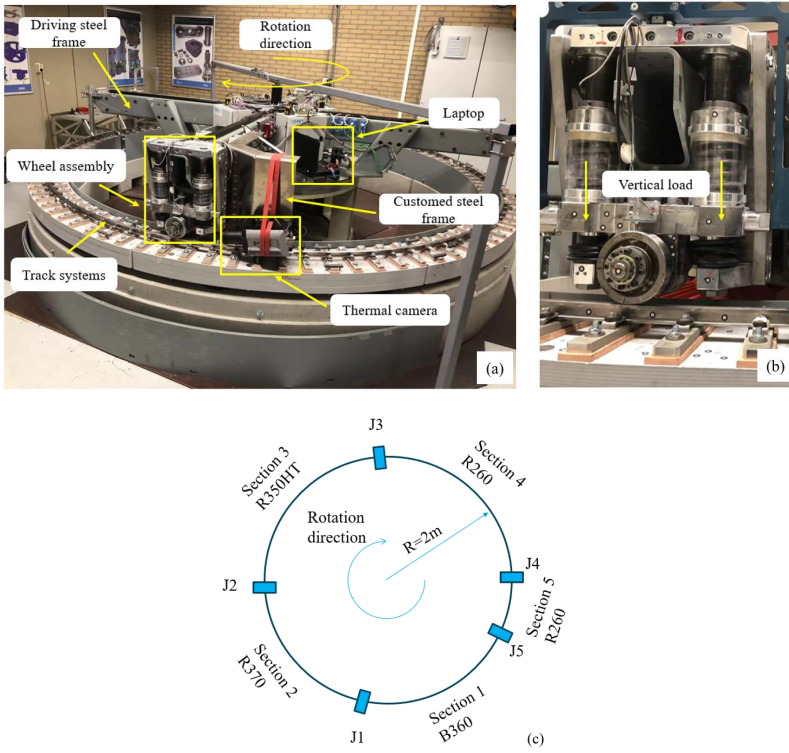


Figure 4.2: The V-track test rig. (a) The components of V-Track; (b) a wheel assembly; and (c) a schematic drawing of the rail section distribution.

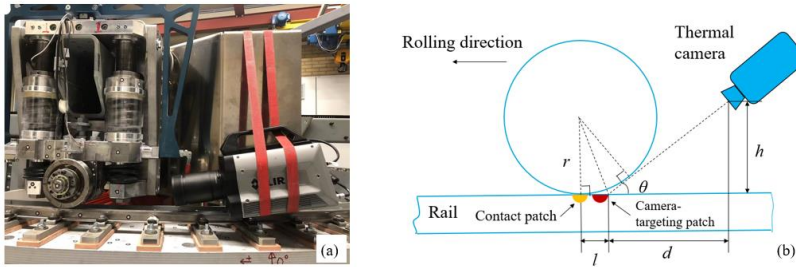


Figure 4.3: The installation and position of the thermal camera. (a) Screw the camera on a customized steel frame; (b) camera-targeting patch.

tal line (shown in Figure 4.3(b)), is desired. Moreover, to avoid possible collisions between the camera and the rail, a safe distance from the lens to the rail top is needed, which results in an angle of  $\theta = 11^\circ$  in this study. The distance from the trailing edge of the camera-targeting patch (denoted by the red solid semicircle in Figure 4.3(b)) to the

wheel-rail contact patch (denoted by the yellow solid semicircle) can be calculated via equation (4.5):

$$l = r \cdot \tan \left( \frac{\arctan \left( \frac{h}{d} \right)}{2} \right) \quad (4.5)$$

where  $l$  is the distance from the camera-targeting position to the center of the wheel-rail contact patch,  $r$  is the wheel radius, which equals 65 mm,  $h$  denotes the distance from the lens center to the rail top surface, approximately 5.5 mm, and  $d$  is the longitudinal distance between the lens center and the camera-targeting position, which is 28.5 mm. The value of  $l$ , which is equal to 6.25 mm, can be calculated via equation (4.5). We use  $2a$  to denote the longitudinal length of the contact patch. By dividing  $(l - a)$  by the translational wheel speed of 16 km/h, a time lag of the temperature measurement after wheel-rail contact can be obtained, which is 1.09 ms. The simulated contact temperatures after 1.09 ms were thus compared to the measured rail surface temperatures, which will be presented in Section 4.3.3.

4

#### 4.2.3. SLIP RATIO CALCULATION

The slip ratio is defined as the difference between the translational velocity and the circumferential velocity of the wheel divided by its translational velocity. As mentioned before, two encoders installed in the test rig were applied to record the angular velocity of the driving steel frame  $\omega_d$  and the wheel axle  $\omega$ . The translational velocity of the wheel assembly  $V_p$  can then be obtained on the basis of the driving steel frame velocity  $\omega_d$  and ring track radius  $R$  according to equation (4.6):

$$V_p = \omega_d \times R \quad (4.6)$$

However, when equation (4.6) was used to calculate the wheel translation velocity  $V_p$ , a sine-wave pattern was observed over the angular position (location as an angle measured from a fixed reference point) along one ring-track circle, as shown by the black curve in Figure 4.4. This was a measurement error induced by a slight misalignment between the encoder center and the rotational center of the driving steel frame. The measurement error exceeded 10%, with an average value of 16 km/h and a maximum value of over 18 km/h, which is unacceptable for the next-step slip ratio estimation, where high-precision velocity measurements are needed.

An alternative method to calculate the wheel translation velocity was thus proposed, as defined in equation (4.7):

$$V_p = \omega_{w0} \times r \quad (4.7)$$

where  $\omega_{w0}$  is the angular velocity of the wheel under free rolling contact conditions: a nominal zero longitudinal wheel-rail friction force was achieved by applying a small positive torque to the wheel axle to overcome the negative torque induced by mechanical friction, e.g., from the gearbox. In wheel-rail free rolling contact, the slip ratio is also zero, i.e., the wheel translation velocity equals the wheel circumferential velocity, because the wheel-rail friction force is zero. The measured translation velocity obtained with this alternative method is also presented in Figure 4.4, which presents a steady trend along the track circle. Consequently, the measured slip ratio can be calculated via equation (4.8):

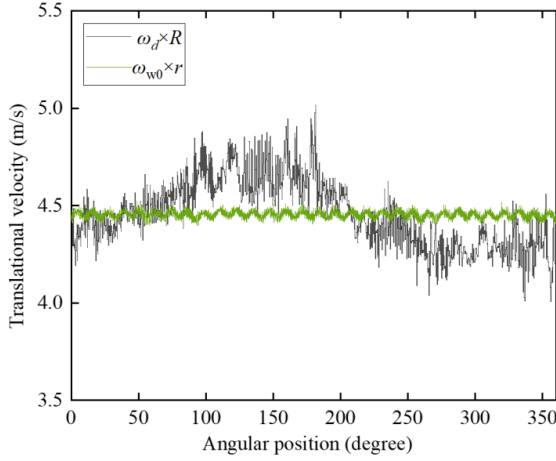


Figure 4.4: Two methods to obtain the translational velocity of the wheel assembly during the measurement.

$$S = \frac{V_p - \omega r}{V_p} = \frac{\omega_{w0} - \omega}{\omega_{w0}} \times 100\% \quad (4.8)$$

where  $S$  denotes the slip ratio,  $V_p$  is the wheel translation velocity, and  $\omega$  is the wheel angular velocity.

## 4.3. RESULTS

### 4.3.1. MEASUREMENT DATA PROCESSING

A regression analysis was conducted in this study to correlate the measured slip ratio and the temperature during braking. However, because the wheel velocities (and thus the slip ratio calculated on the basis of wheel velocities via equation (4.8)) and temperature data were measured separately, each using separate timing systems, data synchronization was required to conduct the regression analysis accurately. Fig. 4.5 presents the measured temperature data and the synchronized slip ratio during a wheel braking process. The synchronization method is described below. In Fig. 4.5, the temperature data points at each instance represent the measured peak temperature within the camera-targeting patch, as presented in Fig. 4.3(b). The labels S1 ~ S5 and J1 ~ J5 correspond to the rail sections and joints depicted in Fig. 4.2(c). The moments at which the wheel passes the joints are denoted by the vertical pink dashed lines and were determined from the angular positions along the track that were recorded together with the wheel velocities. As illustrated in Fig. 4.5, the wheel travelled in a braking manner from the rail section 1 (S1) to section 4 (S4) between 4.45 s and 7.2 s. Subsequently, after passing Joint 5 (J5) at 7.25 s, the wheel returned to S1 for the next cycle. Throughout the wheel braking process from 4.45 s to 8 s, the temperature increased from 250 °C to 670 °C. Note that the temperature data beyond the predefined measurement range, i.e., from 250 °C to 670 °C, were truncated in the measurement. In the subsequent regression analysis, this trun-

cated data was excluded to ensure accuracy. Correspondingly, the slip ratio, which was calculated via equation (4.8), increased from approximately 2% to 35%.

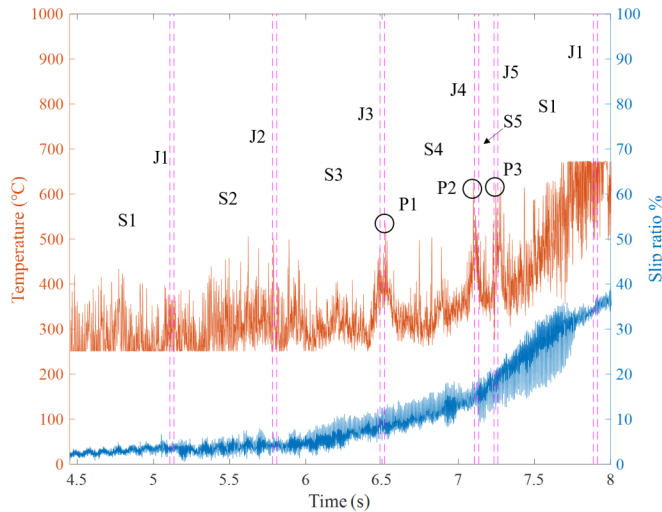


Figure 4.5: The maximum temperature within the camera-targeting patch and the slip ratio.

The maximum temperature within the camera-targeting patch and the slip ratio were initially synchronized by shifting the data so that they corresponded at the joints and then assessed with a frequency domain analysis for fine-tuning. The locations of the joints (pink lines) were known for the slip ratio measurement (blue curve) because it was measured together with the wheel angular position along the ring-track circle. The locations of each joint are indicated with two pink vertical lines, one for entry and the other for exit of the joint. In the temperature measurement (orange curve), peaks (P1, P2, and P3 in Figure 4.5) were identified at joints of poor quality because such joints have a locally reduced wheel-rail contact area and thus increased contact pressure, increasing the temperature. These joints were J3, J4 and J5. The temperature curve was shifted so that J3, J4 and J5 matched their locations in the slip ratio curve, and the two curves were roughly synchronized.

To obtain more accurate synchronization, a frequency-domain analysis was performed. A power spectral density (PSD) analysis of the measured temperature and slip ratio at S3 is shown in Figure 4.6. Both the PSDs of the slip ratio and temperature data exhibit a dominant frequency at 118.5 Hz, denoted by the vertical black dashed line in Figure 4.6. This frequency corresponds to the P2 resonance of the wheel-rail system in the V-Track [36] and indicates a notable correlation between the measured temperature data and the slip ratio data. The temperature and slip ratio data were then filtered with passband frequencies of 118 ~ 119 Hz. The filtered results before synchronization are displayed in Figure 4.7(a).

A correlation analysis was then used to synchronize the measured slip ratio and the temperature by calculating their correlation coefficients  $P$  [37] across various time shifts to find the best alignment.  $P$  quantifies the linear relationship between two variables,

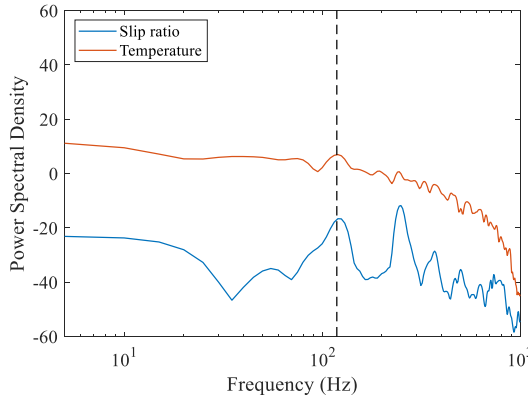


Figure 4.6: The PSD analysis of the measured slip ratio and temperature of S3.

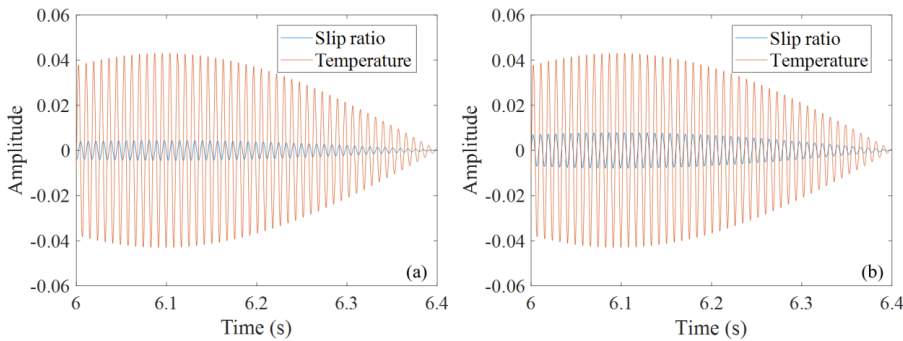


Figure 4.7: The bandpass (118 Hz to 119 Hz) filtered data of the measured temperature and slip ratio. (a) Before the frequency-domain synchronization; (b) after the frequency-domain synchronization.

ranging from  $-1$  (fully negative) to  $+1$  (fully positive). Before the frequency-domain synchronization,  $P$  was  $-0.13$ , i.e., the case in Figure 4.7(a). The measured slip ratio was then incrementally shifted, and the correlation was calculated at each step until  $P$  achieved  $0.98$ , as shown in Figure 4.7(b), indicating that the two signals were well synchronized.

#### 4.3.2. REGRESSION ANALYSIS

The analytical model presented in [11] indicates a linear correlation between the slip ratio and the maximum contact temperature when the contact pressure and thermal parameters are constant. Although the temperature measured in this study was not the maximum temperature within the contact patch, but the temperature field immediately behind the contact patch, given the absence of a known relationship, a linear regression analysis was employed to process the measurement data. Future research can be conducted to further characterize this relationship. Based on the linear regression analysis, the correspondence between the measured slip ratio and temperature was obtained via equation (4.9):

$$T = 8.36 \times S + 260 \quad (4.9)$$

where  $S$  and  $T$  are the measured slip ratio and temperature ( $^{\circ}\text{C}$ ), respectively. The coefficient of determination,  $R^2$ , was calculated to be 0.72, indicating that approximately 72% of the variability in the dependent variable  $T$  can be explained by the independent variable  $S$  in the regression equation (4.9). The temperature  $T$  measured from 5.8 s to 7.7 s (mostly ranging between  $250^{\circ}\text{C}$  and  $670^{\circ}\text{C}$ ) as a function of the slip ratio  $S$ , as well as the derived linear regression fitting, are plotted in Figure 4.8. The regression equation performs well in fitting the data; therefore, the wheel-rail contact temperatures can be estimated on the basis of this regression equation with input slip ratios. The remaining 28% of the variability that cannot be explained by the linear regression relationship may be due to the contact pressure varying over time in real-life wheel-rail rolling [38], and the thermal parameters could need to be further calibrated.

4

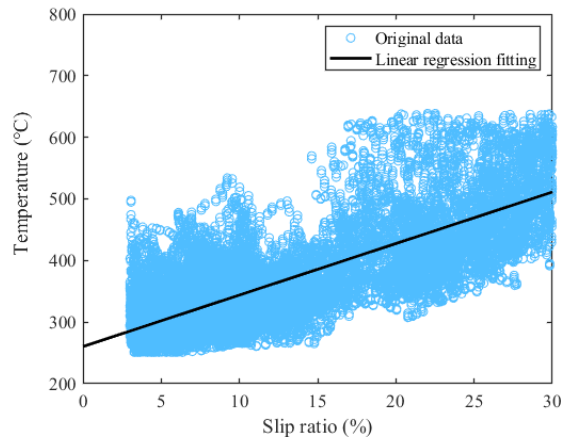


Figure 4.8: A linear regression analysis of the measured slip ratio and temperature.

### 4.3.3. MODEL VALIDATION

#### 4.3.3.1 SIMULATION CASES AND RESULTS

The previous section demonstrated the linear correlation between the wheel-rail contact temperature and slip ratio and the possibility of predicting the contact temperature on the basis of the slip ratio. Three slip ratio scenarios—5%, 10%, and 15%—were then simulated via the FE method presented in Section 4.2.1. In the measurement, we measured the wheel-rail contact temperatures under continuous variation of the slip ratio from low to high along the track with four different rail grades used in the V-Track test rig, as shown in Figure 4.2(c). The 5% and 10% slip ratio scenarios took place with the rail grade R350HT, and the 15% slip ratio scenarios occurred with the rail grade R260. To ensure consistency with the experimental conditions, two distinct sets of temperature-dependent material parameters widely used in wheel-rail thermomechanical behavior modeling were incorporated into the material modeling. The two material parameter

sets, with one set detailed in Tables 4.1 and 4.2 and the other in Table 4.3, result in a total of six simulation cases, as summarized in Table 4.4. The material parameters provided in Table 4.1 and Table 4.3 also illustrate that the same rail type may have different mechanical material parameters at different temperatures, especially the yield strength. The simulated contact temperature on the rail along the rolling direction for case 5 (slip ratio = 10% and rail grade R350HT) at 2.7 ms is plotted against the simulated wheel-rail contact pressure in Figure 4.9(a).

Table 4.4: The simulation cases of the FE model

Material type	Slip ratio and Rail grade		
Material set of rail (parameters in Tables 1&2)	5%, R350HT (case 1)	10%, R350HT (case 2)	15%, R260 (case 3)
Material set of rail (parameters in Table 3)	5%, R350HT (case 4)	10%, R350HT (case 5)	15%, R260 (case 6)

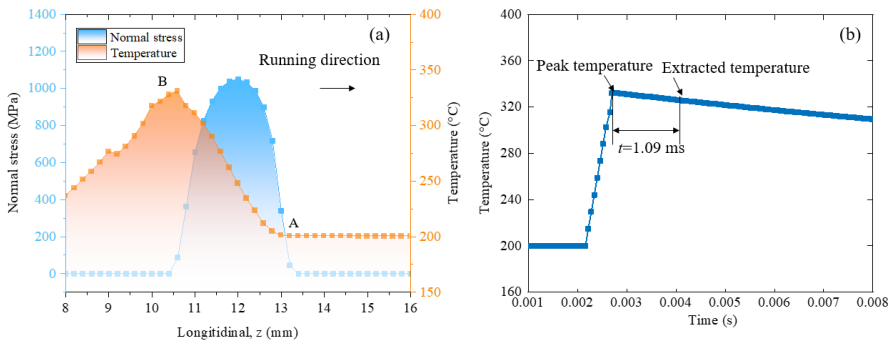


Figure 4.9: Numerical solution within the contact patch of case 5 at 2.7 ms. (a) Temperature field and the contact pressure on the rail surface; (b) the temperature change over time of the node corresponding to the peak temperature within the contact patch.

As shown in Figure 4.9(a), the maximum wheel-rail contact pressure during the simulation is 1048 MPa. The peak temperature is 330 °C and occurs at the trailing edge B of the contact patch, whereas the minimum temperature is found at the leading edge A, which is consistent with the findings reported in [11, 39]. A gradual increase in contact temperature is observed from the leading area to the trailing area. This is because the wheel and rail materials, with their ‘initial temperatures’ accumulated in the previous contact cycles, flow into the contact patch from the leading edge, and the contact-induced heat is accumulated during wheel-rail friction rolling until the materials exit the contact patch at the trailing edge.

The temperature-time history of the trailing-edge node in the middle of the contact patch is presented in Figure 4.9(b). As mentioned in Section 4.2.2, the infrared camera employed in this study captured the flash temperatures on the rail head after 1.09 ms of

wheel passage; the simulated temperatures were thus extracted 1.09 ms after wheel passage, i.e., 1.09 ms after the peak temperature occurred at the trailing edge of the wheel-rail contact patch, as indicated in Figure 4.9(b).

Figure 4.10 shows the time histories of the temperature and slip ratio simulated with case 5 (slip ratio = 10% and rail grade R350HT). As shown in Figure 4.10, the simulated slip ratio, calculated via the method presented in [40], fluctuates between 9% and 11%, with an average value of 10%, aligning with the initial setting of simulation case 5. In addition, the simulated temperature also varies with time, with an average temperature of 317 °C and a fluctuation margin of 4%. This average temperature was then taken as the simulation result to compare with the measured temperature under the same slip ratio conditions. The fluctuations in the simulated slip ratio and temperature should be attributed to the dynamic interactions between the wheel and rail, during which the contact stress and wheel motion vary with time [38].

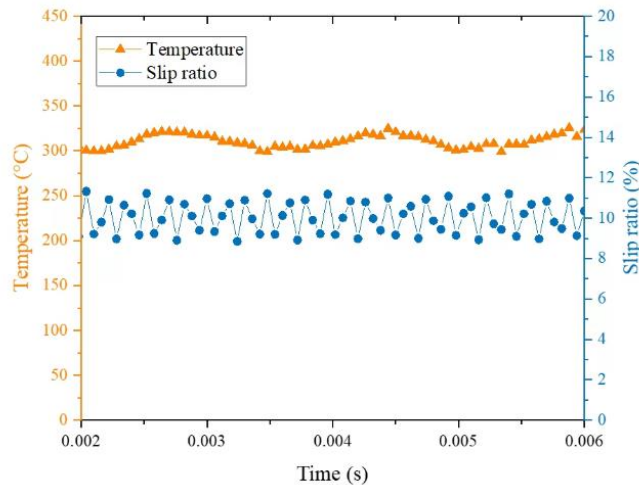


Figure 4.10: The time histories of the simulated contact temperature and slip ratio.

#### 4.3.3.2 COMPARISON WITH MEASUREMENT

Figure 4.11 presents a comparison between the simulated temperatures and the measured temperatures with three different slip ratios and two sets of material parameters. The measured temperatures at different slip ratios were obtained via equation (4.9). The simulation results for all six cases were obtained as described in Section 4.3.3.1.

As shown in Figure 4.11, the measured and simulated temperatures exhibit the same increasing pattern as the slip ratio increases from 5% to 10% and then to 15%. The measured contact temperatures are 302 °C, 343 °C, and 385 °C for slip ratios of 5%, 10%, and 15%, respectively. When the material sets from Tables 4.1 and 4.2 are used, the simulated temperatures for slip ratios of 5%, 10%, and 15% are 278 °C, 310 °C, and 347 °C, respectively, which are slightly lower than those simulated using the material set from Table 4.3: 282 °C, 317 °C, and 360 °C. Since the simulated results obtained with the two parameter

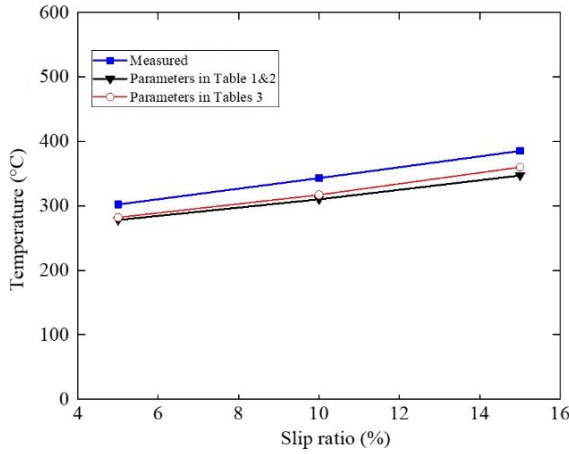


Figure 4.11: The comparison of the measured and simulated temperature with different slip ratios.

sets are close to each other and in reasonable agreement with the measurement results, a conclusion can be drawn that both parameter sets can represent the thermomechanical material properties of rail steels when the temperature is below 360 °C.

The maximum relative errors for the cases with the three slip ratios are 7.9%, 9.6%, and 9.9%. The discrepancy increases with the slip ratio and may be because the initial temperature (200 °C) assumed in the simulations for all three slip ratio cases is lower than that under actual conditions. In particular, for the higher slip ratio case (15%), a higher residual temperature, and thus initial temperature, can accumulate from previous wheel-rail contact cycles. Future work should measure the flash temperature of wheel and rail surfaces immediately before they come into contact, e.g., using an infrared camera targeting the front side of the wheel-rail interface and then providing a more accurate input of initial temperature to the simulation.

#### 4.4. CONCLUSIONS, DISCUSSION, AND FUTURE WORK

In this study, a thermomechanical finite element (FE) model for simulating wheel and rail interactions during braking was developed with two different temperature-dependent mechanical and thermal material parameter sets. This model was experimentally validated up to approximately 360 °C for the first time on the TU-Delft V-Track test rig under the same contact conditions in terms of the contact pressure, slip ratio and coefficient of friction. After processing the measurement data, including the calculation of the slip ratio and data synchronization, a regression analysis was conducted between the measured contact temperature and slip ratio. Comparisons were then made between the measured and simulated contact temperatures under three high slip ratio scenarios. The following conclusions and insights from the discussion are derived from this study:

- The contact temperatures simulated with the developed thermomechanical FE

model achieve reasonable agreement with the experimental results across slip ratios of 5%, 10% and 15% in terms of the values and variation trends. The maximum error between the simulations and measurements is within 9.9% up to 360 °C, which is acceptable for engineering applications.

- The match of the simulated and measured contact temperatures suggests that the proposed model is accurate for simulating wheel-rail contact with thermal effects and that the employed temperature-dependent parameters are reliable for representing the thermomechanical properties of rail materials.
- A linear relationship was identified between the measured slip ratio and contact temperature. 72% of the variability in the measured temperature can be explained by the slip ratio in the linear regression equation. The remaining 28% of the variability that cannot be explained linearly may be due to the contact pressure varying over time during real-life wheel-rail rolling.

The maximum contact temperature is of the most concern in the previous research as it significantly influences contact behavior and the subsequent interface deterioration. In this study, for the experimental validation of the FE thermomechanical model with high slip ratios, which has rarely been addressed in previous research, the contact temperature was measured at a 1.09 ms lag behind the contact patch. The validated FE model then enables the computation of temperature distributions across the contact patch, including the maximum contact temperature. These findings support the reliability of the proposed modeling approach and provide a basis for further investigations into the thermal effects of wheel-rail interactions under high slip conditions.

To further improve the accuracy of the thermomechanical model, more accurate input of the initial temperature of the contact bodies is desirable. In addition, it can be helpful to consider the thermal radiation and convection to the air and the temperature-dependent coefficients of friction. Finally, the thermomechanical model should be better able to account for the contact profile alterations during wheel contact since severe wear can be induced by high slip ratios and elevated temperatures.

# BIBLIOGRAPHY

- [1] A. Ekberg and E. Kabo. “Fatigue of railway wheels and rails under rolling contact and thermal loading—an overview”. In: *Wear* 258 (2005), pp. 1288–1300. DOI: [10.1016/j.wear.2004.03.039](https://doi.org/10.1016/j.wear.2004.03.039).
- [2] J.P. Srivastava, P.K. Sarkar, and V. Ranjan. “Effects of thermal load on wheel–rail contacts: A review”. In: *Journal of Thermal Stresses* 39 (2016), pp. 1389–1418. DOI: [10.1080/01495739.2016.1216060](https://doi.org/10.1080/01495739.2016.1216060).
- [3] A.M.S. Asih, K. Ding, and A. Kapoor. “Modelling rail wear transition and mechanism due to frictional heating”. In: *Wear* 284-285 (2012), pp. 82–90. DOI: [10.1016/j.wear.2012.02.017](https://doi.org/10.1016/j.wear.2012.02.017).
- [4] J. Ahlström and B.J.W. Karlsson. “Analytical 1D model for analysis of the thermally affected zone formed during railway wheel skid”. In: *Proceedings of the Institution of Mechanical Engineers, Part F: Journal of Rail and Rapid Transit* 232 (1999), pp. 15–24.
- [5] M. Ertz and K. Knothe. “Thermal stresses and shakedown in wheel/rail contact”. In: *Archive of Applied Mechanics* 72 (2003), pp. 715–729. DOI: [10.1007/s00419-002-0255-4](https://doi.org/10.1007/s00419-002-0255-4).
- [6] C. Bernsteiner et al. “Development of white etching layers on rails: Simulations and experiments”. In: *Wear* 366-367 (2016), pp. 116–122. DOI: [10.1016/j.wear.2016.03.028](https://doi.org/10.1016/j.wear.2016.03.028).
- [7] J. Jergéus et al. “Full-scale railway wheel flat experiments”. In: *Proceedings of the Institution of Mechanical Engineers, Part F: Journal of Rail and Rapid Transit* 213 (1999), pp. 1–13. DOI: [10.1243/0954409991530985](https://doi.org/10.1243/0954409991530985).
- [8] Q. Lian et al. “Thermo-mechanical coupled finite element analysis of rolling contact fatigue and wear properties of a rail steel under different slip ratios”. In: *Tribology International* 141 (2020), p. 105943. DOI: [10.1016/j.triboint.2019.105943](https://doi.org/10.1016/j.triboint.2019.105943).
- [9] J. Jaeger. “Moving sources of heat and temperature at sliding contacts”. In: *Proceedings of the Royal Society of New South Wales* 1942 (), p. 222.
- [10] H. Blok. “The flash temperature concept”. In: *Wear* 6 (1963), pp. 483–494. DOI: [10.1016/0043-1648\(63\)90283-7](https://doi.org/10.1016/0043-1648(63)90283-7).
- [11] K. Knothe and S.J.W. Liebelt. “Determination of temperatures for sliding contact with applications for wheel-rail systems”. In: *Wear* 189 (1995), pp. 91–99. DOI: [10.1016/0043-1648\(95\)06666-7](https://doi.org/10.1016/0043-1648(95)06666-7).

- [12] R. Lewis and R. Dwyer-Joyce. “Wear mechanisms and transitions in railway wheel steels”. In: *Proceedings of the Institution of Mechanical Engineers, Part J: Journal of Engineering Tribology* 218 (2004), pp. 467–478. DOI: [10.1243/1350650042794815](https://doi.org/10.1243/1350650042794815).
- [13] A. Olver. “Testing transmission lubricants: the importance of thermal response”. In: *Proceedings of the Institution of Mechanical Engineers, Part G: Journal of Aerospace Engineering* 205 (1991), pp. 35–44. DOI: [10.1243/PIME\\_PROC\\_1991\\_205\\_235\\_0](https://doi.org/10.1243/PIME_PROC_1991_205_235_0).
- [14] M. Naeimi et al. “Thermomechanical analysis of the wheel-rail contact using a coupled modelling procedure”. In: *Tribology International* 117 (2018), pp. 250–260. DOI: [10.1016/j.triboint.2017.09.010](https://doi.org/10.1016/j.triboint.2017.09.010).
- [15] K. Vo et al. “The influence of high temperature due to high adhesion condition on rail damage”. In: *Wear* 330 (2015), pp. 571–580. DOI: [10.1016/j.wear.2015.01.059](https://doi.org/10.1016/j.wear.2015.01.059).
- [16] J. Goldak, A. Chakravarti, and M. Bibby. “A new finite element model for welding heat sources”. In: *Metallurgical Transactions B* 15 (1984), pp. 299–305. DOI: [10.1007/BF02667333](https://doi.org/10.1007/BF02667333).
- [17] E.A. Gallardo-Hernandez, R. Lewis, and R.S. Dwyer-Joyce. “Temperature in a twin-disc wheel/rail contact simulation”. In: *Tribology International* 39 (2006), pp. 1653–1663. DOI: [10.1016/j.triboint.2006.01.028](https://doi.org/10.1016/j.triboint.2006.01.028).
- [18] M. Petereson. “Two-dimensional finite element simulation of the thermal problem at railway block braking”. In: *Proceedings of the Institution of Mechanical Engineers, Part C: Journal of Mechanical Engineering Science* 216 (2002), pp. 259–273. DOI: [10.1243/0954406021524945](https://doi.org/10.1243/0954406021524945).
- [19] T. Vernersson. “Temperatures at railway tread braking. Part 1: modelling”. In: *Proceedings of the Institution of Mechanical Engineers, Part F: Journal of Rail and Rapid Transit* 221 (2007), pp. 167–182. DOI: [10.1243/0954409JRRT57](https://doi.org/10.1243/0954409JRRT57).
- [20] T. Vernersson and R. Lundén. “Temperatures at railway tread braking. Part 3: wheel and block temperatures and the influence of rail chill”. In: *Proceedings of the Institution of Mechanical Engineers, Part F: Journal of Rail and Rapid Transit* 221 (2007), pp. 443–454. DOI: [10.1243/09544097JRRT91](https://doi.org/10.1243/09544097JRRT91).
- [21] P. Baranowski et al. “Thermovision in the validation process of numerical simulation of braking”. In: *Metrology and Measurement Systems* 21 (2014), pp. 329–340. DOI: [10.2478/mms-2014-0028](https://doi.org/10.2478/mms-2014-0028).
- [22] Y.C. Chen and S.Y. Lee. “Elastic-plastic wheel-rail thermal contact on corrugated rails during wheel braking”. In: *ASME Journal of Tribology* 131 (2009), p. 011401. DOI: [10.1115/1.2991163](https://doi.org/10.1115/1.2991163).
- [23] L. Wu et al. “Thermo-elastic-plastic finite element analysis of wheel/rail sliding contact”. In: *Wear* 271 (2011), pp. 437–443. DOI: [10.1016/j.wear.2010.10.034](https://doi.org/10.1016/j.wear.2010.10.034).

- [24] Y. Wei, Y. Wu, and Z. Chen. “An experimental measurement and numerical calculation method on friction temperature rise of sliding contact pairs - taking rail/wheel contact as an example”. In: *Journal of Measurements in Engineering* 11 (2023), pp. 1–11. DOI: [10.21595/jme.2023.22974](https://doi.org/10.21595/jme.2023.22974).
- [25] B. Talamini, J. Gordon, and A.B. Perlman. “Investigation of the effects of sliding on wheel tread damage”. In: *ASME International Mechanical Engineering Congress and Exposition*. 2005, pp. 119–125.
- [26] M. Naeimi et al. “Development of a new downscale setup for wheel-rail contact experiments under impact loading conditions”. In: *Experimental Techniques* 42 (2017), pp. 1–17. DOI: [10.1007/s40799-017-0216-z](https://doi.org/10.1007/s40799-017-0216-z).
- [27] X. Zhao and Z. Li. “The solution of frictional wheel–rail rolling contact with a 3D transient finite element model: Validation and error analysis”. In: *Wear* 271 (2011), pp. 444–452. DOI: [10.1016/j.wear.2010.10.007](https://doi.org/10.1016/j.wear.2010.10.007).
- [28] S. Jain and P. Tiso. “Model order reduction for temperature-dependent nonlinear mechanical systems: A multiple scales approach”. In: *Journal of Sound and Vibration* 465 (2020). DOI: [10.1016/j.jsv.2019.115022](https://doi.org/10.1016/j.jsv.2019.115022).
- [29] T.R. Hsu. *The finite element method in thermomechanics*. Springer Science & Business Media, 2012.
- [30] Z. Yang, X. Deng, and Z. Li. “Numerical modeling of dynamic frictional rolling contact with an explicit finite element method”. In: *Tribology International* 129 (2019), pp. 214–231. DOI: [10.1016/j.triboint.2018.08.028](https://doi.org/10.1016/j.triboint.2018.08.028).
- [31] O.H. John. *LS-DYNA theory manual*. Livermore Software Technology Corporation, 2006.
- [32] M.N. Özışık. *Heat Conduction*. Wiley, 1980.
- [33] Z. Yang et al. “An experimental study on the effects of friction modifiers on wheel–rail dynamic interactions with various angles of attack”. In: *Railway Engineering Science* 30 (2022), pp. 360–382. DOI: [10.1007/s40534-022-00285-y](https://doi.org/10.1007/s40534-022-00285-y).
- [34] P. Zhang and Z. Li. “New experimental evidences of corrugation formation due to rail longitudinal vibration mode”. In: *International Journal of Rail Transportation* (2024). DOI: [10.1080/23248378.2024.2336503](https://doi.org/10.1080/23248378.2024.2336503).
- [35] P. Zhang, J. Moraal, and Z.J.M. Li. “Design, calibration and validation of a wheel-rail contact force measurement system in V-Track”. In: *Measurement* 175 (2021), p. 109105.
- [36] P. Zhang et al. “Comprehensive validation of three-dimensional finite element modelling of wheel-rail high-frequency interaction via the V-Track test rig”. In: *Vehicle System Dynamics* (2024). DOI: [10.1080/00423114.2024.2304626](https://doi.org/10.1080/00423114.2024.2304626).
- [37] K. Pearson. “On the criterion that a given system of deviations from the probable in the case of a correlated system of variables is such that it can be reasonably supposed to have arisen from random sampling”. In: *The London, Edinburgh, and Dublin Philosophical Magazine and Journal of Science* 50 (1900), pp. 157–175. DOI: [10.1080/14786440009463897](https://doi.org/10.1080/14786440009463897).

- [38] Z. Yang and Z. Li. “Numerical modeling of wheel-rail squeal-exciting contact”. In: *International Journal of Mechanical Sciences* 153-154 (2019), pp. 490–499. DOI: [10.1016/j.ijmecsci.2019.02.012](https://doi.org/10.1016/j.ijmecsci.2019.02.012).
- [39] H. Alizadeh Otorabad et al. “Modeling temperature evolution of wheel flat during formation”. In: *International Journal of Thermal Sciences* 140 (2019), pp. 114–126. DOI: [10.1016/j.ijthermalsci.2019.02.040](https://doi.org/10.1016/j.ijthermalsci.2019.02.040).
- [40] X. Zhao et al. “A study on high-speed rolling contact between a wheel and a contaminated rail”. In: *Vehicle System Dynamics* 52 (2014), pp. 1270–1287. DOI: [10.1080/00423114.2014.934845](https://doi.org/10.1080/00423114.2014.934845).

# 5

## CONCLUSIONS AND FUTURE WORK

## 5.1. CONCLUSIONS

This PhD research aimed to improve the understanding of the thermomechanical behavior of the wheel-rail system, which is vital for enhancing the safety, reliability, and economic efficiency of railway operations. The study focused on developing a comprehensive thermomechanical wheel-rail contact model, validating its accuracy, and applying the model to analyze thermal contact-induced damages observed in the railway practice. The three research objectives presented in Chapter 1 have been addressed accordingly, and the conclusions can be drawn as follows.

**Objective 1:** Establish numerical models and experimental setups to accurately assess the thermomechanical behavior of the wheel-rail contact system.

- A 3D thermomechanical FE wheel-rail contact model was built. The numerical simulations reveal that within a contact patch, the contact temperature increases from the leading area to the trailing area because cool materials enter the contact patch from the leading area and are then heated up during frictional rolling.
- The normal contact stress simulated with the thermomechanical model is higher than the pure mechanical solution involving plasticity due to the thermal softening and thermal expansion/contraction stress, especially at locations after the crest of the polygonal profile, where the contact temperature is high. The wheel-rail impact contact stress can thus be underestimated without considering thermal effects.
- The material model influences wear depth calculation. The peaks of wear depth can be significantly overestimated when an elastic model is used. The consideration of thermal effects increases the peaks of wear depth, especially when the contact temperature is high.
- The developed measurement system, i.e., the V-Track test rig equipped with an on-board high-precision infrared camera, can reliably and continuously measure the wheel-rail contact temperatures up to 1200 °C, as well as transient thermal phenomena such as the cooling process.
- The V-Track rail emissivity, as an input parameter of the infrared thermal camera, is calibrated with values of 0.83 at 600 °C and 0.43 at 950 °C. It is also found that emissivity is insensitive to rail grades.

**Objective 2:** Reliably validate the thermomechanical contact model by accurately measuring the wheel-rail contact temperature, especially under high slip ratio conditions.

- The measured wheel-rail contact temperature rises with the slip ratio until a “wheel flat” is formed. The contact temperature drops when the “wheel flat” flows outside the contact area and then increases again with the slip ratio. The contact temperature may reach up to 1000 °C with a slip ratio of 99%.
- A linear relationship is identified between the measured slip ratio (2% ~ 30%) and contact temperature (277 °C ~ 511 °C) before the occurrence of a “wheel flat”. 72% of the variability in the measured temperature can be explained by the slip ratio

in the linear regression equation, and the remaining 28% of the variability may be due to the fact that the contact pressure varies over time in the real-life wheel-rail rolling, and the thermal parameters are temperature-dependent.

- The contact temperatures simulated with the developed thermomechanical FE model using two temperature-dependent mechanical and thermal material parameter sets demonstrate close similarity, and they are reasonably aligned with the experimental results across the slip ratios of 5%, 10%, and 15%. The simulated temperatures are about 8% ~ 10% lower than the experimental values. This suggests that the presented model is reliable for simulating wheel-rail contact with thermal effects and both the parameter sets can reflect the thermomechanical properties of the rail materials.

**Objective 3:** Improve the understanding of the generation and development of thermal damage, e.g., polygonal wear and a “wheel flat”.

- The contact temperature presents a periodic pattern along with the polygonal profile: the temperature is low at the locations just after the wheel profile trough and it goes up gradually and reaches the highest amplitude before decreasing slightly near the next trough. The simulated peak contact temperature at the three waves along the polygonal profile are 362 °C, 315 °C, and 275 °C, respectively.
- The simulated wear depth peaks increase with the initial polygonal wear amplitude, suggesting that with the increase of wear amplitudes, the development of polygonization is accelerated.
- A “wheel flat” is generated in the V-Track test when the slip ratio reaches around 40% and the corresponding wheel-rail contact temperature is 624 °C. By tracing the measured temperature drop of the “wheel flat” area over time, a wheel-rail contact temperature-evolution curve is obtained, which can be well-fitted with an exponential curve.

## 5.2. FUTURE WORK

To further improve the understanding of the thermomechanical behavior of the wheel-rail system, future research is recommended as follows.

- To improve the accuracy of the thermomechanical finite element (FE) model, it is desirable to accurately measure the initial temperatures of the contact bodies and use these values as initial conditions of simulations. For instance, another infrared camera can be mounted on the front side of the V-Track wheel assembly to measure the temperatures of the wheel and rail surfaces before they flow into the contact area.
- As the temperature changes, the frictional behavior of the wheel/rail materials may vary due to alterations in their physical and chemical properties. Consequently, the coefficients of friction can be affected. Using temperature-dependent

coefficients of friction can provide a more accurate representation of the interaction between contact bodies in the modeling. Incorporating these variable coefficients into future thermomechanical FE models will allow for more realistic simulations, reflecting how frictional forces might change under different thermal conditions.

- The temperature-dependent variation in material hardness should be incorporated into wear calculations to enhance the accuracy of wear predictions. While the present study neglects the thermal effects and the influence of plastic deformation on hardness in the wear simulation, it is important to recognize that within the studied temperature range, the yield stress is highly dependent on temperature, and material hardness is related to yield stress. Addressing this limitation in future research will allow for a more precise evaluation of wear behavior under varying thermal conditions.
- While the Jendel wear map and wear coefficient ( $k$ ) were utilized in this study, their limitations, including the use of a limited number of data points and material-specific nature, are acknowledged. To improve the accuracy of wear predictions, future work may refine and calibrate the wear coefficients based on comparisons between the simulated and measured wheel profiles.
- Metallographic analysis can be conducted to examine the heat-induced microstructure change of the wheel and rail tested in this study. This analysis can help identify specific changes in the materials, such as the growth of grains, changes in phases, or the formation of small cracks that occur due to the thermal loads. By examining these changes, it becomes possible to understand the reasons for material damage from a material science perspective. This understanding provides information for explaining how and why the materials degrade or fail when exposed to high temperatures, which can help in improving material choices, design methods, and maintenance practices to increase the reliability and lifespan of the wheel and rail under different thermal conditions.
- In the current model, the simulation focused on a single wheel load to analyze its thermal contact impact on the wheel and rail. Future simulations can incorporate cyclic wheel loads, which can more accurately represent real-world conditions where wheels repeatedly pass over the same section of rail. By simulating cyclic loads, it is possible to examine how the repeated application of heat and mechanical stress contributes to the accumulation of thermal effects, such as temperature increases and material softening, which may then lead to greater damage over time. Additionally, the accumulation of plastic deformation from multiple wheel passes can result in material work hardening, which should be considered in future wear calculations to ensure more accurate predictions. This will help refine the estimation of material loss and improve the effectiveness of maintenance strategies.
- The proposed thermomechanical FE model can also be used to study other types of thermal damage caused by the interactions between the wheel and rail, such as

rolling contact fatigue. Rolling contact fatigue occurs when repeated rolling/sliding actions between the wheel and rail, leading to changes in material properties, crack initiation, and eventual material failure. By applying the proposed FE model, it is possible to investigate how the thermal effects contribute to the development and growth of fatigue cracks over time. The analysis may help identify critical factors that influence the rate of fatigue damage, such as temperature rise, temperature-dependent friction levels and material characteristics.

- The thermal contact behavior of the wheel and rail during flange contact on a curved track can be analyzed using the proposed thermomechanical FE model. When a train moves along a curve, the wheel flange makes contact with the rail, generating friction and heat due to the increased lateral forces. This contact may lead to significant temperature rise at the contact points, affecting the material properties of both the wheel and the rail, such as hardness and resistance to wear. By using the FE model, it is possible to simulate and study how these thermal effects develop and interact during flange contact, providing a better understanding of the heat distribution and temperature changes along the curve. This analysis can help identify areas at higher risk of thermal damage, optimize rail design, and develop strategies to minimize wear and improve safety and performance on curved tracks.



# ACKNOWLEDGEMENTS

Time flies, and I have now reached the end of my PhD journey. However, I still vividly remember the day I first arrived in Delft, carrying my bags and filled with anticipation for my PhD studies, along with some anxiety about the uncertain future. I consider myself incredibly fortunate to have encountered supportive teachers and friends who accompanied me throughout this long academic journey, allowing me to gain so much. Here, I would like to take this opportunity to express my heartfelt gratitude to everyone.

I am deeply grateful to my supervisor, Prof. Zili Li. The first time I met Prof. Li was during my PhD application interview. I shared my master's research topic with him, and he asked me to take out paper and pen to draw the gear transmission diagram of a train, which was the core content of my master's research. I am especially thankful to Prof. Li for giving me the opportunity to continue my studies at TUD after the interview. At that moment, I realized that Prof. Li is a very rigorous and serious academic. Throughout our progress meetings, you consistently maintained a rigorous and serious attitude, and your extensive knowledge was evident as you could always provide practical help and guidance on any issue. You always managed to explain complex problems clearly using simple diagrams, and I am grateful for your patience in teaching me through illustrations. Whenever I felt lost in the academic forest, I was thankful that you could guide me back to the right path. Your eyes always sparkled when discussing academic research, and your critical thinking and passion for academia have profoundly influenced me.

I am also very thankful to my daily supervisor, Dr. Zhen Yang. You played a crucial role in my PhD research. You helped me a lot both academically and personally. Thank you for generously sharing your PhD research experience and insights. We discussed theories, methods, and the reasons behind results together. I appreciate your detailed and patient guidance in modeling and all the help and comments you provided for my writing. Thank you for being patient and open to my weird ideas. Your serious attitude towards academia and strong logical thinking have greatly influenced my way of thinking.

The wheel-rail contact temperature tests were a crucial part of my PhD thesis. The success of these experiments would not have been possible without the help of Prof. Zili Li, Dr. Zhen Yang, Jan Moraal, Derek van Bochove, Tom Dries, Gokul Jayasree Krishnan, Fang Ren, and Ron Penners. Special thanks to Prof. Li and Dr. Yang for the detailed discussions before the measurements. A special thanks to Jan Moraal for safely running the V-Track test rig under such extreme braking conditions. Thank you for meticulously recording every set of data and replacing the worn-out wheels. I also thank Derek van Bochove for designing the device to mount the infrared camera on the test rig and for repeatedly helping me install and remove the camera during the tests. Special thanks to Tom Dries, the owner of the camera rental company, who drove three hours from Belgium to assist me with the experiments despite having a knee injury from playing football. I am grateful for Gokul Jayasree Krishnan's contribution during the

experiments. Thanks to Fang Ren and Ron Penners for their enthusiastic help with the emissivity tests.

The research was partly supported by the China Scholarship Council and the numerical work in this thesis was partly supported by ProRail and Europe's Rail Flagship Project R2DATO-Rail to Digital automated up to autonomous train operation. I am grateful for the financial support from them.

The process of developing the finite element model encountered numerous difficulties. I would like to thank Shaoguang Li, Pan Zhang, Fang Ren, and Meysam Naeimi for their technical support during this challenging process. Your willingness to share your experience unreservedly helped me immensely. Discussions with you sparked my thinking, enabling me to quickly identify and resolve each new problem. I sincerely hope that the LSDYNA company will provide advisory panels for researchers in different fields.

The companionship of colleagues and friends has been particularly important throughout this journey. Special thanks to Jacqueline Barnhoorn for her efficient help in communicating with the graduate school and handling my resident permissions. I am also grateful to Prof. Dollevoet and Dr. Alfredo Nunez. Your passionate approach to research continually inspired me. Daily interactions with my office mates Li Wang and Taniya Kapoor made our office a productive and enjoyable environment. Your dedicated work created a learning atmosphere, and our jokes during breaks added much joy to our daily research life. Thanks to Siwarak Unsiwilai for your enthusiastic sharing and help during my studies. I also want to thank my other colleagues in the railway group: Valeri Markine, Ellard Groenewegen, Yunlong Guo, Wenli Jia, Chen Shen, Yuanchen Zeng, Zhiwei Qian, Xiangyun Deng, Xiangming Liu, Hongrui Wang, Omid Hajizad, Wassamon Phusakulkajorn, Yang Jin, and Bin Zhu. Your companionship made the journey of pursuing a PhD more wonderful. Special thanks to Dr. Xinxin Yu. You are like a beautiful sunflower, always full of energy. You are always willing to share and listen, and your passion for your work and future is truly inspiring. I am especially grateful to Yunlong Guo and Lili Ma for taking me bouldering. Your patient encouragement and teaching greatly inspired me, even though I am not naturally athletic.

Besides my colleagues and friends in the railway group, I would also like to thank my wonderful friends from the Delft fellowship: Philip and Ting Xin, Weiyuan Zhang and Chengcheng, Andy and Sharon, Pan Zhang and Ying Wu, Gengjing Chen and Jiayu, Tianmu and Yan Li, Chao Lian and Emily, Guojie Pan, Weiwei, Jingqi Zhuang, Qing Yu, Fei Wu, Yiyun Wang, Yicong Wang, and Yuhang Zhai. Thank you all for your care and help in my daily life. Special thanks to the Children, Muyan Zhang and Muzhen Zhang, Muyan Chen, Yunrong Li, and Yunhui Li, for bringing joy to my life with their innocent smiles. I have cherished every moment of our activities together, such as digging for oysters, making dumplings (my specialty), cooking spicy soup, traveling to Germany, and visiting Christmas markets in the Netherlands. These wonderful and heartwarming activities have brought me immense happiness. You all have shown me that there is no fear in love.

Besides my friends in the Netherlands, I would also like to thank my teachers and friends in China, Canada, Sweden, Italy, the United States, Germany, Japan, and the United Kingdom. They are Prof. Wanming Zhai, Prof. Zhaowei Chen, Prof. Yu Sun, Dr.

Zhiyong Shi, Dr. Xuancheng Yuan, Dr. Can Shi, Dr. Jianjin Yang, Dr. Huiyu Chen, Dr. Andréas Andersson, Dr. Zhiyong Shi, Dr. Jackson Chen, Xiangkai Ding, Ming Chen, and Yi Jiang. Special thanks to my master's supervisor, Prof. Zhai, for his continuous support. I am grateful to Yu Sun and Zhaowei Chen for their help in academic collaboration. Thank you, Dr. Huiyu Chen, for being my friend since we became roommates in 2011. You understand me best and are always there to listen. We have encouraged each other and shared our PhD experiences and insights, making your companionship especially comforting. Thanks to Jackson Chen, an excellent computer science PhD, for sharing your experiences in the US, which have given me much inspiration and thought.

I am especially grateful for the pets that have come into my life. To Modeling, the guinea pig, your steady temperament provided much-needed energy to my anxious self. To the cats, Oscar, Jackson, Nobel, and Marie as well as Candy the border collie, thank you for constantly providing cute and healing energy to my soul.

Lastly, I want to thank my parents and brother for their unwavering support. Though you may not express it often, your unconditional love has given me immense courage. I am grateful to my parents for fully respecting my decisions and giving me the freedom to grow and explore myself. Your persistence in staying active and pushing your limits is truly admirable. I wish you both health and longevity. To my brother, thank you for your companionship, even though you have caused me many worries over the years. Now, as a PhD student in traditional Chinese medicine, I hope your doctoral journey goes smoothly.



# CURRICULUM VITÆ

## Chunyan HE

20-01-1991 Born in Inner Mongol, China.

### EDUCATION

2011–2015	BSc, Machine Design Manufacture and Automation Southwest Jiaotong University, China
2015–2018	MSc, Vehicle Engineering Southwest Jiaotong University, China
2018–2024	Ph.D. Railway Engineering Delft University of Technology, the Netherlands <i>Thesis:</i> Thermomechanical Analysis of Wheel-Rail Contact: Modeling, Validation, and Application <i>Promotor:</i> Prof. dr. Z. Li
2024–Present	Postdoc Researcher, Railway Engineering Delft University of Technology, the Netherlands



# LIST OF PUBLICATIONS

## Thesis-related Journal papers

3. **He, C**, Zhang, P., Yang, Z., & Li, Z. (2025). *Infrared Temperature Measurement in Wheel-Rail Frictional Rolling Contact with High Slip Ratios*. (Under review)
2. **He, C**, Yang, Z., Zhang, P., Dollevoet, R., & Li, Z. (2025). *Thermomechanical finite element modeling of wheel-rail contact and experimental validation*. Tribology International, 209, 110666.
1. **He, C**, Yang, Z., Zhang, P., Li, S., Naeimi, M., Dollevoet, R., & Li, Z. (2024). *A finite element thermomechanical analysis of the development of wheel polygonal wear*. Tribology International, 195, 109577.

## Other Journal papers

3. Chen, Z., Wan, F., & **He, C**. (2024). *Field Test and Numerical Study of Train-Induced Vibration of Over-Track Buildings Above Metro Depot*. Urban Rail Transit, 10(4), 361-375.
2. Zhang, P., **He, C**., Shen, C., Dollevoet, R., & Li, Z. (2024). *Comprehensive validation of three-dimensional finite element modelling of vehicle-track high-frequency interaction*. Vehicle System Dynamics, 62(11), 2785-2809.
1. Li, S., Naeimi, M., **He, C**., Dollevoet, R., & Li, Z. (2023). *An integrated 3D dynamic FE vehicle-track model in elasto-plasticity to investigate short pitch corrugation under cyclic wheel loads*. In Structures (Vol. 53, pp. 1000-1011). Elsevier.

## Conference Papers

4. **He, C**., Yang, Z., & Li, Z. *Experimental validation of thermo-mechanical finite element wheel-rail contact modeling using the V-Track test rig*. the third International Conference of Rail Transportation, Shanghai, China, August 7-9, 2024.
3. **He, C**., Yang, Z., & Li, Z. *A measurement of the wheel-rail contact temperature field*. the 28th IAVSD International Symposium on Dynamics of Vehicles on Roads and Tracks, Ottawa, Canada, August 21-25, 2023.
2. **He, C**., Yang, Z., Zhang, P., Li, S., Naeimi, M., & Li, Z. *A finite element thermomechanical study on the development of polygonal wear*. the fifth International Conference on Railways Technology, Montpellier, France, August 22-25, 2022.
1. **He, C**., Yang, Z., Zhang, P., Li, S., Naeimi, M., & Li, Z. *A finite element thermomechanical analysis of polygonal wear*. the 27th IAVSD International Symposium on Dynamics of Vehicles on Roads and Tracks, Saint-Petersburg, Russia, August 16-20, 2021.